Università Campus Bio-Medico di Roma
School of Engineering

PhD Course in Bio-Engineering and Bio-Sciences
XXIX – 2014/2016

Design, Realization and Testing of a Multi-Sensory Device for Food and Medical Applications

Author
Alessandro Zompanti

Supervisor
Prof. Giorgio Pennazza

Co-Supervisor
Prof. Marco Santonico

Research Unit of Electronics for Sensor Systems

April 2017

Introduction: Taste and Olfaction

Sense of Taste in humans

The reaction between a substance and the taste receptors, located on the taste buds into the mouth (mostly present on the tongue), produces the sensation of taste.

The tongue is covered with thousands of small bumps called papillae, each containing hundreds of taste buds. Most of the taste buds (2000-5000 units) [1] are located on the back and the front of the tongue.

Taste receptor cells of vertebrates are not neurons, but originate from the epithelial covering of the body [2]. To connect to oral space, they send a thin dendritic process to the epithelial surface. The cells occur either singly or densely packed in taste buds, where up to 100 form a functional unit. On the tongue, the taste buds are mounted in special folds and protrusions called papillae.

It was determined that each chemoreceptive area of the human tongue responds to each of the basic tastes: sweetness, sourness, saltiness, bitterness, and umami. Taste buds are able to differentiate among different tastes through detecting interaction with different molecules or ions. Neurons may be particularly sensitive to one or only two of the basic tastes [3][4][5]: sweet, umami and bitter tastes are triggered by the binding of molecules to G protein-coupled receptors; when an appropriate molecule reaches the taste cell, the interaction of the molecule with the G-proteins leads to chemical changes that results in a neural impulse. The perception mechanisms of salt and sour taste are different: saltiness and sourness are perceived with the increase of the concentration of sodium and hydrogen ions in the saliva, reacting with the taste buds.

Mammalian taste-responsive cells age fast, having a lifetime of about 10 days. So any one nerve terminal in a taste bud frequently has to detach from an old cell and connect to a developing taste cell and form new synapses on its surface. The new cell has presumably to be compatible to that specific type of nerve fibre: for instance, a nerve fibre previously connected to a Na^+-responsive cell will again attach to a cell of the same kind. But according to deeper electrophysiology studies [6] a simple one-to-one line design, where each fibre responds to just one type of taste cell is not evident. Some nerve fibres are specialists, but many are generalists, carrying responses to more than one taste quality from different taste cell types.

Similarly, many receptor cells are generalists not showing specificity to a particular taste stimulus (sweetness, sourness, saltiness, bitterness). Given such distributed responses, a part of the information about individual taste sensation must be contained in the quorum of the receptors cells responses. So one of main tasks of the central taste processing will be the identification of the right information about the on-going taste sensation, obtained by pattern discrimination processes [7].

Humans categorize taste into a small palette of qualities: umami and sweet are "good" tastes that promote consumption of nutritive food, whereas bitter and sour are "bad" tastes that alert the organism to toxins and low pH, promoting

rejection of foods containing harmful substances. Salt can taste either "good" or "bad" depending both on the concentration of sodium and on the physiological needs of the taster [8][9].

Receptors and transduction

Taste perception is initiated by the chemical interaction of testant molecules with specific receptor proteins located at the surface of the taste receptor cells.

Taste cells have two specializations: microvilli in contact with the oral cavity and synapses with sensory nerve fibres. Taste receptors proteins are mounted onto the microvilli. On binding taste molecules, the receptors trigger transduction cascades that activate synapses, causing excitation of the nerve fibre. These carry the signal to the brain stem, where central taste processing begins.

The first "receptors" of the taste stimulus are the membrane proteins in the apical surface of the taste receptor cells. They provide the molecular specificity to the taste response: ion channels, ligand-gated channels, enzymes and GPCRs (G protein–coupled receptors) serve as receptors for the basic tastes (sweetness, sourness, saltiness, bitterness) and trigger the transduction chain.

Salt taste

Two taste qualities detect ions in the oral space: salt and sour taste. Salt taste guides the incorporation of NaCl and other required minerals, thus serving an essential function in ion and water homeostasis [10].

The receptor for table salt (NaCl) is an ion channel that allows sodium ions (Na^+) to enter directly into the cell depolarizing it and triggering action potentials in a nearby sensory neuron.

Sour Taste

Sour receptors detect the protons (H^+) liberated by sour substances (acids). This closes trans-membrane K^+ channels, which leads to depolarization of the cell, and the release of the neurotransmitter serotonin into its synapse with a sensory neuron. Sour taste is acceptable or interesting when mild, thereby aiding the recognition of complex food, but it becomes increasingly unpleasant when strong. It serves to detect unripe fruits and spoiled food, and to avoid tissue damage by acids and problems of systemic acid–base regulation.

Sweet Taste

Sweet substances (like table sugar — sucrose) bind to G-protein-coupled receptors (GPCRs) at the cell surface. Each receptor contains 2 subunits designated T1R2 and T1R3 and is coupled to G proteins. The complex of G proteins has been named gustducin because of its similarity in structure and action to the transducin that plays such an essential role in rod vision.

Activation of gustducin triggers a cascade of intracellular reactions: production of the second messengers inositol trisphosphate (IP3) and

diacylglycerol (DAG) which releases intracellular stores of Ca++ which allows in the influx of Na+ ions depolarizing the cell and causing the release of ATP, which triggers action potentials in a nearby sensory neuron.

Bitter taste

Bitter taste is unpleasant though bearable when weak, but repulsive when strong. Bitter taste effectively warns us not to ingest potentially harmful compounds. One of the exciting challenges in taste research is to understand how bitter receptors were shaped by evolution to serve this task.

The binding of substances with a bitter taste also takes place on G-protein-coupled receptors that are coupled to gustducin and the signaling cascade is the same as for sweet (and umami).

Humans have genes encoding 25 different bitter receptors ("T2Rs"), and each taste cell responsive to bitter expresses a number (4–11) of these genes. This is in sharp contrast to the olfaction system where a single odor-detecting cell expresses only a single type of odor receptor.

Umami taste

"Umami" a term derived form the Japanese *umai* (delicious), designates a pleasant taste sensation that is qualitatively different from sweet, salty, sour and bitter. Umami is the response to salts of glutamic acid, like monosodium glutamate (MSG), a flavour enhancer used in many processed foods and in many Asian dishes. Processed meats and cheeses (proteins) also contain glutamate.

The binding of amino acids, including glutamic acid, takes place on G-protein-coupled receptors that are coupled to heterodimers of the protein subunits T1R1 and T1R3. The signal cascade that follows is the same as it is for sweet and bitter.

Olfaction in humans

From an evolutionary perspective, the chemical senses — particularly olfaction — are deemed the "oldest" sensory systems; nevertheless, they remain in many ways the least understood of the sensory modalities. The olfactory system processes information about the identity, concentration, and quality of a wide range of chemical stimuli. These stimuli, called odorants, interact with olfactory receptor neurons in an epithelial sheet (the olfactory epithelium) that lines the interior of the nose.

Transduction of olfactory information occurs when odorant molecules contact the dendrites of olfactory receptor neurons (ORNs). These neurons reside in the olfactory epithelium, a specialized region of the dorsal nasal cavity. The axons arising from the receptor cells project directly to neurons in the olfactory bulb, which projects in turn to the pyriform cortex in the temporal lobe.

Unlike taste-receptor cells, which are modified epithelial cells, olfactory receptors are true neurons. Their cell bodies lie in the basal two-thirds of the epithelium, and their apical dendrites extend to the surface.

The olfactory receptors are located in both the cilia and synapses of the olfactory sensory neurons and in the epithelium of the human airway. The odorant receptors are expressed in the cell membranes of olfactory receptor neurons and are responsible for the detection of odorants which give rise to the sense of smell. Activated olfactory receptors trigger nerve impulses that transmit information about odour to the brain. These receptors are members of the class A rhodopsin-like family of G protein-coupled receptors (GPCRs).

Rather than binding specific ligands, olfactory receptors display affinity for a range of odour molecules, and conversely a single odorant molecule may bind to a number of olfactory receptors with varying affinities, [11] which depend on physio-chemical properties of molecules like their molecular volumes [12].

Once the odorant has bound to the odour receptor, the receptor undergoes structural changes and it binds and activates the olfactory-type G protein on the inside of the olfactory receptor neuron. The G protein (Golf and/or Gs) [13] in turn activates the lyase - adenylate cyclase - which converts ATP into cyclic AMP (cAMP). The cAMP opens cyclic nucleotide-gated ion channels, which allow calcium and sodium ions to enter into the cell, depolarizing the olfactory receptor neuron and beginning an action potential which carries the information to the brain.

The reason for the large number of different odour receptors is to provide a system for discriminating between as many different odours as possible. Even so, each odour receptor does not detect a single odour. Rather each individual odour receptor is broadly tuned to be activated by a number of similar odorant structures. So most odours activate more than one type of odour receptor. Since the number of combinations and permutations of olfactory receptors is very large, the olfactory receptor system is capable of detecting and distinguishing between a very large number of odours [14].

Therefore, each odorant has its own pattern of activity, which is set up in the sensory neurons. This pattern of activity is then sent to the olfactory bulb, where other neurons are activated to form a spatial map of the odour.

Compared to vision, audition, touch, and even taste, our understanding of olfactory-system function lags behind. A major reason for this is that we are only beginning to understand how odours are "coded" by primary olfactory neurons in the nasal epithelium and by activity patterns in the olfactory bulb.

Olfactory and Taste Senses Integration

Integration of information from physiologically distinct sensory modalities is a general property of the mammalian nervous system [15]. The purpose of this integration strategy may be to enhance the detection or identification of stimuli, especially in those cases where the information from a single sensorial modality is ambiguous or low perceptible.

Sense of taste and olfaction allow us to perceive chemicals in the air or in food. Despite being senses belonging to different sensorial systems, taste and smell are intimately connected: interactions between the senses of taste and smell enhance our perceptions of the foods we eat.

Tastants, chemicals in foods, are detected by taste buds, special structures embedded within small protuberances on the tongue called papillae. Other taste buds are found in the back of the mouth and on the palate. Each taste bud

consists of 50 to 100 specialized sensory cells, which are stimulated by tastants such as sugars, salts, or acids. When the sensory cells are stimulated, they cause signals to be transferred to the ends of nerve fibres, which send impulses along cranial nerves to taste regions in the brainstem. From here, the impulses are relayed to the thalamus and on to a specific area of the cerebral cortex, which makes us conscious of the perception of taste.

Airborne odour molecules, called odorants, are detected by specialized sensory neurons located in a small patch of mucus membrane lining the roof of the nose. Axons of these sensory cells pass through perforations in the overlying bone and enter two elongated olfactory bulbs lying against the underside of the frontal lobe of the brain.

Ultimately odour and taste information combine in specific areas of the brain (far anterior insular cortex, the caudal OFC, the amygdala, the ventral forebrain and the ACC (Anterior Cingulate Cortex) [16][17], allowing us to detect the perception of the flavours of foods.

Odour and Taste Sensor Systems

The senses of taste and smell have long played a fundamental role in human life and social interactions. Consequently, many industries manipulate the aroma and the taste of their products in order to improve appeal and quality to get more consumers. As a result, research and quality control of aroma and taste characteristics during product manufacturing has become of great importance in industrial production processes.

So electronic nose and tongue systems have got increasingly attention in the last two decades and they are now widely used in numerous research fields like agriculture, food, biomedical, environmental and pharmaceutical applications.

Electronic Nose

In the human olfactory system, odorants are detected by numerous biological sensors (olfactory receptors) and stimulate a neural signal; signals are processed in the olfactory bulb and finally analysed in specific areas of the brain. The brain achieves a pattern recognition analysis of the neural signals in order to detect and identify each odour.

Latest technological developments have made possible the realization of devices, called electronic noses [18], capable of detecting volatile compounds and so identifying different kinds of aroma. E-nose systems are based on the principle of the identification or classification of odours, analysing a mixture of compounds rather than identifying a single component.

Electronic-nose systems have been designed specifically to be used for numerous applications in many different industrial production processes.

Industry field	Application area
Agriculture	Crop protection
	Harvest timing and storage
	Meat, seafood and fish products

	Plant production Pre- and post-harvest diseases
Airline transportation	Public safety & welfare Passenger & personnel security
Cosmetics	Personal application products Fragrance additives
Environmental	Air and water quality monitoring Indoor air quality control Pollution abatement regulations
Food and beverage	Consumer fraud prevention Quality control assessments Ripeness Food contamination Taste Smell characteristics
Manufacturing	Processing controls Product uniformity Safety Security Work conditions
Medical and clinical	Pathogen identification Pathogen or disease detection Physiological conditions
Military	Personnel and population security Civilian and military safety
Pharmaceutical	Contamination Product purity Variations in product mixtures
Regulatory	Consumer protection Environmental protection
Scientific research	Botany Ecological studies Engineering Material properties Microbiology Pathology

Table 1: List of e-nose applications [20]

Electronic nose can be used as an auxiliary tool for panellists (human testers) of the food industry in order to better evaluate food quality. Even if human panel testing is being used for centuries, the disadvantages are many: panellist's judgment is subjective and may be affected by several human factors like individual variability, fatigue, etc.

It's obvious that human replacement with artificial systems, able to detect sensorial parameters such as aroma, taste and exterior appearance, would allow objective evaluation of foodstuffs quality: this opportunity promises a very good chance for food industry. Moreover the use of artificial system could be

implemented directly in the production line, allowing a control over the entire production batch, instead of current controls carried out over samples.

	Panel	E-Nose	GC-MS
Cost	High	Low	Medium
Reproducibility	Low	Medium	High
Objectivity	Low	High	High
Invasiveness	High	Low	Low
Flexibility	Low	High	High
Analysis length	High	Low	Medium

Table 2: Comparative chart of different analysis methods

Most of the electronic nose systems (used for both commercial and scientific research applications) perform analysis providing a complex information on the sample composition: usually they return a signature (fingerprint) very useful to perform pattern recognition analysis.

E-Nose architecture is highly dependent from the specific application. In general an e-nose device is made of a gas sampling and delivery system, a sensors array, a signal conditioning stage, a data acquisition stage, a signal pre-processing stage and classification/regression software.

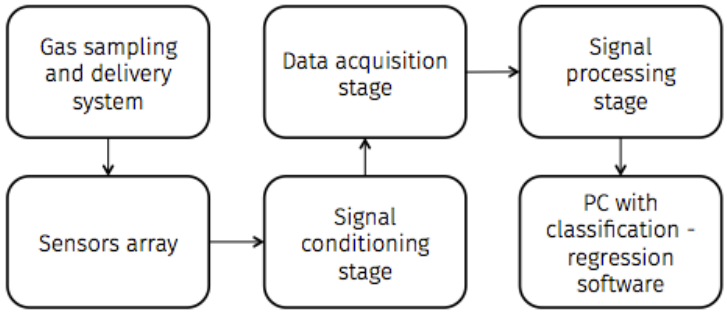

Fig 1: Block diagram for e-nose systems

In the e-nose systems, the interaction between chemical volatile compounds and each gas sensor of the array causes the reversible and real-time variation of an intrinsic quantity of the sensor and then the production of an electrical signal, that has to be recorded and processed.

The commonly used types of sensors for electronic nose belong to the different following categories [19]:

- Piezoelectric sensors (also called acoustic sensors): the working principle is based on the acoustic wave propagation produced by a piezoelectric material, in a multilayer structure. The acoustic waves can travel on the surface of the sensor (SAW = Surface Acoustic Wave) or inside, into the sensor bulk (BAW = Bulk Acoustic Wave).

- Chemo-resistive sensors: the Metal Oxide Semiconductors (MOX), and conductive polymers (CP) are the most used among all the electrical gas sensors. A chemo-resistor is a material that changes its electrical resistance in response to changes in the nearby chemical environment.
- Electrochemical sensors: chemical species reacting at an electronic conductor / ionic conductor interface exchange electric charges, then resulting in an electric signal. Electrochemical gas sensors are cells whose output is directly related to the concentration or partial pressure of the gaseous species. Depending on whether the output is an electromotive force or a current, the devices may be classified in potentiometric or amperometric electrochemical sensors.
- Field Effect sensors are widely used in the e-sensing field: they are similar to traditional MOSFETs, but the interaction between the gate material and the chemical compounds generates charges that modulate the drain-source current.
- Optical sensors: they are used in the traditional absorbance, reflectance and luminescence techniques.
- Calorimetric sensors: a thermal transducer, such a thermistor, monitors the heat generated by specific chemical reactions involving the compounds to be measured.
-

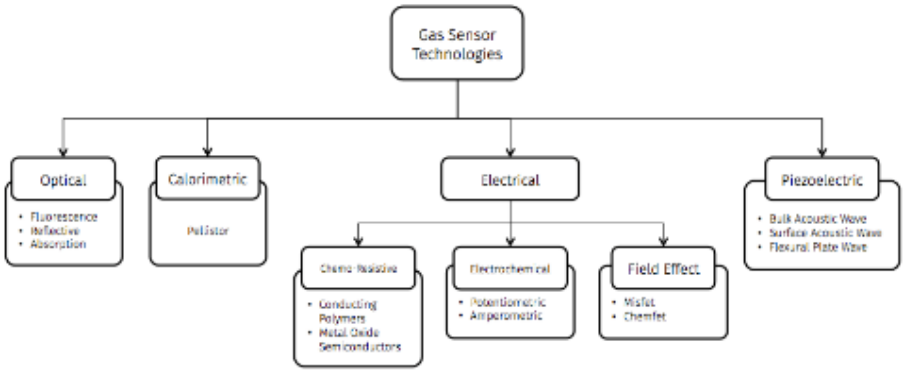

Fig 2: Types of sensors used in electronic nose

There is a variety of advantages and disadvantages of using a specific technology regarding response and recovery times, sensitivities, detection range, operating limitations, physical size, inactivation by certain poisoning agents, and other limitations that are specific to individual sensor types.

E-nose technologies try to mimic the human nose using a large number of low selective gas sensors: human olfactory system can count on a number of 10^8 receptors. Two main peculiar features make the parallelism between human and artificial olfaction possible:

1. The large number of sensors used;
2. Low selectivity of each sensor to single chemical volatile compounds.

Taking into account the large number of chemical compounds that creates a well-determined smell, it is evident that it's much more convenient to extract quickly information linked to global characteristics of the volatile sample rather than discriminate each chemical compounds present in the mixture.

It is important to underline that notion of "odour" does not exactly exist in the field of gas sensor technologies: odour notion doesn't refer to all the complex mixtures of volatile substances, but only to those that the human nose can perceive. The range of smells that the human nose can perceive is a subset of all the possible "smells" that the electronic nose can detect.

Gas sensors used in the electronic nose sensors array are non-specific and so generate pattern responses, also called finger-prints, that represent an univocal electronic signature of the sample under analysis: samples with similar odour usually will have similar response patterns; in the case of samples with distinct odours, the finger-prints will be very diverse.

Electronic Tongue

An electronic tongue is an analytical tool that uses an array of non-specific and low selective chemical sensors, with partial cross-sensitivity, capable to globally respond to the non-volatile compounds present in a test liquid sample. So e-tongue devices are not able to identity individual chemical compounds and the output signals have to be analysed with appropriate methods of pattern recognition and/or Multivariate Data Analysis (MDA) in order to discriminate the samples.

E-Tongue architecture is highly dependent from the specific application. In general it is made by an array of electrodes, a signal conditioning stage, a data acquisition stage, a data pre-processing stage and classification/regression software.

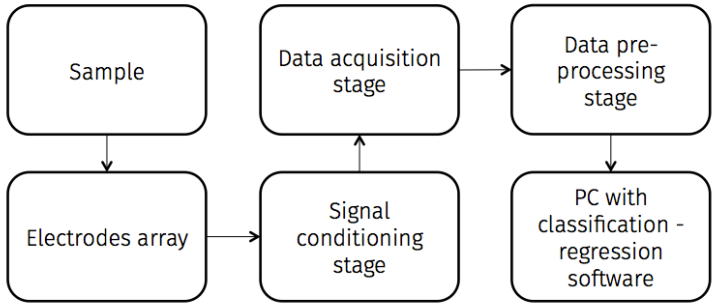

Fig. 3: Block diagram for e-tongue systems

The commonly used types of sensors for electronic tongue belong to the different following categories:

- Potentiometric sensors: the potential, generated by the concentration of a specific family of compounds present on the surface of the

sensing material, is measured between two electrodes when no current is flowing.

- Amperometric sensors: Red-ox reactions in the liquid sample generate a current between the working and the counter electrodes. Current intensity is related to the concentration of compounds involved in the red-ox reactions. The current is measured.
- Voltammetric sensors: Applying a variable potential between the working and the reference electrodes, it's possible to generate red-ox reactions with currents flowing between the working and the counter electrodes. Current peaks are related to the concentration of compounds involved in the red-ox reactions.
- Impedentiometric sensors: ions concentrations in the solution determine sample impedance.
- Piezoelectric sensors: the working principle is based on the acoustic wave propagation on the surface of a piezoelectric material (Surface Acoustic Wave, SAW). The frequency of the wave can be modified by the interaction with an adjacent liquid resulting in a change of the inertial characteristics of the piezoelectric material.
- Optical sensors: colorimetric or fluorescence changes of the chemical receptors, traditional absorbance, reflectance and luminescence techniques.

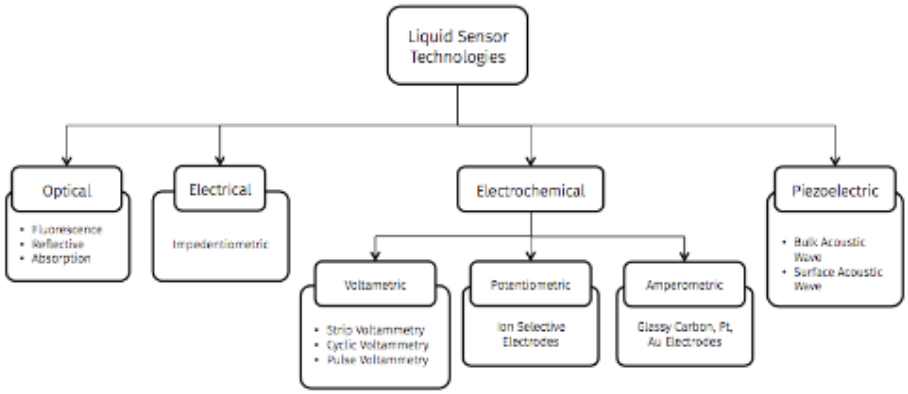

Fig. 4: Types of sensors used in electronic tongue

Data processing and data analysis techniques

Data processing and data analysis are very important components of electronic nose and tongue systems: usually the information produced by the olfactory and taste sensors have a low intensity and are immersed in noise. Moreover, the e-nose and e-tongue sensors are non-specific and produce only an electronic fingerprint of the gas or liquid sample that has to be identified by a complex data analysis process. Also in mammalians, the brain deciphers the information and in spite of its immense capability, the smell and taste interpretation may not always be accurate.

It is very important to pre-process the raw output data produced by the e-sensing system before the final analysis: the appropriate pre-processing technique is crucial for optimizing the performance of the sample classification process. The most commonly used pre-processing techniques are mathematical operation of normalization, scaling, subtraction of the baseline or drift value to better express the data for the next processing steps.

Digital fingerprints generated by e-nose systems have to be analysed using the following techniques in order to extract useful information:

1. Graphical analysis using charts: the simplest data analysis is to use graphs in order to compare the output data (finger-print) and identify the specific aroma;
2. Multivariate Data Analysis (MDA): multivariate data analysis uses a set of statistical techniques on data sets with more than one variable when variables are partially correlated; it operates reducing the high dimensionality of the data (usually higher than three) in two or three dimensions. MDA is very useful to analyse e-nose output data because usually sensors present cross-sensitivity to the different compounds in the gas sample mixture. MDA can be divided into untrained and trained techniques: untrained techniques, such as PCA (Principal Component Analysis), are used when a database of known sample is not present and so is not possible to identify the specific sample but is possible to make a comparison between different unknown sample to discriminate them; on the other hand, trained or supervised technique classify unknown samples on the basis of features of known samples or sets of samples organized into database.
3. Network analysis: Artificial Neural Network (ANN) is the best known and most evolved analysis technique implemented in statistical software packages for e-nose data analysis. Like the cognitive process of the human brain, ANN contains interconnected data processing algorithms that work in parallel looking for similarities and differences between the peculiar characteristics of known aroma patterns present in the reference library. The training process requires a discrete amount of known sample data to train the system and is very efficient in comparing unknown samples to known references. The result of ANN data analysis usually is in the form of a percentage match of identification elements in the sample with those of aroma patterns from known sources in the reference library.

Obviously, the best data analysis method depends on the type and amount of data produced by the sensors.

Combined e-nose/e-tongue systems

In the last decade, many applications using combined electronic nose and tongue approaches have been explored in different research areas. Most of the research reports on combination of electronic and tongue are based on data fusion strategies; very few studies have tried to combine the two e-sensing technologies at hardware level [20].

Data fusion strategies are listed below:

- Low-level data fusion: data are combined at the lower level merging together the raw data produced by the electronic nose and tongue. All the further data analysis steps will be executed on the merged data matrix.

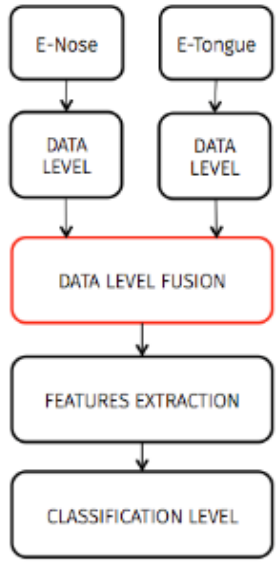

- Intermediate-level data fusion: data fusion occurs at the features selection level. Features extraction is performed on the raw data, separately for the e-nose and the e-tongue; then the best features are merged together in order to achieve the best classification rate. Usually feature level fusion is very useful when raw data are non-commensurable and represent different chemical and physical parameters.

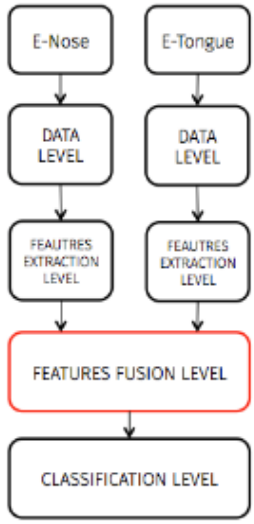

- High-level data fusion: the combination between the two e-sensing systems is performed at the decision level. Separate classification processes are executed using data and features from each e-sensing system; afterwards the classification results are merged to preform the final classification step.

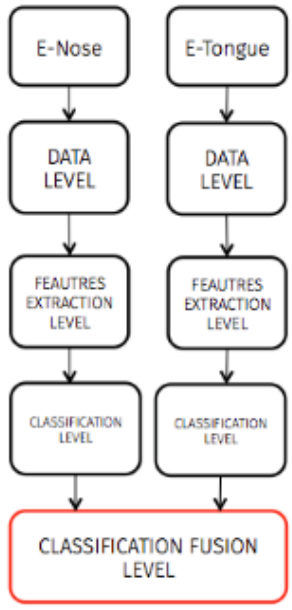

A list of several scientific studies using combined e-nose and e-tongue devices is shown in the following table (Tab. 4):

Sensor Technology	Fusion Technique	Application Area	Data Analysis method	Ref.
- 10 MOSFETs + 4 Metal Oxide sensors (Taguchi) - Pulse Voltammetry (6 WE with different metals, 1 CE, 1 RE)	Data Level Fusion	Fruit Juice	PLS (Partial Least Square)	[21]
- 10 MOSFETs + 4 Metal Oxide sensors (Taguchi) - Pulse Voltammetry (6 WE with different metals, 1 CE, 1 RE)	Decision Level Fusion	Fruit Juice	Bayesian statistical approximation	[22]
- Pulse Voltammetry (4 WE (Gold, Iridium, Rhodium, Platinum), 1 RE (Ag/AgCl), 1 CE (stainless steel)) - 4 SnO_2 Taguchi sensors	Data Level Fusion	Potato chips and creams	ANN (Artificial Neural Networks)	[23]
- Quartz Microbalances (QMB) with metalloporphyrin functionalization - Potentiometric electrodes with metalloporphyrin functionalization	Data Level and Feature Level Fusion	Clinical and food samples (Urine and Milk)	PCA	[24]
- Quartz Microbalances (QMB) with metalloporphyrin functionalization - Potentiometric electrodes with metalloporphyrin functionalization + glass pH electrode	Data Level Fusion	Red Wine	PCA and ANN	[25]
- Commercial e-nose PEN2 (WMA (Win Muster Airsense) Analytics Inc.) composed of 10 metal oxide semiconductor (MOS) type chemical sensors. - Amperometric sensors: a working electrode (a dual glassy carbon electrode and a gold electrode), a reference (Ag/AgCl saturated) electrode and a platinum counter electrode	Data Level Fusion	Italian Wines	PCA, Linear discriminant analysis (LDA), Classification And Regression Tree (CART)	[26]
- Commercial e-nose PEN2 (WMA (Win Muster Airsense) Analytics Inc.): 10 metal oxide semiconductor (MOS) type chemical sensors. - Amperometric sensors: a working electrode (a dual glassy carbon electrode and a gold electrode), a reference (Ag/AgCl saturated) electrode and a platinum counter electrode	Data Level Fusion	Italian Wines	Genetic Algorithms (GA)	[27]
- Commercial e-nose (model 3320 Applied Sensor Lab Emission Analyser, Applied Sensor Co., Linkoping, Sweden): 10 MOSFETs and 12 SnO_2 Taguchi sensors - Amperometric sensors: a working electrode (a dual glassy carbon electrode and a gold electrode), a reference (Ag/AgCl saturated) electrode and a platinum counter electrode	Data Level Fusion	Extra Virgin Olive Oils	ANN	[28]
- Commercial e-nose (model 3320 Applied Sensor Lab Emission Analyser, Applied Sensor Co., Linkoping, Sweden): 10 MOSFETs and 12 SnO_2 Taguchi sensors - Amperometric sensors: a working electrode (a dual glassy carbon electrode and a gold electrode), a reference	E-nose, E-tongue and HPLC data fusion	Extra Virgin Olive Oils	LDA	[29]

	(Ag/AgCl saturated) electrode and a platinum counter electrode				
-	Commercial e-nose α-Prometheus (developed by Alpha MOS): the electronic nose consists of a mass spectrometry system and a gas sensor array of 18 MOXs - Commercial e-tongue α-Astree (developed by Alpha MOS): 7 potentiometric sensors	Data Level Fusion	Apple Juice Quality	Quantitative Descriptive Analysis (QDA, Tragon Corporation)	[30]
-	14 inorganic gas sensors from Figaro and FIS (MOS technology) - Voltammetric sensors (6 WE, 1 CE, 1 RE)	Data Level Fusion	Red Wines	PLS	[31]
-	14 inorganic gas sensors from Figaro and FIS (MOS technology) - Voltammetric sensors (6 WE, 1 CE, 1 RE)	Data Fusion Level	Extra Virgin Olive Oils	PCA, PLS-DA	[32]
-	4 MOSFETs sensors - Shear horizontal surface acoustic wave (SH-SAW) sensors	Data level fusion	Food liquid samples	PCA	[33]
-	E-nose: 4 potentiometric sensors - E-tongue: 9 potentiometric sensors	Data level fusion	Spoilage of wine	PCA, PLS	[34]
-	Commercial e-tongue, Taste-Sensing System SA 402B (Intelligent Sensor Technology Co., Ltd., Japan) - Near and mid infrared spectroscopy - Commercial e-nose PEN2 (WMA (Win Muster Airsense) Analytics Inc.): 10 metal oxide semiconductor (MOS) type chemical sensors.	Data level fusion	Alcoholic fermentation	PLS	[35]
-	7 potentiometric sensors from Sensor Systems (St. Petersburg, Russia) - Commercial e-nose Cyranose320 from Smith Detection: 32 conducting polymers	Data level fusion	Orthosiphon stamineus	PCA, LDA	[36]
-	Infrared spectroscopy - Gas Chromatography Mass Spectroscopy (GC-MS) - Commercial e-nose Cyranose320 from Smith Detection: 32 conducting polymers - 7 potentiometric sensors from Sensor Systems (St. Petersburg, Russia)	Data level fusion	Honey	PCA, LDA	[37]
-	E-nose made of five metal oxide Taguchi Gas Sensors TGS8XX (15, 22, 24, 25, 42) - 6 potentiometric chemical sensors: all-solid-state ion-selective poly(vinyl chloride) (PVC) membranes (Sodium, Potassium, Calcium, Nitrate, Chloride, Fluoride) obtained from ELIT electrodes-NICO 2000 Ltd. and Metrohm. Sensor potential values were measured versus a conventional Ag/AgCl reference electrode	Data level fusion	Fruit juice	ANN	[38]
-	Commercial e-nose PEN2 (WMA (Win Muster Airsense) Analytics Inc.): 10 metal oxide semiconductor (MOS) type chemical sensors. - Commercial e-tongue α-Astree (developed by Alpha MOS): 7 potentiometric sensors	Feature level fusion	Cherry tomato squeezed juice	Canonical Discriminant Analysis (CDA), Library Support Vector Machines (Lib-SVM)	[39]
-	Eight metal oxide TGS Figaro gas sensors, TGS8XX (XX = 13, 21, 22, 25, 26, 30, 31, 32) - Cyclic voltammetry	Data level fusion	Mixed Edible-Oil	PCA, PLS	[40]
-	Commercial e-nose PEN3 (AIRSENSE	Data level	Rice wine	PCA, Multiple	[41]

	ANALYTICS GmbH, Schwerin, Germany) system: 10 metal-oxide gas sensors - Commercial e-tongue α-Astree (developed by Alpha MOS): 7 potentiometric sensors	fusion	Linear Regression (MLR), SVM

Table 3: Applications of combined e-nose and e-tongue systems

Many studies proved that combining e-nose and e-tongue devices is possible to obtain an improvement: when data or feature generated by the two different systems are combined together, the classification performance increases compared to the performances of the individual e-sensing systems.

However it is necessary to underline that the combination of e-nose and e-tongue systems could involve some downsides: several researchers reported limitations mostly arising from the particular experimental conditions that differ between the two sensing systems. So it could be very important to develop a sensing device implementing the e-nose and e-tongue technologies, to measure the gas and liquid samples at the same time with the same experimental conditions (e.g. temperature, relative humidity). Moreover, instead of using generalized sensors, development of application specific sensors would be an important improvement.

It is also very important to pay special attention to data fusion: raw data, generated by e-nose and e-tongue systems, are usually non-commensurable and represent different chemical and physical parameters. It's necessary to adequately pre-process the raw data to obtain realistic classification results. It's important to improve classification algorithms through feature extraction optimizations or developing peculiar data analysis processes for particular applications.

Another issue is to find the right correlation of the parameters between the combined e-sensing systems and panellist judgments that are often used to train the classification processes. Usually panellist or consumers data are subjective and generate low classification rates.

Moreover e-nose and e-tongue systems are mostly used to evaluate natural products containing a large number of chemical compounds: when chemical analyses are used to find a correlation between sample representative chemical compounds and e-sensing output data, there is a significant risk to take into account only one or two major chemicals, ignoring other minor relevant compounds, obtaining the non-optimal training model for the classification engines.

Summing up, combined e-nose and e-tongue systems are mostly applied in food quality area and in a few clinical areas. Considering the great potentialities of these e-sensing systems, it is obvious therefore that their application could be extended to several other areas, ranging from human safety to environmental monitoring.

Combined e-nose and e-tongue systems are still in the first development stages, but this kind of new technology seems to be very promising and in the next years it will make possible several successful new applications.

PhD Research Proposal: Multi-sensory Device for Food and Medical Application

Brief Introduction

In most cases analyses on gas and liquid samples are performed using several sensors arranged in multi-dimensional systems (array of sensors) or in network systems (sensors systems expressly distributed on a special area), according to the specific application. Sensors array are intended to mimic the working principles of the human senses: advancements made in the field of electronic miniaturization, power consumption reduction and data analysis techniques make possible the realization of these new technologies.

Measuring devices implementing sensors array are used both in the medical applications fields, because of their minimally invasive approach for the patients, and in the food industry field because of their non-destructive approach towards the food samples.

This PhD research activity is focused on the design, realization and test of a novel multi-sensory system for medical and food applications.

State of the art

Chemical analysis techniques for gas and liquid sample are evolving and changing dramatically: the current technologies, instead of focusing on a single parameter, aim to extract global qualitative information of the sample under analysis.

For this reason there is a growing interest in developing both technologies that allow the collection of large amounts of data (such as array of gas and liquid sensors), and pre-processing techniques that allow the extraction of features from the collected data, granting a high scientific value to the qualitative analysis of the sample.

Measuring devices used in this kind of qualitative analysis consist of arrays of sensors, each with a different selectivity to chemical compounds families, a data acquisition unit, able to collect the electrical output signals, and data analysis unit in order to process and decipher the measured quantities.

Figure 5: Block Diagram of gas or liquid sensor system

The array of sensors is able to generate a characteristic pattern, specific for the analysed sample. Unique pattern generation is allowed by the different

selectivity of the sensors used. The lack of specificity of the sensors makes possible the recognition of a large number of qualitatively different samples.

In the last decade, e-sensing technologies made great progresses both from a purely technical point of view as well as regarding their real applications in the productive processes.

E-sensing tech potentialities could be exploited arranging sensors in complex multidimensional systems, making possible the extraction of a specific pattern or fingerprint, as well as in sensor networks, allowing the distribute monitoring on the analysed sample. Arrays of chemical sensors now represent the standard sensing technology to realize devices that can mimic the working principles of the human senses with a wide range of use for medical applications [42][43][44] and the food industry [45][46][47][48].

However, these technologies have not still reached sufficient maturity to be able to allow their real usage in production routine activities both in the medical and industrial fields [49], even if the number of possible applications continues to grow. Such limits arise from a lack of standardization among the outputs of the existing e-sensing technologies, which differ both for transduction principles and for the sensitive materials.

Several scientific studies were performed using different gas and liquid sensor systems [20]: usually distinct devices with different experimental conditions are used to generate the output data and the final results are obtained just through data fusion.

Only few recent studies investigated on the simultaneous analysis on gas and liquid sample: Cole et al., 2011, [50] realized an interesting experiment with the simultaneous analysis of a gas and a liquid sample, using two sensors based on different working principles; In particular, gas sensors are based on shear horizontal SAW and liquid sensors are based on ChemFET.

The simultaneous analysis of the liquid and vapour phase of the same sample, using a single device, really express the concept of synaesthesia [51], that is the multi-sensorial approach of the human body. The concept of synaesthesia provides interesting ideas for a possible technological development in the field of electronic sensing systems.

Aims of the project

The cross-selectivity phenomenon is one of the main issues regarding the use of chemical sensors: cross-selectivity represents a major limit in the case of using a single sensitive material and a single transducer. However, the phenomenon of cross-selectivity can become an opportunity if the liquid and vapour phases of a single sample is analysed using different types of transducers and a common sensitive material.

On this working principle is based the idea of realizing a novel multi-sensory system. Human beings use the five senses simultaneously: the interaction between different senses is called synaesthesia.

The present doctoral thesis aims to the design, realization and test of a multi-sensory system for biomedical and food applications: the integrated system will consist of gas sensors system and liquid sensors system. The use of different

types of sensors allows the simultaneous analysis of the physical-chemical characteristics of the liquid and vapour phases of the samples.

Gas sensor system

The sensing system for the vapour phase of the sample will use piezo-electric sensors: the working principle is based on the propagation of an acoustic wave produced by a piezo-electric material (Quartz Crystal Microbalance (QCM)). The measuring device will consist of an array of QCM functionalized with a biological sensing material that will interact with the analysed volatile compounds. The absorption of volatile compounds produces a change of the resonance frequency: this change represents the quantity to be monitored.

The response of the sensors depends on the chemical properties of the sensitive biological material. The sensors have to be connected to an oscillating circuit and the oscillation frequency changes will be measured.

Liquid sensor system

The sensing system for the liquid phase of the sample will use cyclic voltammetry techniques trough a three-electrode system: the effects of the concentration of the different species in the liquid sample on the current-voltage characteristics of the redox reactions involved will be analysed.

In particular, the three-electrode system consist of:

- Working electrode, whose potential is varied in a predetermined manner;
- Reference electrode, the potential of which remains unchanged during the measurement;
- Counter electrode, also called auxiliary electrode, which has the task of absorbing or providing the current produced by the redox reactions. The use of the counter electrode allows to not compromise the stability of potential of the reference electrode because of a current flow over it.

The reason for this particular configuration is that the reference electrode potential has to be not modified. A variable potential difference is applied between the working electrode and the auxiliary electrode; the current flowing between the working and the counter electrodes is measured. The current will be generated by the redox chemical reactions and will be related to the concentration of specific compounds contained into the liquid sample.

Electronic interfaces

It will be necessary to interface the developed sensors with custom electronic circuits in order to:

- Amplify the output signal generated by the sensors;
- Obtain a satisfactory Signal-to-Noise ratio;
- Limit side effects caused by secondary phenomena that could affect the sample analysis process (e.g. temperature, humidity, etc.)

Project Impact

The use of the proposed multi-sensory system could have several application opportunities in the medical and food industry area because:

- The device could be used on-line to monitor production processes in food industries;
- It is non-destructive for the food samples;
- It is low invasive for the patients (analysis of breath, saliva, blood or urine);
- It is low cost, suitable for large medical screening campaigns;
- It allows cross-sensorial analysis, because different sensors, working together, can record a more complete and complex information.

Considering the biomedical applications, the low invasiveness of the system is very important because it allows the short- and long-term monitoring of patients, without any particular complications.

From a purely scientific point of view, the innovative multi-sensory approach could perform a more comprehensive analysis of the sample (vapour and liquid phase simultaneously), allowing the correlation of pathogens that would be impossible to achieve through the analysis of the single phase of the sample.

The multi-sensory device could be used as an auxiliary tool for human testers of the food industry in order to better evaluate food quality. Even though human panel testing is being used for centuries, the disadvantages are many: panellist's judgment is subjective and may be affected by several human factors like individual variability, fatigue, etc.

It's obvious that human replacement with artificial systems, able to analyse the flavour of the product, would allow objective evaluation of foodstuffs quality: this opportunity promises good chances for food industry. Moreover the use of artificial system could be implemented directly in the production line, so allowing a control over the entire production batch, instead of current controls carried out over samples.

Novel multi-sensory device design and realization

E-tongue

Introduction: e-tongue working principles

The e-tongue system is based on an electrochemical analytical technique called cyclic-voltammetry.

Cyclic-voltammetry (CV) is a type of potentiodynamic electrochemical measurement used to study the electrochemical properties of an analyte in solution or the surface of an electrode [52].

A standard CV experiment employs an electrochemical cell with three electrodes:

- Working electrode (WE);
- Reference electrode (RE) at constant potential;
- Counter Electrode (CE).

All the volammetric techniques implies the application of a electrical potential (V) on one couple of electrodes (WE/RE) and the measurement of the produced current (i) flowing between another couple of electrodes (WE/CE).

Current peaks, measured in respect of specific potential values of the input signal, are caused by oxidation or reduction phenomena occurring on the surface of the working electrode. Usually current at the working electrode is plotted versus the applied voltage (that is, the working electrode's potential) to give the cyclic voltammogram trace.

Oxidation and reduction reactions are complementary chemical processes in which the oxidation states of atoms change. Redox reactions cause both reduction process, in which one reactant acquires electrons, and a complementary oxidation process, in which one reactant lose electrons:

- Oxidation is the loss of electrons or an increase in oxidation state by a molecule, atom, or ion.
- Reduction is the gain of electrons or a decrease in oxidation state by a molecule, atom, or ion.

In the following sections, the some electrochemistry fundamentals will be discussed to make the working principle of the developed e-tongue system more comprehensible.

Electrochemistry fundamentals

Electrochemical cells are defined most generally as two electrodes separated by at least one electrolyte phase. In the electrochemical experiments, many factors affect the transport of the charge across the interface between the chemical phases, like an electric conductor (electrode) and an ionic conductor solution (electrolyte). At the electrode/electrolyte interface, the applied potential will generate a current flow: the movement of both electrons and holes transports the charge.

Since the reference electrode has a fixed potential, any changes in the cell are ascribable to the working electrode. So the potential of the working electrode is controlled with respect to the potential of the reference electrode, and through its potential is possible to control the energy of the electrons.

Driving the potential of the electrode to a more negative value, the energy of the electrons is raised: if the energy level is high enough the electrons can transfer into vacant electronic states on species in the electrolyte. In that case, a flow of electrons from electrode to solution (a reduction current) occurs (Figure 6.a). Similarly, imposing a more positive potential the energy of the electrons can be lowered: at some point electrons on solutes in the electrolyte will find a lower energy state on the electrode and will transfer there. Their flow, from solution to electrode, is an oxidation current (Figure 6.b). The critical potentials at which these processes occur are related to the standard potentials, E°, for the specific chemical substances in the system.

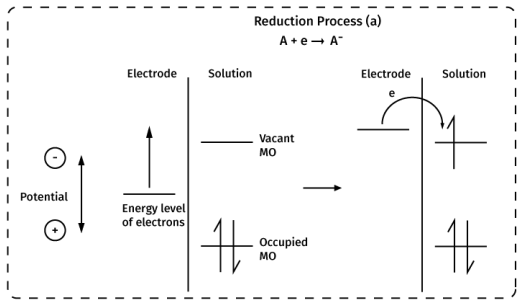

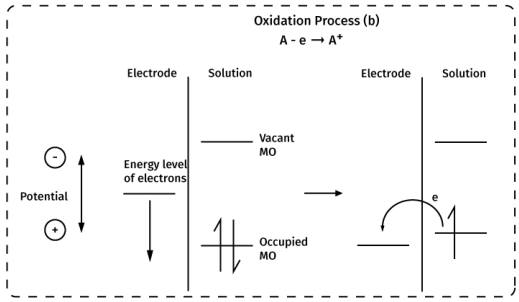

Figure 6: Representation of reduction (a) and oxidation (b) process of a species

In a typical electrochemical experiment, the working and the reference electrodes are immersed in the solution and the potential difference between the two electrodes is varied by an external power supply. The variation of the potential, E, can produce redox reactions and so a current because the electrons crossing the electrode/solution interface. The number of electrons that cross the interface is related to the extent of the chemical reaction: the current is related to the amounts of reactants consumed and product generated.

Faraday's law gives the relationship between charge and amount of product generated:

$$m = \left(\frac{Q}{F}\right)\left(\frac{M}{z}\right)$$

where:
m is the mass of generated substance at an electrode
Q is the total electric charge passed through the solution [C]
F = 96485 mol^{-1} is the Faraday constant
M is the molar mass of the susbstance [g/mol]
z is the valncy number of ions of the substance (number of electrons transferred per ion)

So 96,485.4 C causes 1 equivalent of reaction (e.g., consumption of 1 mole of reactant or production of 1 mole of product in a one-electron reaction).

The current, I, is the rate of flow of coulombs (or electrons), where a current of 1 ampere (A) is equivalent to 1 C/s.

Usually it's useful to plot the current (I) as a function of the potential (E): these curves can be quite informative about the solution, the electrodes and the reactions taking place at the solution/electrode interface.

Two types of phenomena can occur at the electrodes:

- Faradaic process: charges are transferred across the electrode-solution interface. Charges transfer causes oxidation or reduction processes governed by Faraday's law (the amount of chemical reaction caused by the flow of current is proportional to the amount of electricity passed).

- Non-faradic processes: under some conditions, applying a range of potentials to a specific electrode-solution interface, no charge-transfer reactions could occur because they are thermodynamically or kinetically unfavourable. However, other processes such as adsorption and desorption can occur changing the structure of the electrode-solution interface and so potential or solution composition. Although charges don't cross the interface, currents can flow when the potential, electrode area or solution composition change.

Both faradaic and non-faradaic processes occur when electrode reactions take place. The faradaic processes are usually of primary interest, but the effects of the non-faradaic processes must be taken into account in using electrochemical data to obtain information about the charge transfer and associated reactions.

Non-faradic processes

The ideal polarized electrode (IPE) is an electrode at which no charge transfer, across the electrode-solution interface, can take place regardless of the potential applied by an external voltage source (in real cases, in a limited range of potential).

Since charge cannot cross the IPE interface when the potential across it is changed, the behaviour of the electrode-solution interface is analogous to that of a capacitor and is governed by the equation:

$$\frac{q}{E} = C$$

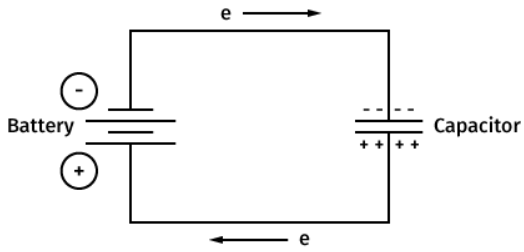

Figure 7: Charging a capacitor with a battery

Where q is the charge stored in the capacitor [C, coulombs], E is the potential applied on the two metal plates of the capacitor [V, volts] and C is the capacitance [F, farads]. When a potential is applied across the capacitor, a charging current will flow and charges will accumulate on its metal plates until:

$$q = C \cdot E$$

For example, if a potential difference of 2V is applied across a 10 μF capacitor, current will flow until 20 μC has accumulated on the capacitor plates. The magnitude of the current depends on the resistance of the circuit.

So the electrode-solution interface can be modeled as a capacitor, where one metal plate is the electrode and the other plate is the solution near the electrode: at a given potential, the metal electrode will accumulate a charge q_M and the solution will shown a charge q_S, with $q_M = -q_S$. The charge on the metal, q_M, represents an excess or deficiency of electrons and resides in a very thin layer (<0.1 Å) on the metal surface. The charge in solution, q_S, is made up of an excess of either cations or anions in the vicinity of the electrode surface.

All the charged species and oriented dipoles existing at the electrode-solution interface is called the electrical double-layer. At a given potential, the electrode-solution interface is characterized by a double-layer capacitance, C_d, typically in the range of 10 to 40 $\mu F/cm^2$. However, unlike real capacitors, whose capacitances are independent of the voltage across them, C_d is often a function of potential.

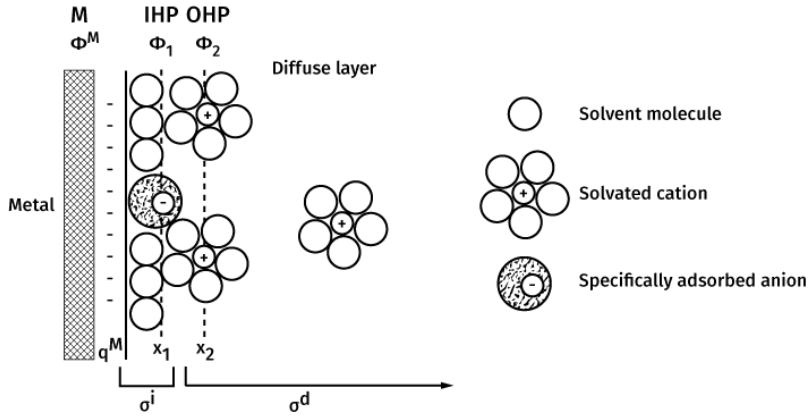

Figure 8: Electrical double-layer

The solution side plate of the capacitor is made up of several layers. The layer closest to the electrode contains solvent molecules and other species (ions or molecules) that are specifically adsorbed on the electrode surface. This inner layer is also called the compact, Helmholtz, or Stern layer.

The electrical center of the Helmholtz layer ions is located on the inner Helmholtz plane (IHP), at a distance x_1 from the electrode-solution interface plane. The total charge density from specifically adsorbed ions in this inner layer is σ^i ($\mu C/cm^2$). The Solvated ions can approach the electrode surface only to a distance x_2. The electrical center of these ions is called outer Helmholtz plane (OHP).

So interactions between solvated ions and the charged electrode involve only lomg-range electrostatic forces and are independent of the chemical properties of the ions that are non-specifically adsorbed. The non-specifically ions are distributed in a large region called the diffuse layer, which extends from the OHP to the bulk of the solution.

The charge density in the diffuse layer is σ^d and the total charge density of the solution side of the electrical double-layer is σ^S:

$$\sigma^S = \sigma^i + \sigma^d = -\sigma^M$$

The thickness of the diffuse layer depends on the total ionic concentration in the solution. The profile of the potential across the double-layer region is shown in the following figure:

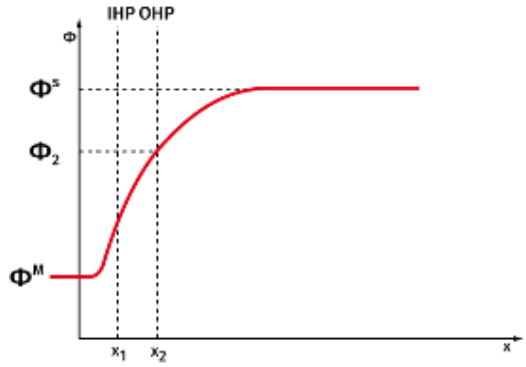

Figure 9: Potential profile across the double-layer region

The double-layer phenomenon can effect the rates of the reactions that take place on the electrode: if an electro-active specie, not specifically adsorbed, will be able to approach the electrode only to the OHP and it will interact with potential that is lower than the potential at the electrode-solution interface, because of the potential drop across the diffuse layer.

Under some conditions, when very low concentrations of electro-active species are present in the solution, the charging non-faradic current can be much larger than the faradic current produced by the redox reactions. So it is important to understand the behaviour of the charging current for some electrochemical experiments.

Consider a cell consisting of an IPE and an ideal reversible electrode. We can approximate such a system with an electrical circuit with a resistor, R_s, representing the solution resistance and a capacitor, C_d, representing the double layer at the electrode-solution interface:

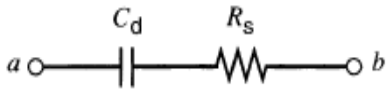

Figure 10: electrical equivalent of an IPE electrode

The C_d is usually function of the applied potential, so the model is accurate only if the potential doesn't change too much. It is possible to obtain useful information about the system applying a perturbation and observing the system behaviour.

Potential Step

If we apply a potential step to the IPE, the system will show the typical

behaviour of a RC circuit.

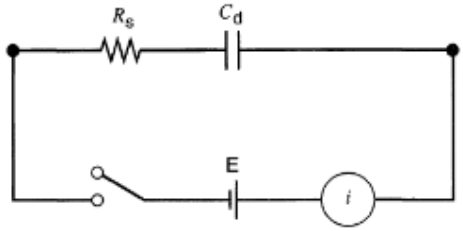

Figure 11: Potential step experiment

The total applied potential E can be expressed as:

$$E = E_R + E_C = iR_s + \frac{q}{C_d}$$

E_R is the potential drop across the resistor R_s
E_C is the potential drop across the capacitor C_d

$$i = \frac{dq}{dt} = \frac{-q}{R_s C_d} + \frac{E}{R_s}$$

assuming that initially the capacitor is fully uncharged (q=0 at t=0)

$$q = EC_d[1 - e^{\frac{-t}{R_s C_d}}]$$

$$i = \frac{E}{R_s} e^{-\frac{t}{R_s C_d}}$$

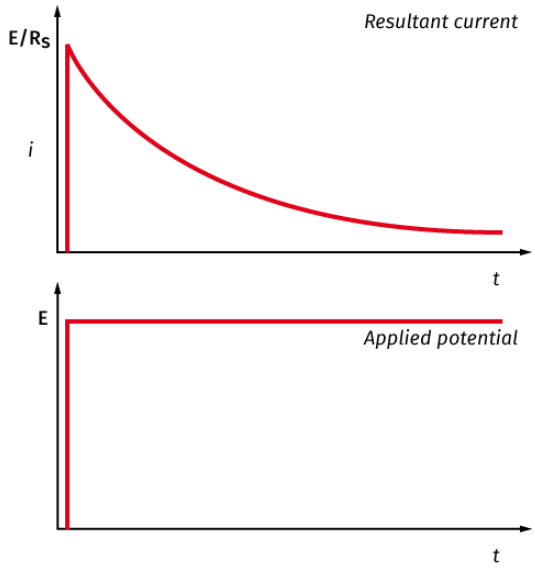

Figure 12: Current response for a potential step

Potential Ramp

A voltage ramp or linear potential sweep is a potential that increases linearly with time starting from an initial value (here assumed to be zero) at a sweep rate v (in Vs^{-1}):

$$E = vt$$

If such a ramp voltage is applied to the **RC** circuit, the following equation still applies:

$$E = E_R + E_C = iR_s + \frac{q}{C_d}$$

$$vt = R_s\left(\frac{dq}{dt}\right) + \frac{q}{C_d}$$

If q=0 at t=0,

$$i = vC_d[1 - e^{(\frac{-t}{R_s C_d})}]$$

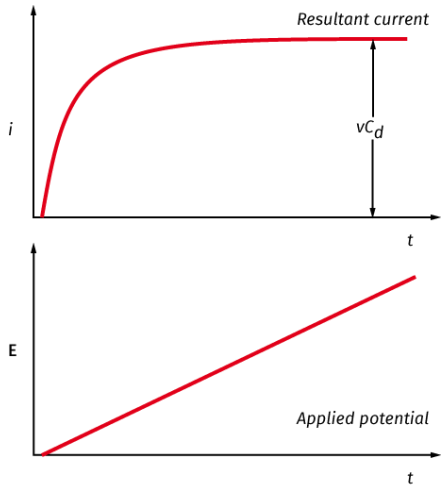

Figure 13: Current response for a potential ramp

If a triangular wave is applied, the following result is obtained:

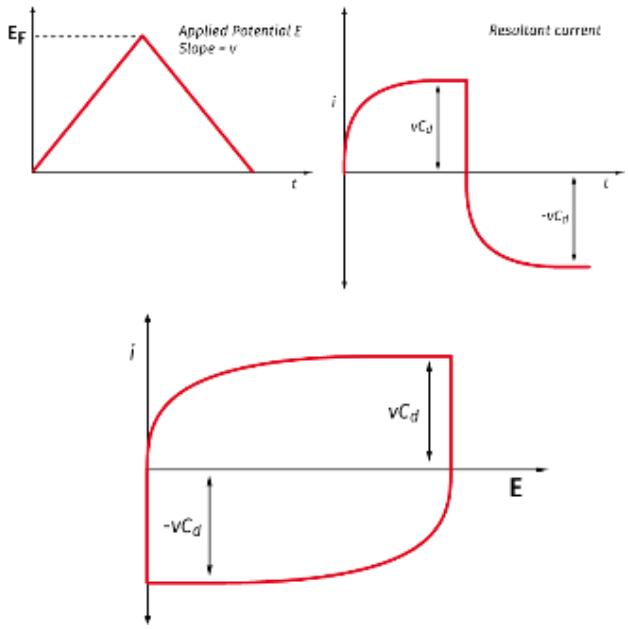

Figure 14: Current response for a cyclic linear potential sweep input

Faradic processes

Electrochemical cells producing faradaic currents are classified as *galvanic* or *electrolytic* cells:

- Galvanic cell: reactions occur spontaneously at the electrodes when a conductor connects them. This kind of cell is used to convert chemical energy into electrical energy.
- Electrolytic cell: reactions occur because of the application of an external voltage greater then the open-circuit potential of the cell. These cells are used to carry out specific chemical reactions by supplying external electrical energy.

In discussing cells, the electrode at which reductions occur is called *cathode*, and the electrode at which oxidations occur is called *anode*. A current in which electrons cross the interface from the electrode to a species in solution is a cathodic current, while electron flow from a solution species into the electrode is an anodic current. In an electrolytic cell, the cathode is negative with respect to the anode; but in a galvanic cell, the cathode is positive with respect to the anode.

The important parameters in an electrochemical cell are shown in the following figure:

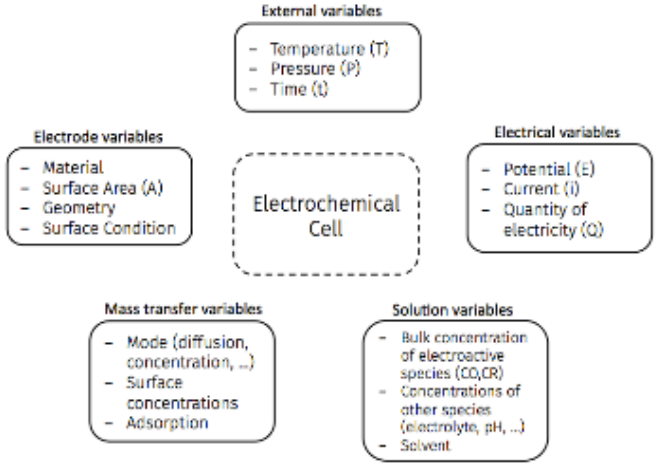

Figure 15: Important parameters in an electrochemical cell

To investigate the electrochemical behaviour of a specific solution it is possible to consider the electrochemical cell as a black box and observe its response to a certain applied perturbation (e.g. potential step). It is necessary to hold certain variables of the electrochemical cell constant and observe how other variables vary (usually current, potential or concentration) with changes in the input stimuli.

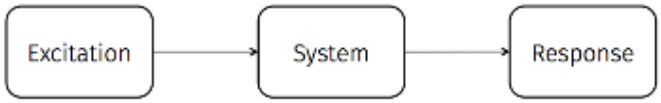

It will useful to consider more closely the nature of the current and the potential in an electrochemical cell. What is the current generated by a redox reaction? The faradaic current has a direct proportional relation with the electrolysis rate of the specie involved into the reaction:

$$i\ (amperes) = \frac{dQ}{dt}(coulombs/s)$$

$$\frac{Q}{nF}\left(\frac{coulombs}{coulombs/mol}\right) = N\ (mol\ electrolyzed)$$

where n is the stoichiometric number of electrons consumed in the reaction

$$Rate\ \left(\frac{mol}{s}\right) = \frac{dN}{dt} = \frac{i}{nF}$$

This is the rate for a type of reactions called *homogenous reaction* because it occurs everywhere in the electrochemical system at a uniform rate.

But understand the reaction rate on the electrode surface is more complex: the reactions that takes place on the electrodes are called *heterogeneous reactions* because they occur only on the electrode surface. Since the electrode reactions are heterogeneous their reaction rates are usually expressed in units of mol/s per unit of area:

$$Rate\left(\frac{mol}{s \cdot cm^2}\right) = \frac{i}{nFA} = \frac{j}{nF}$$

where j is the current density (A/cm^2)

Information about an electrode reaction is often gained by determining current as a function of potential (by obtaining i-E curves). If a cell has a defined equilibrium potential that potential is an important reference point of the system. The departure of the electrode potential (or cell potential) from the equilibrium value upon passage of faradaic current is called *polarization*. The extent of polarization is measured by the *over potential*, η:

$$\eta = E - E_{eq}$$

Current-potential curves, particularly those obtained under steady-state conditions, are sometimes called *polarization curves*.

Consider an overall electrode reaction, O + ne ⇌ R, composed of a series of steps that cause the conversion of the dissolved oxidized species, O, to a reduced form, R, also in solution. In general, the current (or electrode reaction rate) is governed by the rates of processes such as:

1. Mass transfer (e.g., of O from the bulk solution to the electrode surface).
2. Electron transfer at the electrode surface.
3. Chemical reactions preceding or following the electron transfer. These might be homogeneous processes or heterogeneous ones on the electrode surface.
4. Other surface reactions, such as adsorption, desorption, or crystallization (electro deposition).

The simplest reactions involve only mass transfer of a reactant to the electrode, heterogeneous electron transfer involving non-adsorbed species, and mass transfer of the product to the bulk solution. When a steady-state current is obtained, the rates of all reaction steps in a series are the same. The magnitude of this current is often limited by the inherent sluggishness of one or more reactions called rate-determining steps. The more facile reactions are held back from their maximum rates by the slowness with which a rate-determining step disposes of their products or creates their reactants.

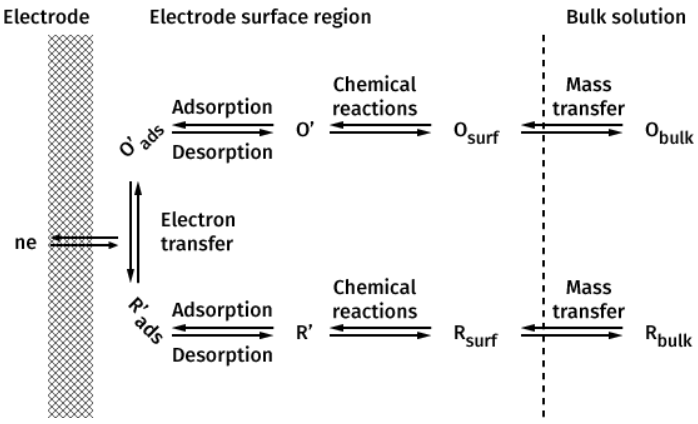

Figure 16: Reactions chain for a general redox process

So if we understand *i*, we must be able to describe the rate of the reaction, v, at the electrode surface.

$$Rate\left(\frac{mol}{s \cdot cm^2}\right) = \frac{i}{nFA} = \frac{j}{nF}$$

The simplest electrode reactions are those in which the rates of all associated chemical reactions are very fast compared to those of the mass-transfer processes. The surface concentrations on the electrode of the species

involved in the charge-transfer process will be related to the electrode potential by an equation on the Nernst form.

$$E = E^{0\prime} + \frac{RT}{nF} ln \frac{C_O}{C_R}$$

where:

E	is the half-cell reduction potential at the temperature of interest
$E^{0\prime}$	is the standard half-cell reduction potential
R	is the universal gas constant = 8.314472 J K^{-1} mol^{-1}
T	is the temperature in Kelvin
n	is the number of moles of electrons transferred in the cell reaction or half-reaction
F	is the Faraday constant, the number of coulombs per mole of electrons = 9.64853399 x 10^4 C mol^{-1}
C_O	is the concentration of the specie O
C_R	is the concentration of the specie R

The meaning of the Nernst's equation is that with an increased potential E the ratio $\frac{C_O^0}{C_{Or}^0}$ will increase and on the contrary with a reduced potential the ratio will decrease.

The net rate of the electrode reaction, v_r, is governed only by the rate at which the electroactive species reach the surface by mass transfer, v_{mt}.

$$v_r = v_{mt} = \frac{i}{nFA}$$

Such electrode reactions are often called reversible or *nernstian*, because the principal species obey thermodynamic relationships at the electrode surface.

The modes of mass transfer are:

1. Migration: movement of a charged body under the influence of an electric field (a gradient of electrical potential).
2. Diffusion: movement of a species under the influence of a gradient of chemical potential (a concentration gradient).
3. Convection: stirring or hydrodynamic transport. Generally fluid flow occurs because of natural convection (convection caused by density gradients) and forced convection, and may be characterized by stagnant regions, laminar flow, and turbulent flow.

Usually voltammetry technique is applied to reversible processes that present only diffusive phenomena, and therefore it will be possible to study the reaction trough Fick's law. Consider the reduction of a species O at a cathode O + ne ⇌ R. Once electrolysis of species O begins, its concentration at the electrode surface, C_o(x = 0) becomes smaller than the value, C_O^*, in the *bulk solution* (far from the electrode). We assume here that stirring is ineffective at the electrode surface, so the solution velocity term need not be considered at x = 0. This simplified

treatment is based on the idea that a stagnant layer of thickness δ_o exists at the electrode surface (Nernst diffusion layer), with stirring maintaining the concentration of O at C_O^* beyond x = δ_o. Since we also assume that there is an excess of supporting electrolyte, migration is not important, and the rate of mass transfer is proportional only to the concentration gradient at the electrode surface:

$$v_{mt} \propto \left(\frac{dC_o}{dx}\right)_{x=0} = D_o \left(\frac{dC_o}{dx}\right)_{x=0}$$

Assuming a linear concentration gradient within the diffusion layer close to the electrode surface:

$$v_{mt} = D_o \frac{[C_o^* - C_o(x=0)]}{\delta_o}$$

or:

$$v_{mt} = m_o[C_o^* - C_o(x=0)]$$

where m_o is the *mass-transfer coefficient* (cm/s).

$$\frac{i}{nFA} = m_o[C_o^* - C_o(x=0)]$$

$$\frac{i}{nFA} = m_R[C_R(x=0) - C_R^*]$$

The values of $C_o(x=0)$ and $C_R(x=0)$ are functions of the electrode potential, E. The largest rate of mass transfer of O occurs when $C_o(x=0) \ll C_o^*$. The value of the current under these condition is called *limiting current*:

$$i_l = nFAm_oC_o^*$$

and

$$C_o(x=0) = \frac{i_l - i}{nFAm_o}$$

When the limiting current flows, the electrode process is occurring at the maximum rate possible because O is being reduced as fast as it reaches the electrode surface.

If R is initially absent, $C_R^* = 0$ and $C_R(x=0)$ is:

$$C_R(x=0) = \frac{i}{nFAm_R}$$

$$E = E^{0\prime} - \frac{RT}{nF} ln \frac{m_O}{m_R} + \frac{RT}{nF} ln\left(\frac{i_l - i}{i}\right)$$

when $i = i_l/2$:

$$E = E_{1/2} = E^{0'} - \frac{RT}{nF} ln \frac{m_O}{m_R} \rightarrow E = E_{1/2} + \frac{RT}{nF} ln \left(\frac{i_l - i}{i} \right)$$

where $E_{1/2}$ is independent of the reactant concentrations and is characteristic of the O/R system.

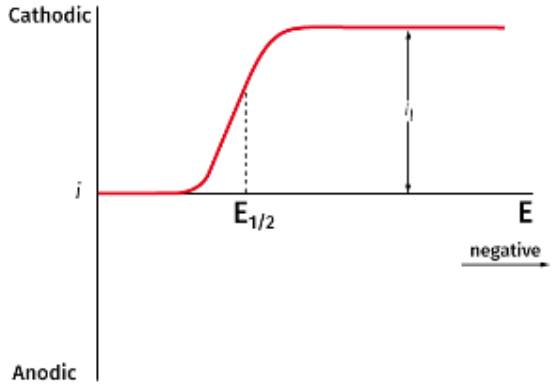

Figure 17: Current vs potential curve for a nernstian reaction involving two soluble species with only oxidant present initially.

Development of a Novel E-tongue System

Introduction

The e-tongue system is based on an electrochemical analytical technique called cyclic-voltammetry.

Voltammetry is an electrochemical technique used to study a compound, a biological material, or an electrode surface. In voltammetry we apply a time-dependent potential to an electrochemical cell and measure the resulting current as a function of that potential.

The electrochemical cell used in voltammetry is, in most cases, made of three electrodes, respectively called working, reference and counter electrode.

A time-dependent potential excitation signal is applied between the working electrode and the reference electrode and the current that flows between the working and auxiliary electrodes is measured. Current peaks, observed at specific applied voltages, are due to specific redox reactions running on the working electrode surface.

Cyclic Voltammetry (CV) consists of cycling the potential of the working electrode: the excitation signal for CV is a linear potential scan with a triangular waveform with bipolar range.

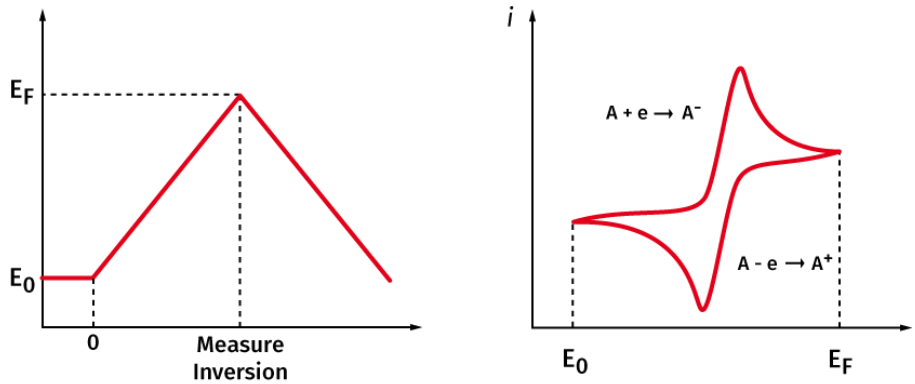

Figure 18: Typical voltammogram curve for a reversible redox reaction

The voltammogram is a display of current (vertical axis) versus potential (horizontal axis) because the potential varies linearly with time, the horizontal axis can also be thought of as a time axis. This is helpful in understanding the fundamentals of the technique.

Cyclic voltammetry (CV) is perhaps the most versatile electro-analytical technique for the study of electro-active species. Cyclic voltammetry is often the first experiment performed in an electrochemical study. The effectiveness of CV results from its capability for rapidly observing the redox behaviour over a wide potential range.

System design and realization

A complex system, inspired by the electrochemical technique above described, has been designed and implemented to perform cyclic-voltammetic analysis on liquid sample. The system consists of the following elements:

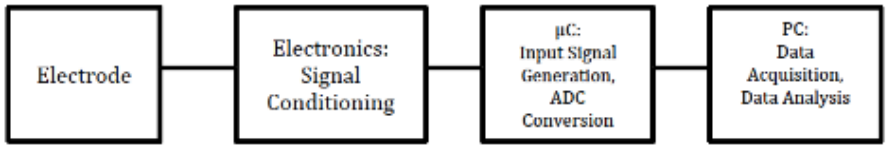

Figure 19: Block diagram of the e-tongue system

Electrodes

All electrochemical cells require at least two electrodes, since the potential of a given electrode can only be measured relatively to another reference electrode, which should have a constant potential.

Otherwise in voltammetric analysis, it is necessary to apply a potential E to an electrode and simultaneously monitor the resulting current flowing in the cell. A two electrodes system could not work properly because of the potential drop caused by the resistance of the solution and the polarization of the auxiliary electrode, necessary for the measurement of the current [53]. A suitable control of the potential is achieved using a three-electrode system using a potentiostat to monitor the potential of the working electrode (WE) than the reference electrode (RE) while the current flows across the WE and counter electrode (CE).

Working electrodes – WE

The working electrode works as a source or a drain of electrons to allow an optimal electrons transfer with the surrounding solution. It has to be made of a conductive material that is electrochemically inert in the potential range of the electrochemical experiment.

The most used materials for the WE are platinum, gold, glassy-carbon, mercury, pyrolytic graphite and other metal and semiconductor materials. The use of mercury film electrodes [54] is due to the inert behaviour of mercury in a wide range of negative potential and the ability to regenerate its surface applying a drop or a thin layer of film of new mercury.

A regular and well-defined shape of the WE allows a good control of the surface area exposed to the analyte: this is very important for the quantitative interpretation of the results of the CV experiments.

Reference electrodes – RE

The reference electrode should primarily be able to maintain a known and constant potential during the measurement. If an electrode doesn't vary its

potential, because of a current, is called non-polarizable ideal electrode: the impedance of an ideal reference electrode should be null.

Usually the passage of a current through an electrode can degrade the potential [55] and so a real non-polarizable electrode is used: this kind of reference electrode has high input impedance so that a negligible current flows through it.

The reference electrode is mostly realized [56] with a Saturated Calomel Electrode (SCE), Hg /Hg_2Cl_2, or with silver/silver chloride electrode, Ag/AgCl. The SCE electrode is a reference electrode based on the reaction between elemental mercury and mercury chloride (calomel). The aqueous phase in contact with the mercury and Hg_2Cl_2 is a saturated solution of potassium chloride in water. For years this has been the most widely used reference electrode. The silver/silver-chloride electrode is made of a silver wire, coated with silver chloride immersed in a solution containing chloride ions, such as KCl. The two reference electrodes have a similar behaviour, since they involve a redox reaction between a poorly soluble chloride and the metal element in a chloride aqueous solution.

Another type of traditionally used reference electrode [57] for cyclic voltammetry applications is the Hg/Hg_2SO_4, made of mercury, mercury sulphate and a saturated solution of potassium sulphate: this electrode is designed for certain applications where it is preferable not to use chloride ions.

Counter Electrode – CE

The counter electrode, or auxiliary electrode, can be made of any material with high conductivity and with an inert behaviour in the experiment conditions: the counter electrode is usually a platinum wire or a graphite rod with an adequate surface area.

During the voltammetric measurement, on the surface of the CE occurs a redox reaction to balance the reaction that occurs on the WE: the products of this reaction can diffuse towards the working electrode and interfere with it. However in cyclic voltammetry experiments the time-scale is short enough to avoid significant interference.

E-Tongue electrodes

The e-tongue device uses two types of electrodes:

- Commercial Screen-Printed Electrodes (Dropsens, Spain)
- Custom Micro-Fabricated Electrodes

Screen-Printed Electrodes

The system can use commercial screen printed electrodes made by Dropsens (ref. code 250BT): the working electrode is made of gold and has a diameter of 4mm, the counter electrode is made of platinum, the reference electrode is made of silver and all the other electric contacts are made of silver. The support material is ceramic and the total thickness of the electrode is 1mm. The thickness of the metal material screen-printed on the electrode is about 1µm. The surface roughness is quite high.

Figure 20: Used electrodes (Dropsens 250BT)

A specific connector and cable are used to interface the screen-printed electrode with the electronic device: the cable provides four connections, one for each electrode (WE, RE and CE) and the last one for the cable shield. The cable ends with four male pins with a diameter of 2mm and with four detachable crocodile clips. The cable is made by Dropsens and has the ref. code CAC.

Figure 21: Electrode connector (Dropsens CAC)

Micro-Fabricated Electrodes

Custom micro-fabricated electrodes were designed and realized to improve the performances of the e-tongue system. The main aim was to have complete control on the fabrication of the electrodes: using a micro-fabrication process it is possible to control the thickness of metal layers, the purity of the materials and the surface roughness.

The electrodes were fabricated in the Integrated Circuit Processing lab of the Else Kooi Laboratory in the TU Delft (Delft University of technology). The micro-fabrication process was realized thanks to the cleanroom facilities provided by the ECTM group (Electronic Components, Technology and Materials) under the supervision of Professor Lina Sarro.

The electrodes were designed to be compatible with the connection cable made by Dropsens, so the external connection layout of the electrode is the same of the screen-printed electrodes. The metals used in the micro-fabricated electrode are: gold for the working electrode and the external connections, silver for the reference electrode and platinum for the counter electrode.

The fabrication process of the electrode includes several micro-fabrication steps with three successive lift-off processes. Fabrication steps are summarized in the following chart:

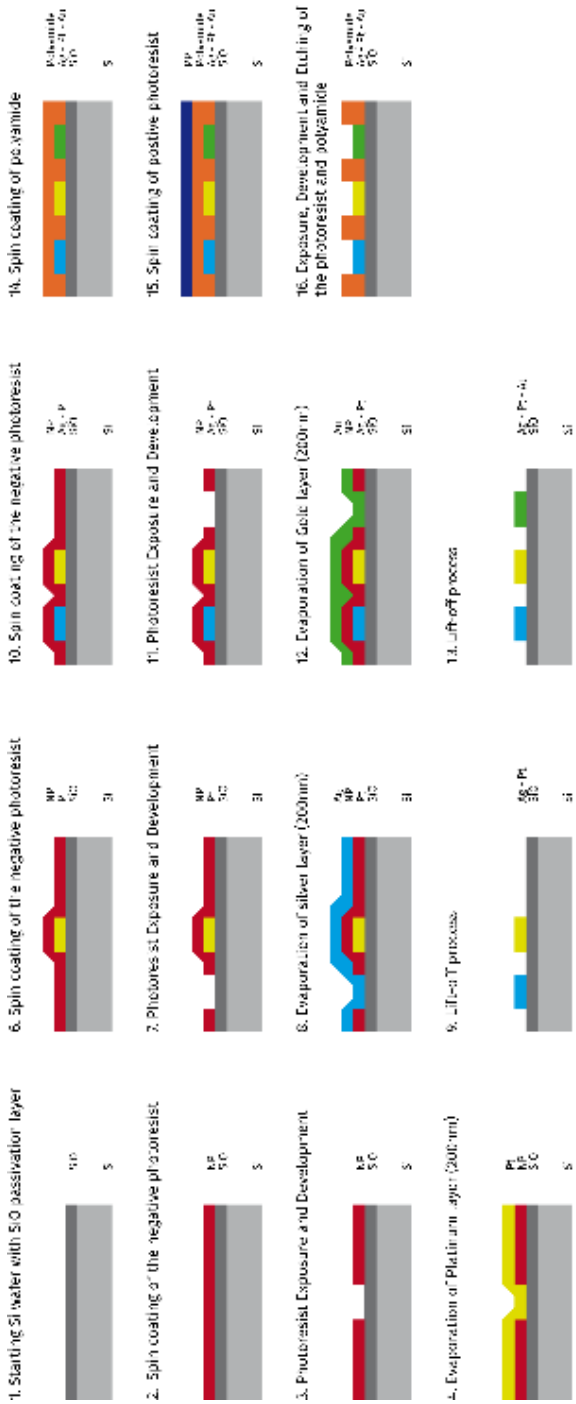

Figure 22: Micro-fabrication steps

Detailed workflow

1. Platinum layer process:
    - Spin coating of the negative photoresist
    - Exposure of the photoresist with a negative mask
    - X-link bake
    - Development of the exposed photoresist
    - Visual Inspection of the wafers
    - DUV Bake
    - O2 Plasma flash
    - Evaporation of Platinum layer – 200nm
    - Lift-off procedure in a ultrasonic bath of NMP (N-metil-2-pirrolidone) Solvent
    - Rinsing with DI water and drying
    - O2 plasma cleaning
2. Silver layer process:
    - Spin coating of the negative photoresist
    - Exposure of the photoresist with a negative mask
    - X-link bake
    - Development of the exposed photoresist
    - Visual Inspection of the wafers
    - DUV Bake
    - O2 Plasma flash
    - Evaporation of Silver layer – 200nm
    - Lift-off procedure in a ultrasonic bath of NMP (N-metil-2-pirrolidone) Solvent
    - Rinsing with DI water and drying
    - O2 plasma cleaning
3. Gold layer process:
    - Spin coating of the negative photoresist
    - Exposure of the photoresist with a negative mask
    - X-link bake
    - Development of the exposed photoresist
    - Visual Inspection of the wafers
    - DUV Bake
    - O2 Plasma flash
    - Evaporation of Gold layer – 200nm
    - Lift-off procedure in a ultrasonic bath of NMP (N-metil-2-pirrolidone) Solvent
    - Rinsing with DI water and drying
    - O2 plasma cleaning
4. Polyamide layer process:
    - Spin coating of the polyamide
    - Spin coating of the positive photoresist
    - Exposure of the photoresist with a positive mask
    - Development of the photoresist and etching of the polyamide layer with a TMAH (Tetramethylammonium hydroxide) solution
    - Photoresist stripping

- Polyamide thermal polymerization

Comparison of Screen-printed and Micro-fabricated Electrodes

The micro-fabricated electrodes (MF electrodes) were compared with the commercial screen-printed electrode (SP electrodes) in order to match the electrochemical performances. The electrodes were tested using a high-end potentiostat by Metrohm, the Autolab PGSTAT302N.

Figure 23: Micro-fabricated electrode (left) and Commercial screen printed electrode (right)

Cyclic voltammetry experiments were performed using a solution of DI water containing ferrocyanide ions $Fe(CN)^{4-}$ with different concentrations (0.1, 0.5, 1, 2, 3, 4 mMol). The ferrocyanide was chosen because it produces a reversible redox reaction and is widely used in electrochemical experiments. The experiments were performed applying to the electrode immersed in the solution a triangular wave ranging from -0.25 and 0.6 V with a scan rate of 0.04 V/s.

Figures 24 and 25 show respectively the behaviour of the micro-fabricated and screen-printed electrodes:

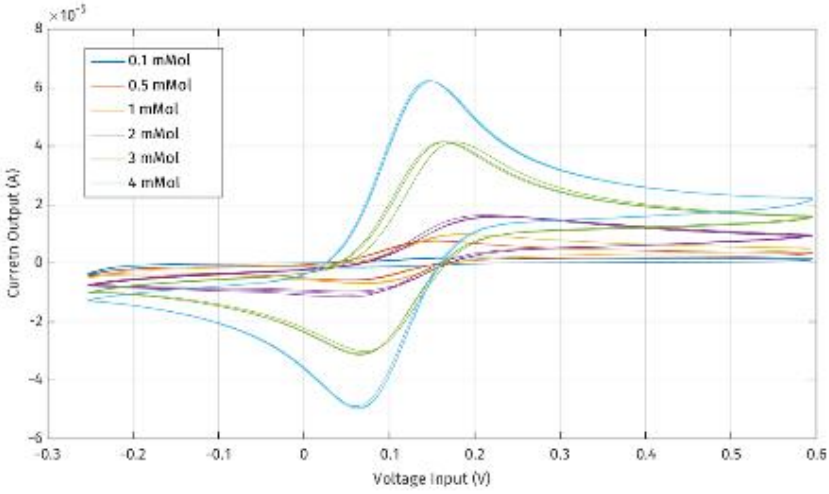

Figure 24: Cyclic voltammetry curves of the screen-printed electrodes for different concentrations of ferrocyanide

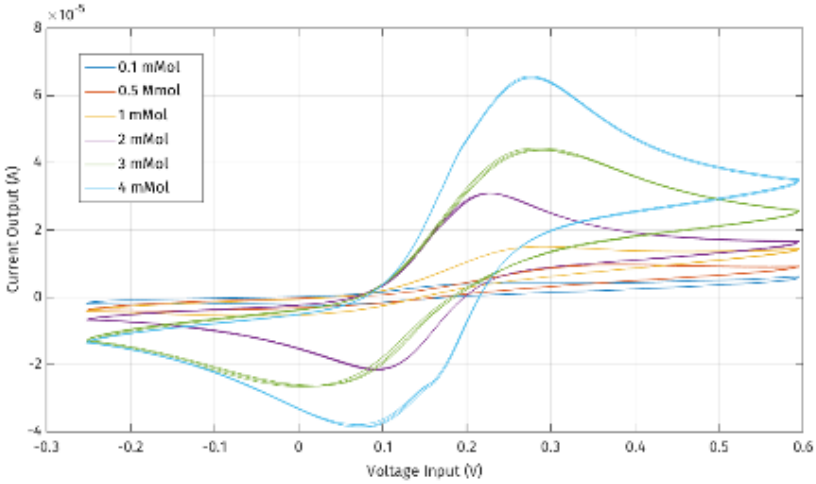

Figure 25: Cyclic voltammetry curves of the micro-fabricated electrodes for different concentrations of ferrocyanide

The curves of both the MF electrodes and the SP electrodes show the typical result of the cyclic voltammetry study of ferrocyanide that presents a reversible redox reaction:

$$[Fe(CN)_6]^{4-} \leftrightharpoons [Fe(CN)_6]^{3-} + e^-$$

When the input voltage exceeds 0.1 V the oxidation of the specie occurs and the anodic current peaks is between 0.2 and 0.3 V depending on the concentration of the reactant. The input voltage decreasing triggers the reduction process.

The oxidation current peaks are proportionally related to the concentration of ferrocyanide in the solution: so it is possible to fit the experimental data in order to observe this relationship.

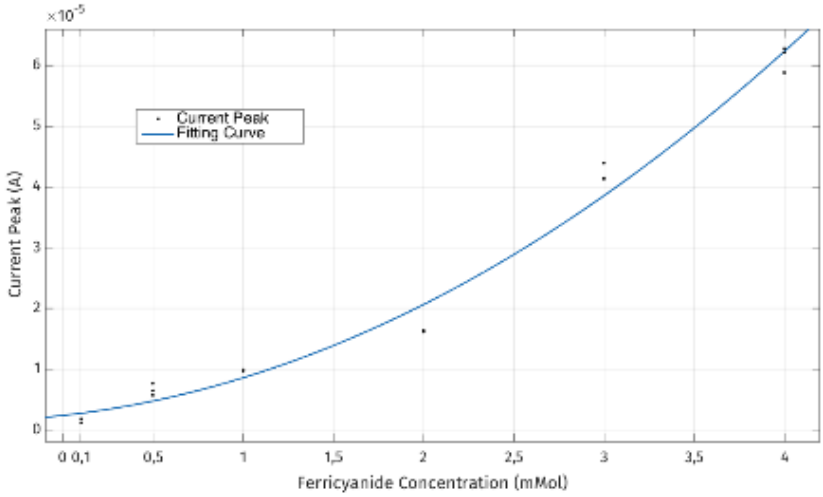

Figure 26: Current peaks data versus Ferrocyanide concentrations for the screen-printed electrodes. Three experimental values of the current peak are considered for each concentration.

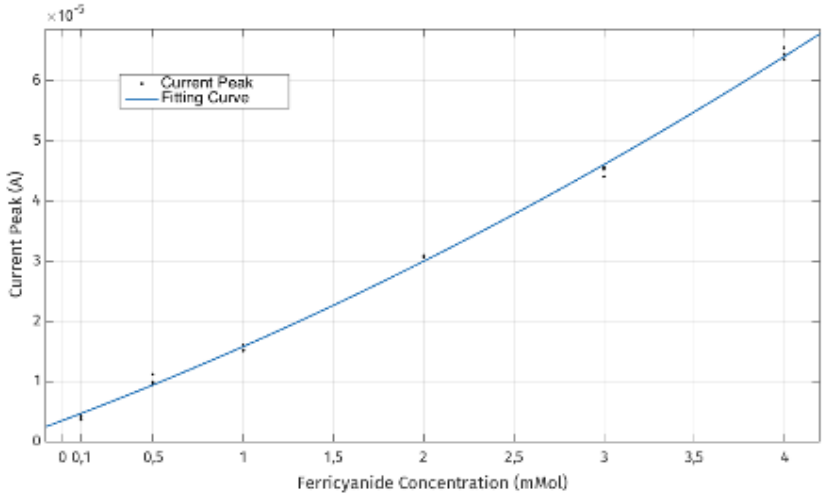

Figure 27: Current peaks data versus Ferrocyanide concentrations for the micro-fabricated electrodes. Three experimental values of the current peak are considered for each concentration.

The output current data can be interpolated with quadratic function and the sensorial characteristic of the electrodes can be evaluated:

	Screen-Printed Electrodes
Interpolating function	$2.93 \cdot 10^{-6}x^2 + 3.28 \cdot 10^{-6}x + 2.36 \cdot 10^{-6}$
R-square factor	0.9839
Sensitivity function	$5.86 \cdot 10^{-6}x + 3.278 \cdot 10^{-6}$
LOD (noise current 10nA)	$0.0031\ Mol$

	Micro-Fabricated Electrodes
Interpolating function	$9.51 \cdot 10^{-7}x^2 + 1.13 \cdot 10^{-5}x + 3.54 \cdot 10^{-6}$
R-square factor	0.9939
Sensitivity function	$1.9 \cdot 10^{-5}x + 1.13 \cdot 10^{-5}$
LOD (noise current 10nA)	$0.0009\ Mol$

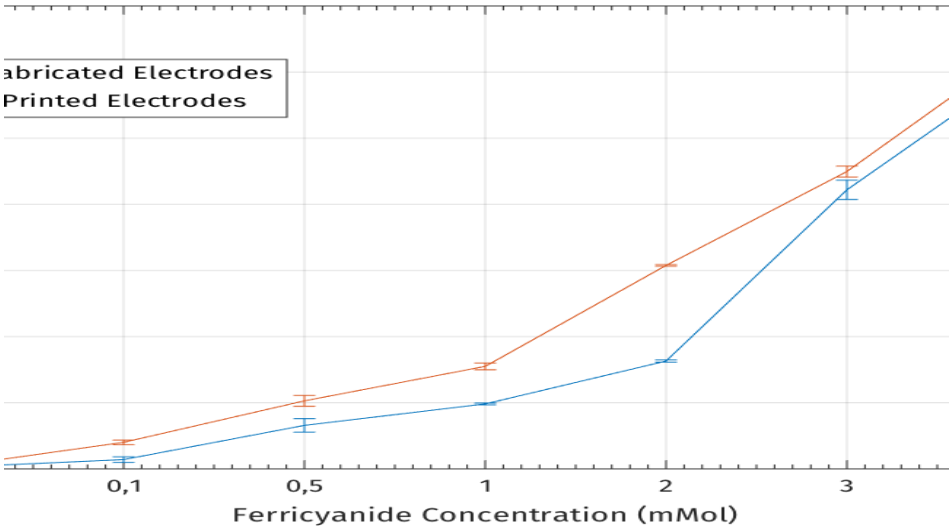

Figure 28: Mean values and standard deviations of the output current peaks

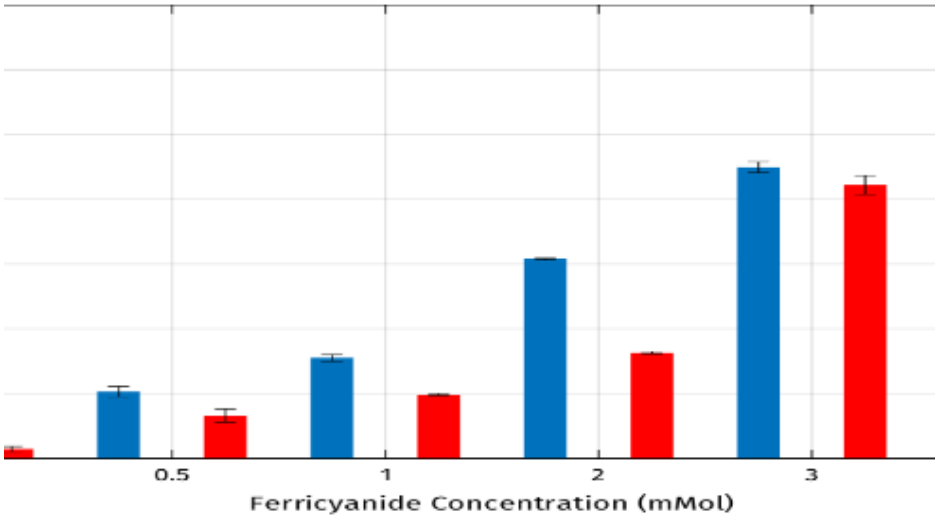

Figure 29: Mean values and standard deviations of the output current peaks

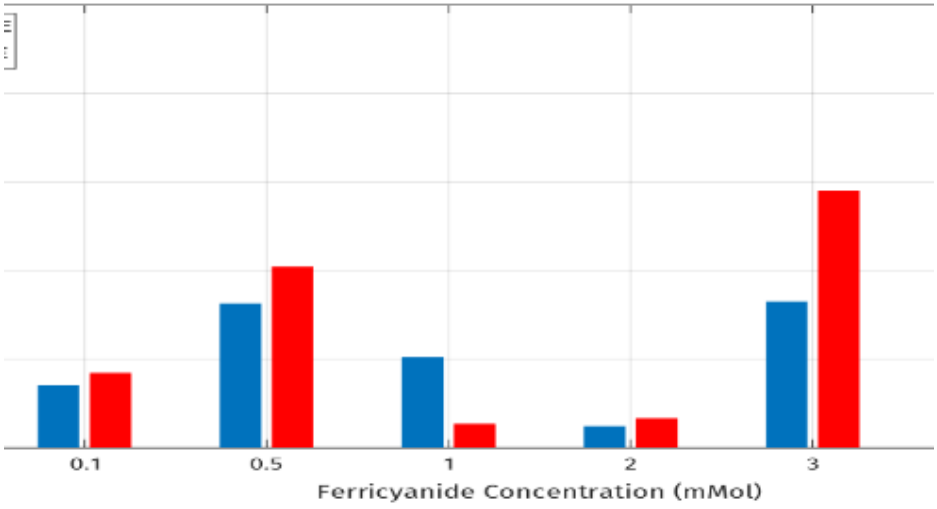

Figure 30: Standard deviations of the output current peaks

It is also possible to evaluate the precision of the experimental data generated with the two types of electrodes. Considering figures 28, 29 and 30, it is possible to compare standard deviations of five repeated measurements per concentration for each electrode: it's evident that micro-fabricated electrodes produce more precise measurements with a lower standard deviation error and a higher current peak mean value.

Thus it has been demonstrated experimentally that the micro-fabricated electrodes own a lower LOD (Limit of Detection) and produce more repeatable measurements.

Signal conditioning and Data Acquisition: first prototype

The first experimental tests on the signal conditioning stage were performed using a potentiostatic circuit and laboratory equipment:

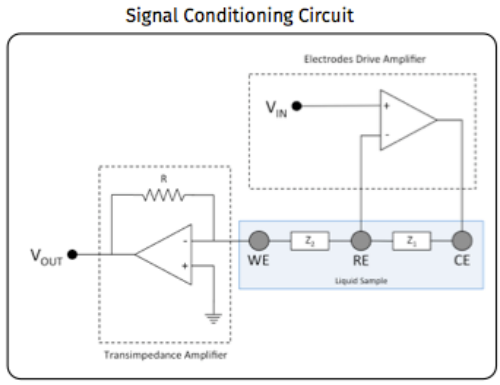

Figure 31: Scheme of the signal conditioning circuit stage: this stage includes an electrodes driver circuit and a trans-impedance circuit.

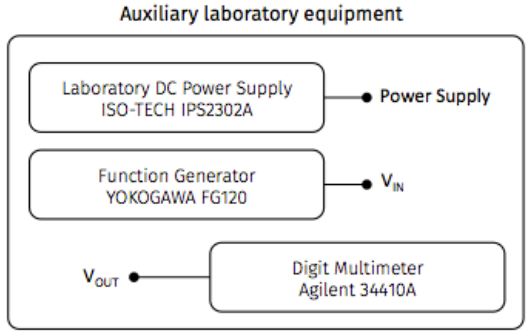

Figure 32: Auxiliary laboratory equipment used to perform the tests

Commercial screen-printed electrodes by Dropsens (cod. 250BT) were used: WE is made of gold and has a diameter of 4mm, RE is made of silver and CE is made of platinum.

The DC power voltage is supplied by a Laboratory DC Power Supply (ISO-TECH IPS2302A): the op-amps used in the signal conditioning stage are powered with a dual supply voltage of ±10V. The input signal is supplied by a function generator device (YOKOGAWA FG120) and is a triangular waveform ranging from -1 V to +1 V with a frequency of 0.01 Hz (scan rate of 40mV/s). The output signal is

acquired by a Digital Multimeter (Agilent 34410A) connected to a PC. The output data are analysed on a PC using specific statistical analysis techniques in MATLAB.

Observing the electrodes driver amplifier in Figure 16, it's clear that the op-amp allows the reference electrode RE to maintain a constant voltage: in fact current cannot flow through it because of the high input impedance of the amplifier. The potential of the WE is constant and equal to the op-amp input reference voltage that is zero because it is connected to the ground.

Thus the current that flows across RE and WE is:

$$i = \frac{V_{RE} - V_{WE}}{Z_2}$$

where Z_2 is the impedance related to the redox reactions that occur in the liquid solution, triggered by the voltage drop across WE and RE. So the current is voltage-dependent.

The trans-impedance stage has the task of converting the current into a voltage: it converts the current flowing across the WE in an output voltage to be acquired by the Digital Multimeter. The voltage output signal is acquired with a sample-rate of 1s and then, for each triangular scan, 100 samples will be recorded.

Output data are processed using PCA (Principal Component Analysis) techniques in a specific MATLAB toolbox. The cyclic-voltammetry curves (i versus V) are generated using MATLAB. Three water samples were analysed to carry out the initial tests of the measuring system: the samples are very different among them, considering in particular the dry residue value:

	Dry residue (mg/L)	Electrical conductivity **(µs/cm)**	Calcium (mg/L)	Bicarbonates (mg/L)	Sodium (mg/L)	Potassium (mg/L)
Distilled water	0	1	0	0	0	0
Bottle-water **"Panna"**	141	222	32	103	6,7	0,9
Bottle-water **"S.Gemini"**	932	1365	326	1155	19,5	3,4

Table 4: Comparison chart of the water samples.

To verify the repeatability of the measuring system, it is necessary to carry all the repeated measurements on the same measurands and under the same experimental conditions.

Each sample is measured applying a triangular voltage waveform, as input signal, between the WE and the RE. The input voltage ranges from -1 V to +1 V with a frequency of 0.01 Hz. The generated current, flowing across the WE, is measured. The output signal is acquired every 1 s generating an array of 100 values per voltammetry cycle.

The resulting cyclic voltammetry curves or fingerprints (i versus V) are shown:

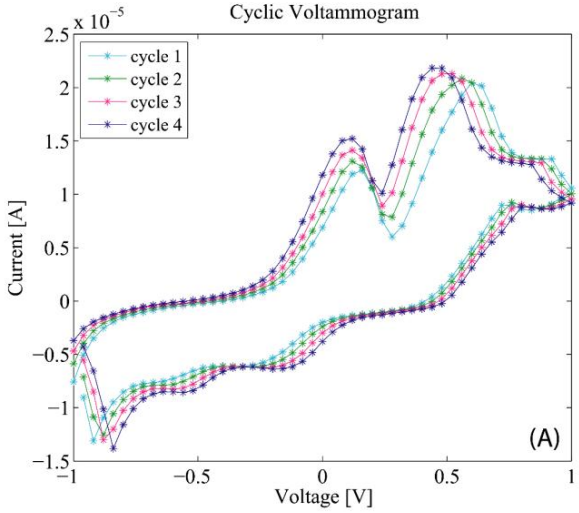

Figure 33: Cyclic voltammetry graph of a sample of "Levissima" water.

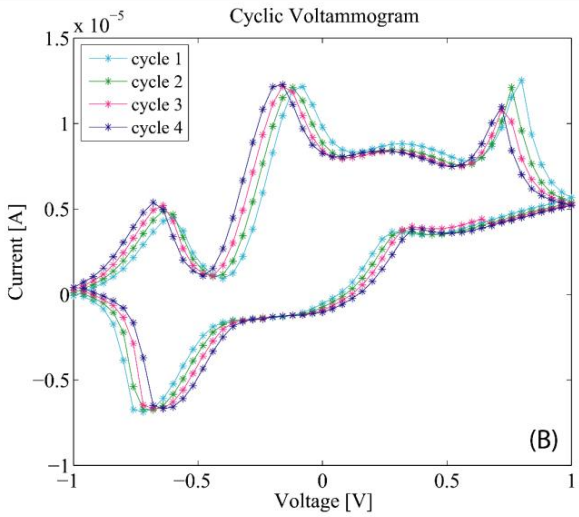

Figure 34: Cyclic voltammetry graph of a sample of "Panna" water.

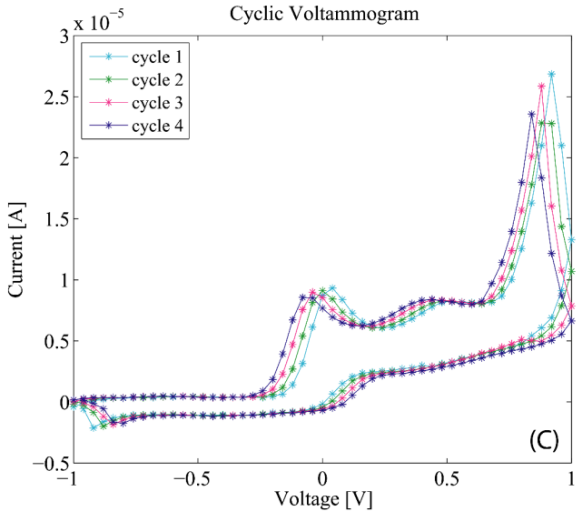

Figure 35: Cyclic voltammetry graph of a sample of "S. Gemini" water.

The repeated measuring cycles show a good repeatability of the measuring system. The chemical and physical properties of the analysed samples are different enough to allow a visual discrimination of the samples just comparing the cyclic voltammetry graphs.

The obtained three cyclic voltammetry charts have three distinct trends for the three samples, presenting characteristic current peaks corresponding to specific applied potential input.

The discriminant capability of the system was also investigate. In the following score plots, the results of the PCA analysis are shown; the two figures show the PCA of the output data obtained by a double measurement of each sample performed with two different electrodes:

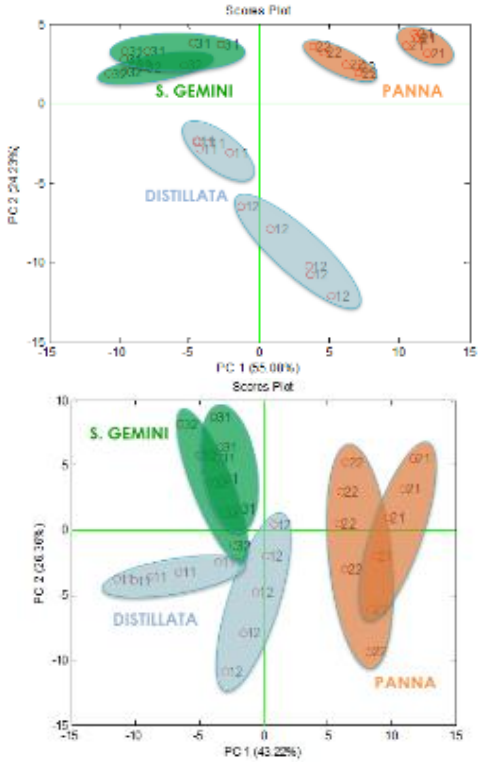

Figure 36: Score plots of the PCA analysis of the three water samples.

The Scores Plot shows a good discrimination of the three samples of water (Distilled, "Panna" and "S. Gemini").

Signal conditioning and Data Acquisition: second prototype

Since the first tests of the feasibility study produced satisfying results, it was possible to continue with the engineering and integration process of the measuring device.

The use of the laboratory equipment, as first approach, had the aim of studying the output signal and optimizing the measuring parameters (e.g., input voltage range, scan rate) to obtain the best reproducibility and stability of the system. The integration of the system is part of an engineering process to make the device portable and "user-friendly".

Moving from a laboratory measuring system to an integrated device, some working parameters changed because of the characteristics of the applied electronic solutions. These variations were analysed to monitor their effects on the final correct operation: in particular the frequency of the input triangular signal and the power supply circuit were analysed.

The power supply function, first provided by a Laboratory DC Power Supply (ISO-TECH IPS2302A), was replaced with a custom designed circuital solution:

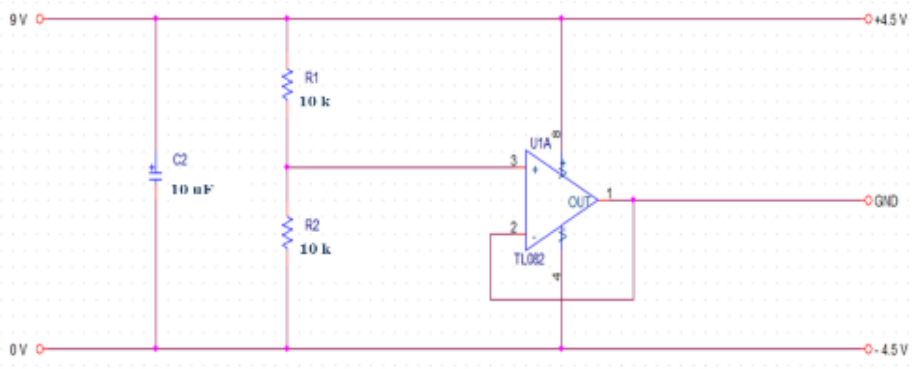

Figure 37: Schematic of the Split-supply circuit.

The potentiostatic circuit was tested for different power supply values: in particular, the performances of the first prototype dual power supply (± 10 V) were compared with the performances of the system powered by the integrated solution (split-supply circuit ± 4.5 V). The choice of these power supply values (± 4.5 V) is the due to the use of a 9 V battery.

The visual comparison of the fingerprints obtained with the different power supply voltages doesn't indicate substantial differences in the possible classification of the analysed samples:

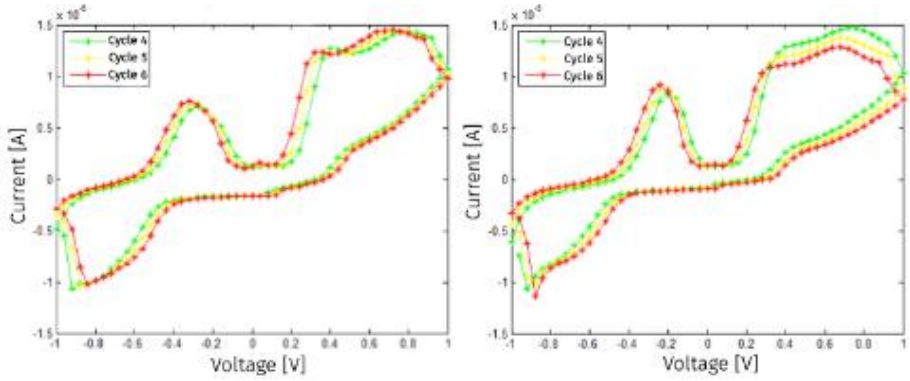

Figure 38: Left: cyclic voltammetry plots of a S. Gemini sample analysed using a dual power supply of ±10V. Right: cyclic voltammetry plots of a S. Gemini sample analysed using a dual power supply of ±4.5V

The score plot in figure 39 shows that there is no significant differences in the classification results obtained using the PCA technique:

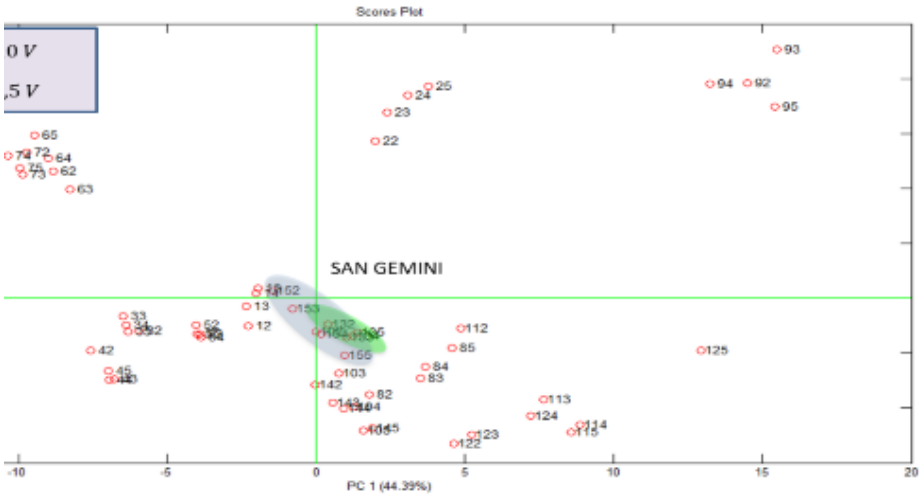

Figure 39: Score plot of the PCA analysis of several water samples, including "S. Gemini" samples. Investigations on the relationship between the frequency of the input signal and the performances of the system were performed. In the first prototype system, the input signal has a frequency of 0.01 Hz, ranging from -1 to +1 V. The output signal is acquired with a sampling rate of 1 sample per second; so for each scan, 100 samples are recorded. The cyclic potential scan is repeated for 5 consecutive times, recording 500 samples.

In order to guarantee the same number of acquired samples, the sampling rate was adapted to the specific frequency of the input signal. Four frequencies were tested: 0,005 Hz, 0.01 Hz, 0.05 Hz and 0.1 Hz.

Frequency	Samples number	Sampling rate	Cycles	Measure time
0.005 Hz	100	0.5 sample/s	5	16' 46''
0.01 Hz	100	1 sample/s	5	8' 23''
0.05 Hz	100	5 sample/s	5	1' 43''
0.1 HZ	100	10 sample/s	5	53''

Table 5: Tested frequency of the input signal.

The results with higher informative content are those obtained with the input signal frequencies of 0.005 and 0.01 Hz.

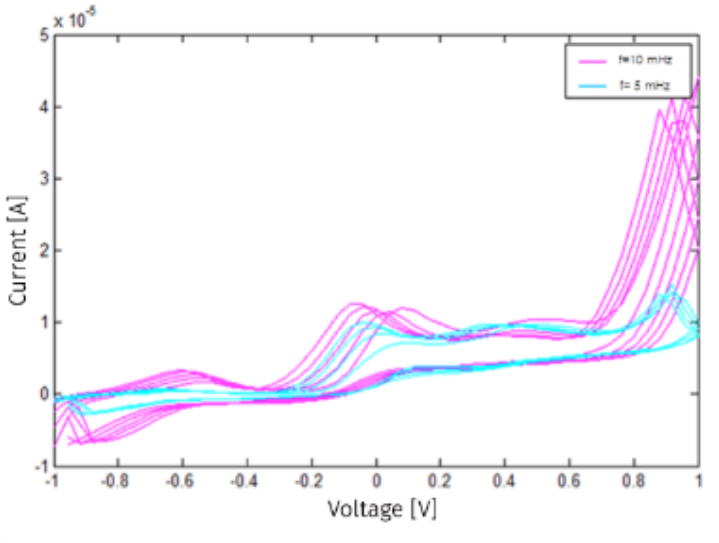

Figure 40: comparative chart of output data for two input signals with different frequencies.

The i/V chart shows the existing relationship between the current peaks and the scan rate of the input signal: the intensity of the current peaks increases with the increasing of the scan rate.

The input signal generator, first represented by a Function Generator device (Yokogawa FG120) was replaced with an integrated circuit.

An XR-2206 (EXAR Corporation, USA) was used to replace the Yokogawa function generator: this integrated circuit can generate tuneable waveforms (triangular, sine and quadratic) if properly implemented with few external components.

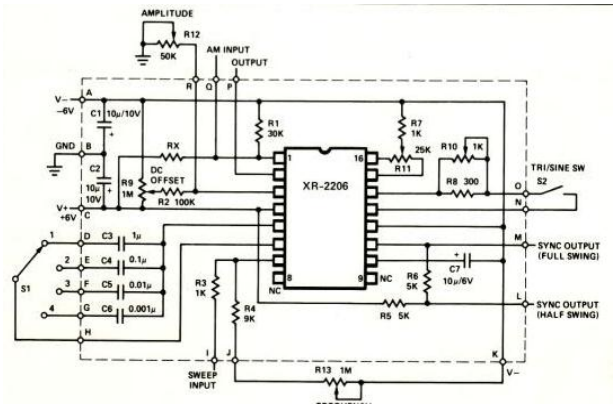

Figure 41: circuit configurations for typical applications

Therefore the XR-2206 replaces the Test Function Generator (Yokogawa FG120) generating an input signal with a triangular waveform that ranges from -1 to

+1 V with a frequency of 10mHz, that is exactly the same signal generated using the test instrumentation.

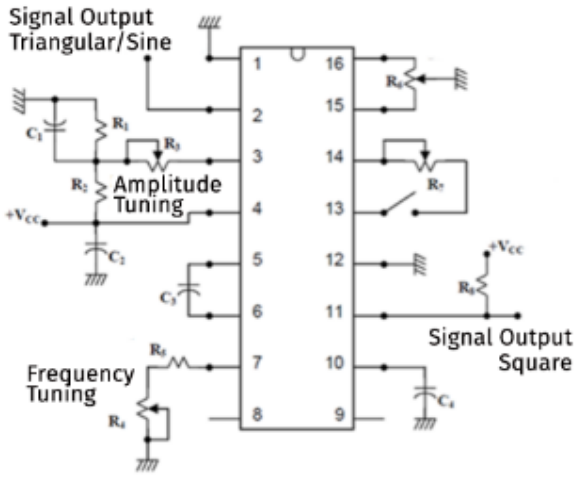

Figure 42: Specific configuration for the integrated function generator

The amplitude of the signal depends on the value of R_3 connected to pin 3. The datasheet reports a peak-to-peak amplitude of the output signal of 320mV for a resistance value of 1kΩ; thus the sensitivity of the output signal is:

$$S = \frac{320\ mV}{1k\Omega} = 3{,}2 \cdot 10^{-4}\frac{V}{\Omega}$$

So to obtain a peak-to-peak amplitude of 2V it would be assumed to use an R_3 with a theoretical value of 6.25kΩ:

$$R_3 = \frac{V_{OUT}}{S} = \frac{2V}{3{,}2 \cdot 10^{-4}\frac{V}{\Omega}} = 6{,}25 \cdot 10^4\Omega$$

It was experimentally determined that the real value of the R_3 had to be 5.6kΩ, because of additional parasitic resistance.

The frequency of the output signal is set through the external capacitance C_3, connected between the Pin 5 and 6, and the series of resistance R_4 and R_5:

$$F_{out} = \frac{1}{(R_4 + R_5) \cdot C_3}$$

According to the datasheet, the minimum value of the total impedance of the series of R_4 and R_5 must not be less than 1kΩ: it is useful to assign the resistance value of the minimum threshold to one of the two resistances (R_4 or R_5).

Thus to obtain the desired frequency of 10mHz, using a capacitance of 100μF:

$$R_4 + R_5 = \frac{1}{10^{-2}Hz \cdot 10^{-4}F} = 1M\Omega$$

In the realized prototype it was used a single resistance with the value of 1MΩ, but it could be also useful to insert a multiplexer connected to resistances with different values to test several frequencies.

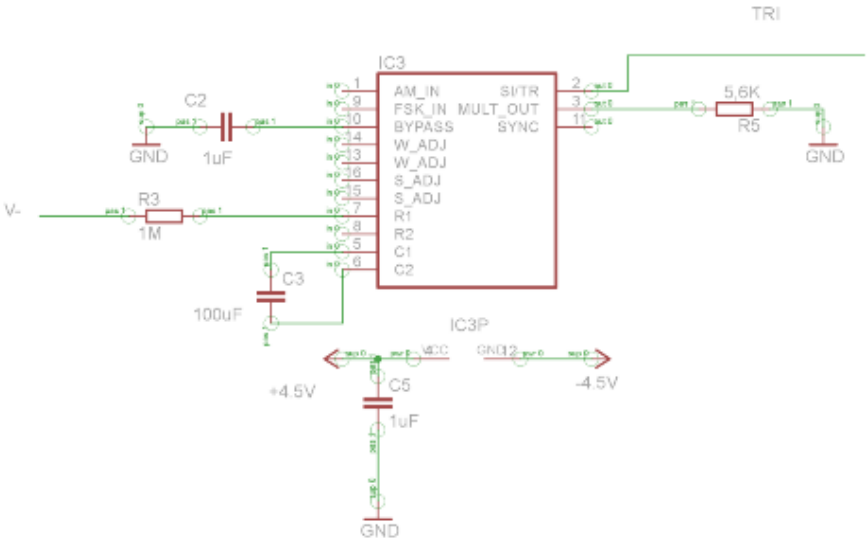

Figure 43: Schematic of the implemented XR-2206 function generator

An Arduino UNO evaluation board was used to replace the Digital Multimeter (Agilent 34410A): the Arduino UNO board is connected to a PC through an USB cable, so the data acquired by the microcontroller can be subsequently saved and analyzed using MATLAB.

Arduino is an open source electronics and firmware prototyping platform based on flexible software and hardware, that allows users to create microcontroller-based interfaces and devices able to sense and control physical systems using sensors and actuators.

The microcontroller on the board can be programmed using the Arduino Integrated Development Environment (IDE): it takes advantage of a C/C ++ library called *Wiring* : the availability of the library makes it much easier to implement the common input/output operations. This platform can be used to develop both stand-alone projects and tethered projects in communication with software running on a PC. The platform is suitable for prototyping with a modular approach and it's rapid spreading due to its ease of use and low cost.

Figure 44: Arduino UNO board

The Arduino UNO is one of the most popular evaluation board and is based on the ATmega328 microcontroller. It has 14 digital input/outputs (6 of them with PWM), 6 analog inputs, a 16 MHz crystal, a USB port, a power source, an ICSP connection, and a reset button.

Microcontroller	ATmega328
Operating voltage	5V
Input Voltage (recommended)	7-12V
Input Voltage (limit)	6-20V
Digital I/O Pins	14
PWM Digital I/O Pins	6
Analog Input Pins	6
DC Current per I/O Pins	40mA
Flash memory	32KB
Flash memory for Bootloader	0.5KB
SRAM	2KB
EEPROM	1KB
Clock Speed	16MHz

Table 6: Arduino UNO technical specifications

The Arduino Uno has an integrated Analog to Digital converter with 6 input pins and a resolution of 10bit. The internal ADC acquires values between 0 and 5V and returns a number between 0 and 1023 (2^{10}):

$$V_{LSB} = \frac{V_{MAX} - V_{MIN}}{1024} = \frac{(5-0)V}{1024} = 4.88\ mV$$

The output signal generated by the current in the electrochemical cell ranges range from negative to positive voltage values. Since the internal ADC of

ATmega328 is not able to read negative potentials it was necessary to design a circuit to adapt the signals and interface them with Arduino board.

So the output signal from the trans-impedance amplifier it's made totally positive adding a voltage offset to it: a summing amplifier was used to sum a positive constant voltage (3.3V) to the signal in order to make it completely positive. Furthermore after the summing stage, it was inserted a low-pass filter to remove some noise.

First tests were performed using the following configuration:

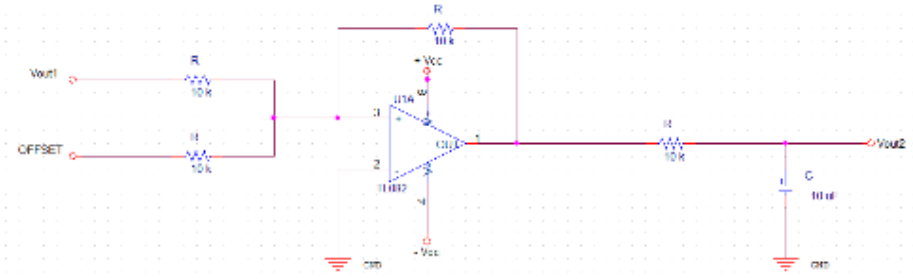

Figure 45: Schematic of the summing op-amp (TL082) and the LP filter

However, in the definitive implementation of the circuit, it was decided to use the instrumentation amplifier INA114P:

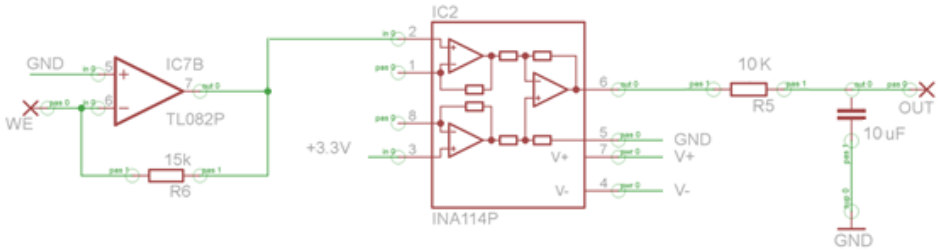

Figure 46: Signal adapter stage using an INA114P

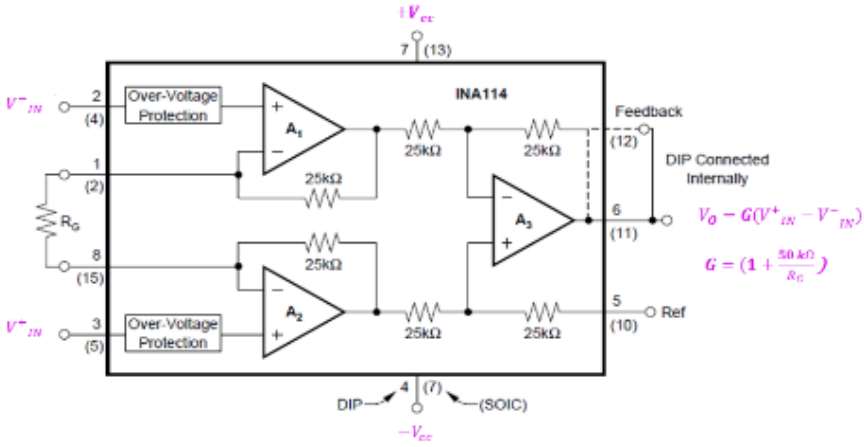

Figure 47: Schematic of the circuital configuration of the INA114. If the R_G is not connected the gain is zero.

The offset value of 3.3V is provided by Arduino UNO board to the V_{IN}^+ of the instrumentation amplifier. Thus a negative signal, up to a maximum -3.3V, will be shifted into a positive signal:

$$V_{OUT} = V_d = V_{IN}^+ - V_{IN}^-$$

$$V_{OUT} = V_d = 3.3V - V_{IN}^-$$

The signal coming from the potentiostatic circuit, ranging from a minimum value of about 10mV to a maximum value of about 1V, will go to the Pin 2 (V_{IN}^-) of the INA114P, it will be shifted positively of 3.3V and will be digitally converted by the ADC of the ATmega328 microcontroller. Also the triangular waveform, that drives the WE potential, will be adapted to be digitally acquired by the Arduino board in order to have control and synchronization data.

The block diagram shows the logical structure of the integrated device:

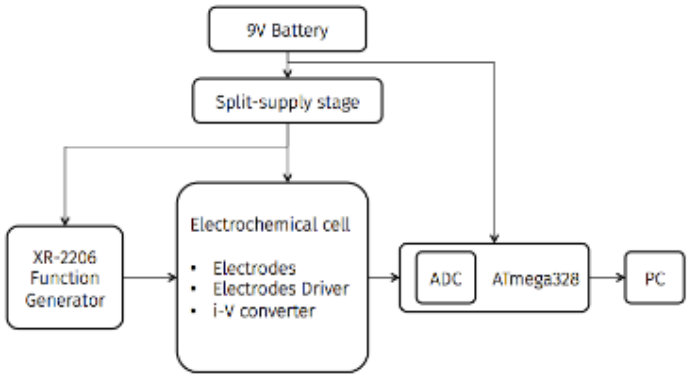

Figure 48: Scheme of the integrated e-tongue

Experimental tests were performed to evaluate the reproducibility of the output signal generated using the first laboratory experimental set-up or the new integrated device. Several water samples were analysed to match the output data, obtaining comparable results:

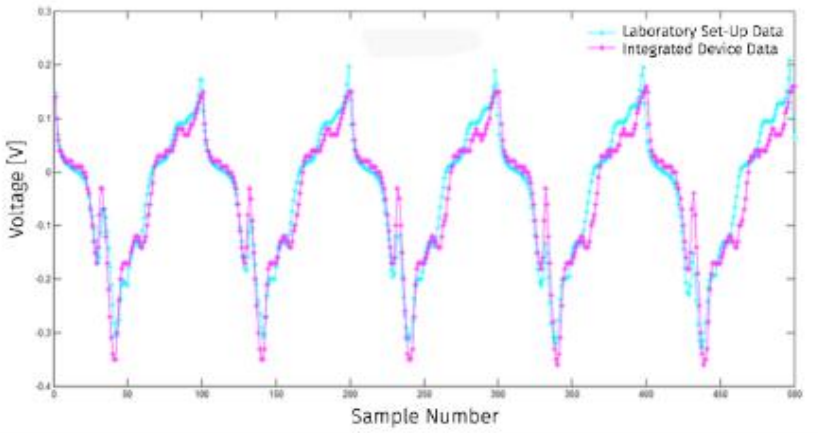

Figure 49: Output signal obtained analysis the same water sample using the two systems. The cyan curve is obtained from the output data of the laboratory set-up. The magenta curve is obtained from the output data of the integrated device. The input signals for both were: triangular wave ranging from -1 to +1 V and a scan rate of 40mV/s.

Comparing the score plots of the PCA performed on the output data of the two systems, the discriminatory performances remain unchanged:

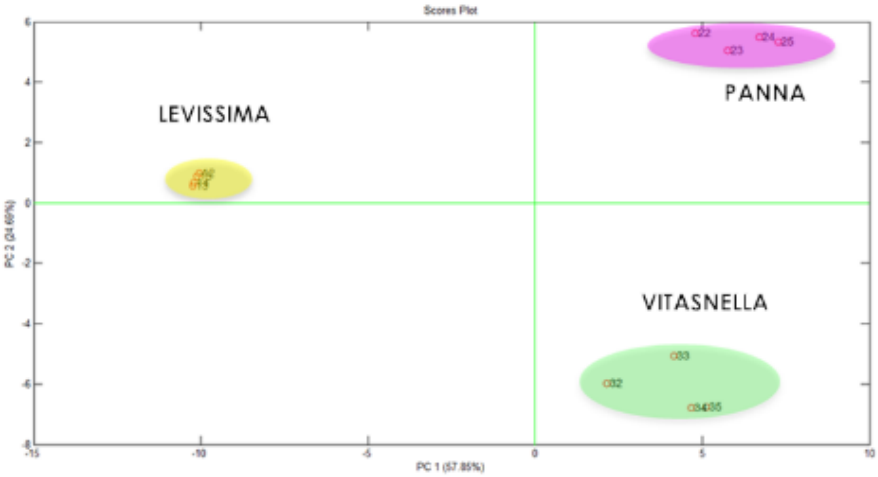

Figure 50: Score plot of the PCA of the data generated by the previous laboratory setup

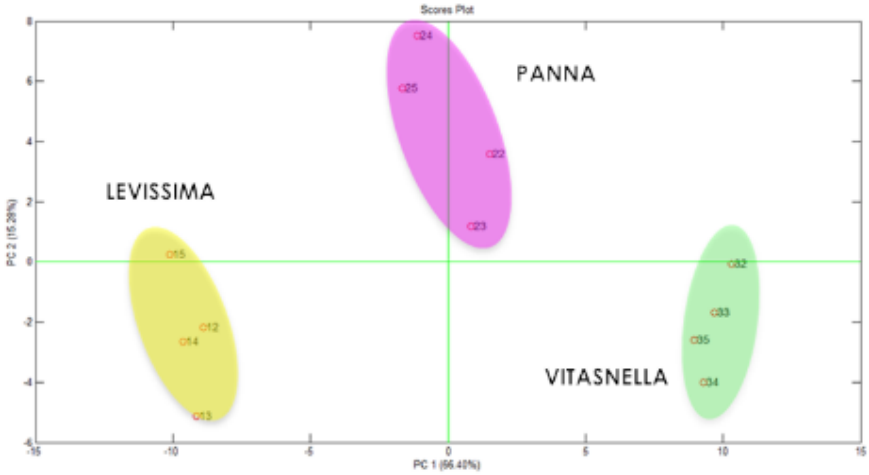

Figure 51: Score plot of the PCA of the data generated by the integrated device

Signal conditioning and Data Acquisition: third prototype

A successive device was realized to improve some critical features of the first second prototype:

- Function generator: the previous used XR-2206 generates very good analogue output waveform, but the signal is not so easy to customize and is not real-time tuneable. Some physical components have to be replaced when a waveform with different characteristic is needed.
- ADC resolution: the performance of the analogue to digital conversion stage has to be improved to maximize effectiveness of the electrochemical analysis.

The first step was to replace the function generator XR-2206 with a new electronic solution: it was decided to adopt a new microcontroller with an integrated DAC. The selected microcontroller is the Atmel AT91SAM3X8E that presents two DAC channels with 12-bits resolution (4096 levels), equal to 1.2mV. The Arduino Due is a microcontroller board based on the Atmel AT91SAM3X8E.

Microcontroller	AT91SAM3X8E
Operating Voltage	3.3V
Input Voltage (recommended)	7-12V
Input Voltage (limits)	6-16V
Digital I/O Pins	54 (of which 12 provide PWM output)
Analog Input Pins	12
Analog Output Pins	2 (DAC)
Total DC Output Current on all I/O lines	130 mA
DC Current for 3.3V Pin	800 mA
DC Current for 5V Pin	800 mA
Flash Memory	512 KB all available for the user applications
SRAM	96 KB (two banks: 64KB and 32KB)
Clock Speed	84 MHz

Table 7: Arduino DUE technical specifications

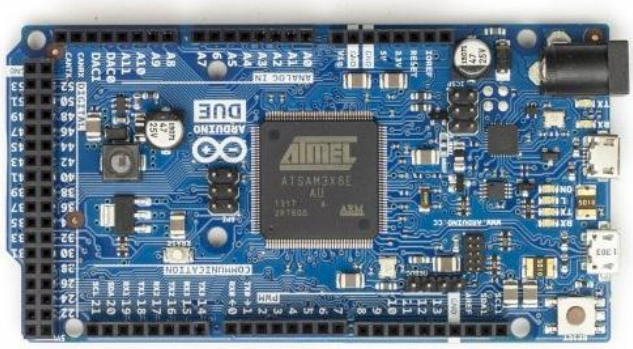

Figure 52: Arduino DUE board

Thus the input signal to the potentiostat circuit will be provided by the internal DAC of the AT91SAM3X8E. The microcontroller gets the analogue voltage values to reproduce from a custom look-up table where the discretized waveforms are stored. Four different waveforms were stored in the look-up table: sine, triangular, saw-tooth and square wave. Each waveform is discretized in 500 values, with a step resolution of 4mV. The values are expressed in discretization levels.

The waveforms were discretized in 500 values in order to have the possibility of changing the signals frequency in a useful range: too many values would have limited the maximum available frequency.

The analogue signal generated by the DAC has only positive values so it has to be adapted to cover also negative potentials: the DAC signal is shifted to negative values using an instrumentation amplifier INA114 and then it is applied to the WE in the electrochemical cell.

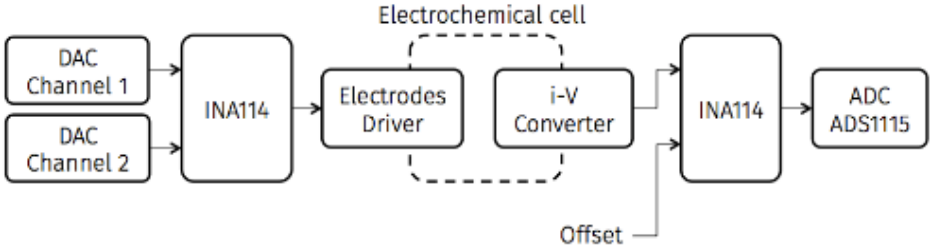

Figure 53: Scheme of the device

The DAC Channel 1 uses the lookup table to generate the analogue input waveform, totally positive: this signal goes on V_{IN}^{+} pin of the INA114. The DAC Channel 2 provides the offset on the V_{IN}^{-} of the INA114 to shift the signal. So after the adapting stage, the analogue signal generated by the DAC Channel 1 can range from negative to positive values (e.g. Triangular wave ranging from -1 to +1 V). The obtained signal is applied to the Working electrode through the driver amplifier. The current flowing on the WE, because of the running redox reactions, is converted into current by the trans-impedance amplifier (i-V converter). The voltage signal, ranging from negative to positive values, is adapted using another INA114 to be digitally converted by an external ADC.

The used ADC is not the internal one of the Atmel microcontroller, but is an external ADC, the Texas Instruments ADS1115.

The ADS1115 is low power 16-bits analogue to digital converter: it was selected to replace the internal ADC of the Arduino board because of its higher resolution. In fact the microcontroller used in the Arduino DUE board has a 12-bit ADC.

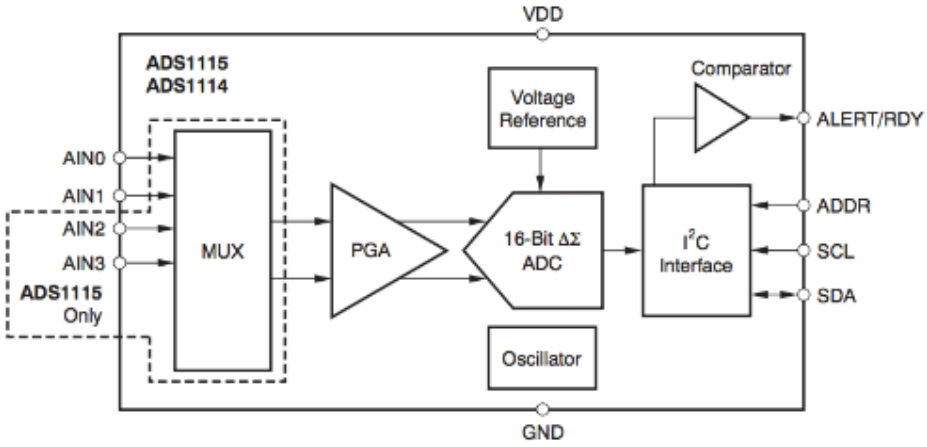

Figure 54: ADS1115 block diagram

The ADC1115 has 4 single inputs or 2 differential inputs. It has an internal pre-amplification stage (programmable gain amplifier, PGA) and it's based on a ΔΣ converter. The ADC1115 has an I²C interface fully compatible with the Atmel AT91SAM3X8E.

The ADS1115 is used in the differential configuration with a sample rate of 500 samples/cycle.

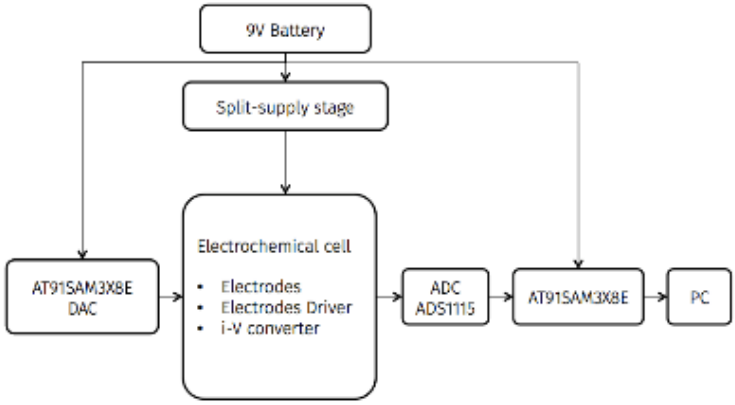

Figure 55: Scheme of the integrated e-tongue (third prototype)

This e-tongue device, based on the Arduino DUE board, optimized system performances as desired:

- The internal DAC module allows the complete customization of the input signals through the use of the lookup tables. The waveform and the frequency of the signal can be modified at software level without changing hardware components.

- The new ADC has an higher resolution of 0.1875mV versus 4.88 mV of the previous device.

PC Data Acquisition and GUI

A Graphical User Interfaces (GUI) was developed to control the e-tongue and visualize and save the output data on a PC. The GUI was developed in the MATLAB programming environment.

To run a measurement it's necessary to set some parameters to communicate with the e-tongue microcontroller and to choose the input signal for the cyclic voltammetric analysis.

Figure 56: Communication and control parameters

It's necessary to define the specific virtual serial port that the operating system is using to communicate with the e-tongue system.

The waveform of the input signal can be chosen among the four possible input waves (sine, triangular, saw-tooth, square). The amplitude of the input signal was fixed at 2V peak to peak, ranging from -1V to +1V.

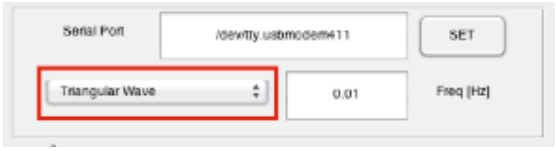

The frequency of the input signal can be set.

At the end of the measurement it's possible to save the output data into a .mat file.

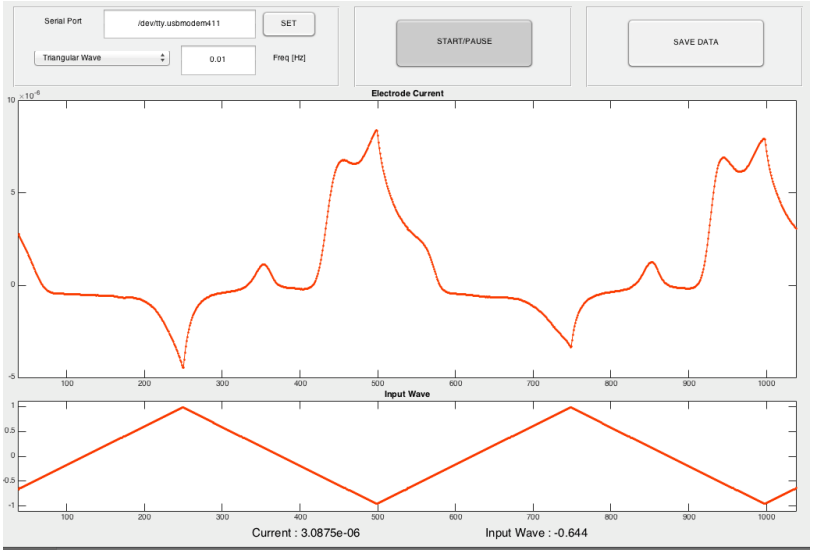

Figure 57: Cyclic voltammetric analysis of a water sample using a triangular wave with a frequency of 0.01Hz. The upper chart shows the system output current signal (A); the lower chart shows the input signal (V).

Development of a Novel E-nose System

Introduction: e-nose working principles

The electronic nose is an electronic sensory device based on an array of gas sensors. The gas sensors are able to provide an electrical signal, reacting with the chemical compounds of the gas sample under analysis. To obtain an electrical output signal, the sensors must be integrated into a proper signal transduction chain with a suitable electronic interface.

The hardware architecture of an E-nose system is significantly dependent on the specific application for which it is designed; however from a general point of view it is composed of a gas sampling and delivery system, a gas sensors array, a signal conditioning stage, a data acquisition and digitization system, a signal processing stage and a system able to implement suitable algorithms to perform classification or regression processes on the data.

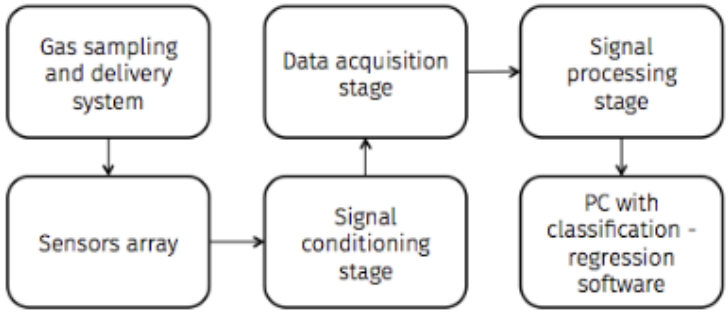

Figure 58: Block diagram for e-nose systems

As in the human olfactory system, in the electronic nose the interaction between the volatile chemical compounds and the sensors of the array produces, in a reversible way and in real-time, the change of an intrinsic quantity of the sensor properly transduced into an electrical signal that thereafter will be recorded and processed.

The developed e-nose system is based on an array of quartz crystal microbalances (QCM): QCMs take advantage of the piezoelectric properties of a quartz crystal; they are made of a thin plate of quartz crystal set in vibration by suitable electronic circuits, at a proper frequency.

Different quartz cutting directions produce structures with different sensitivities to volatile compounds: the quartzes used in the developed e-nose were cut along the AT crystallographic direction and then oscillating in shear thickness mode (along the thickness strain) at approximately 32MHz.

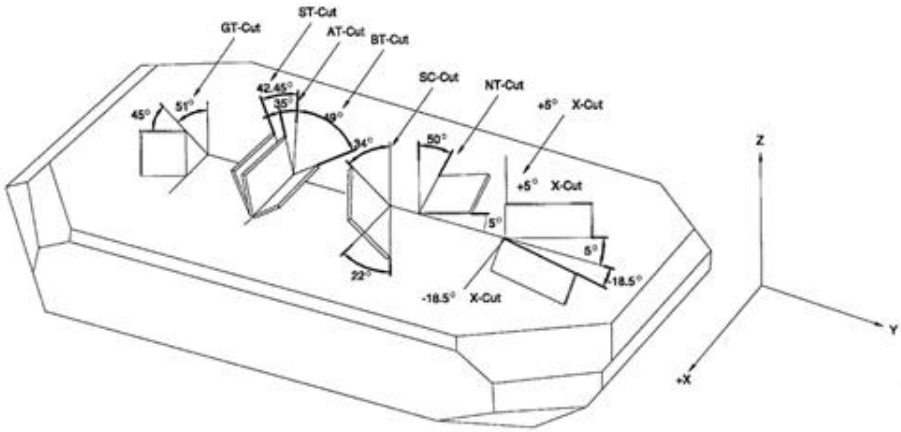

Cut Type	XY	NT	X Bar
Frequency Range	1-50 KHz	3-10 KHz	40-200 KHz
Vibration Mode	Bending 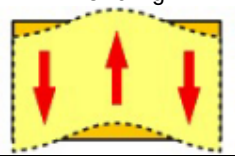		Extension 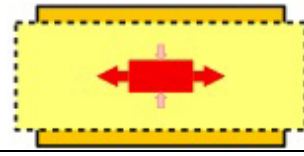

Cut Type	DT	SL	BT	AT
Frequency Range	100-300 KHZ	350-1100 KHz	3-22 MHz	0.8-40 MHz
Vibration Mode	Face Shear 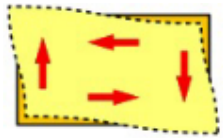		Thickness Shear 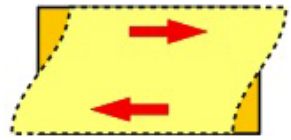	

Table 8: Cut types, frequency ranges and vibration modes of a quartz crystal

The transducing ability of the piezoelectric quartz crystals is due to the fact that if the mass weighing on the piezoelectric material changes, also the resonance frequency will change: the absorption of volatile molecules produces a mass variation and then a frequency shift.

In fact, thanks to the intrinsic piezoelectric properties, the quartz crystal behaves as a resonant electrical circuit whose resonance frequency is proportional, considering small perturbations, to the inertial mass of the crystal itself.

The quartz microbalances (QCMs) are inertial mass variations sensors. A mass change on the sensor surface produces a change in the frequency of the resonator. The quartz crystal microbalance, shown in Figure 9, is made of a quartz slice, used as a transducer, between two gold electrodes.

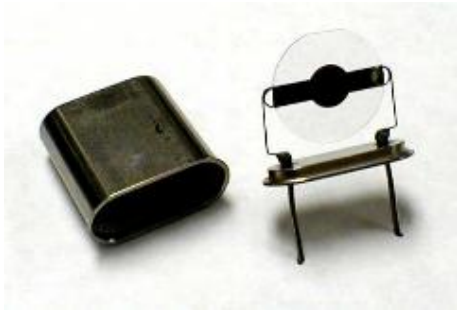

Figure 59: Picture of a quartz crystal microbalance (QCM)

The piezoelectric effect is a reversible process in that materials exhibiting the direct piezoelectric effect (the internal generation of electrical charge resulting from an applied mechanical force) also exhibit the reverse piezoelectric effect (the internal generation of a mechanical strain resulting from an applied electrical field).

Thus by applying an AC potential difference between the two faces of the crystal, the quartz will produce a vibration: the frequency of the vibration will be inversely proportional to its thickness.

The fundamental vibration frequency of the quartz, f_0 , is a function of the physical dimensions and the cutting angle of the quartz. The frequency of the commercially available quartzes ranges from hundreds of kHz to tens of MHz. This is mainly due to the fact that the frequency is inversely proportional to the thickness of the quartz: higher frequencies would require smaller thickness and the quartzes would be extremely fragile.

The electrical behaviour of a quartz crystal can be explained using the Butterworth-Van Dyke (BVD) model, with an equivalent electrical circuit:

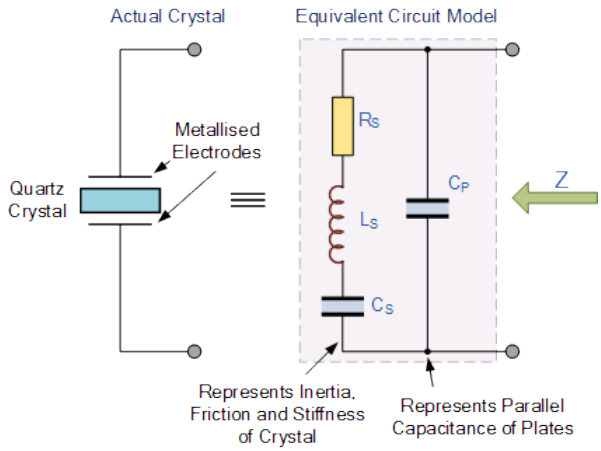

Figure 60: Butterworth-Van Dyke equivalent electrical circuit of a quartz crystal

Each electrical components of the equivalent circuit represents a physical quantity: the resistance R_1 represents the energy dissipation of the crystal; the capacitance C_1 is the energy stored into the crystal and is related to the mechanical elasticity of the crystal and of the surrounding materials; the inductance L_1 represents the inertial mass of the oscillator; the parasitic capacitance C_0 is the sum of the single capacitances due to the electrodes and the electrical connections.

The total impedance of the circuit is:

$$Z(s) = \left(\frac{1}{s \cdot C_1} + s \cdot L_1 + R_1\right) \parallel \left(\frac{1}{s \cdot C_0}\right)$$

$$Z(s) = \frac{s^2 + s\frac{R_1}{L_1} + \omega_s^2}{(s \cdot C_0)\left[s^2 + s\frac{R_1}{L_1} + \omega_p^2\right]}$$

$$\omega_s = \frac{1}{\sqrt{L_1 C_1}}$$

$$\omega_p = \sqrt{\frac{C_1 + C_0}{L_1 C_1 C_0}} = \omega_s \sqrt{1 + \frac{C_1}{C_0}} \approx \omega_s \left(1 + \frac{C_1}{2C_0}\right) \quad \text{if } (C_0 \gg C_1)$$

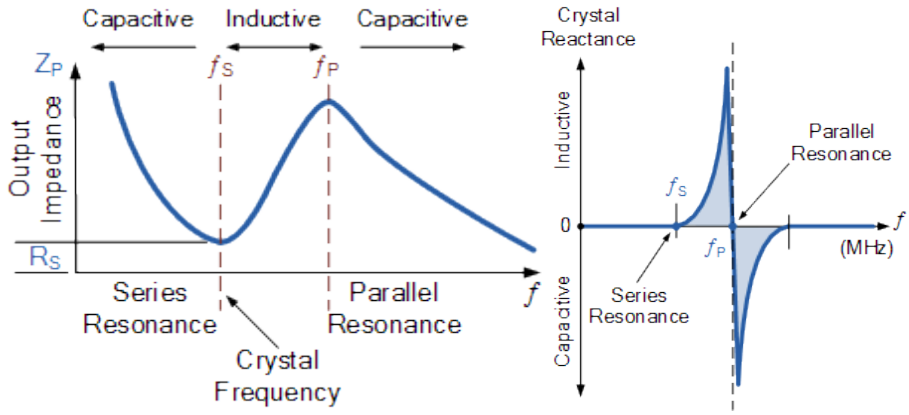

Figure 61: Impedance behaviour versus frequency

A quartz crystal has both a series and a parallel resonance: crystals oscillating up to 30 MHz generally work between the series and the parallel resonances, away from each other of a few kilohertz.

In order to provide sensing capabilities to the crystal quartz, it's necessary to cover its surface with a coating layer of adsorbent material, generally polymers or organic molecules films. The obtained system can be used to sense inertial mass variation: in fact it provides an electrical response proportional to the number of total adsorbed molecules.

So the total frequency variation when the QCM has adsorbed a certain number of volatile molecules is:

$$f = f_0 - Km_{coating} - Km_{adsorbed}$$

where:

f_0	is the fundamental resonance frequency of the clean crystal quartz
$Km_{coating}$	is the frequency shift due to the addition of the adsorbing layer
$Km_{adsorbed}$	is the frequency shift due to the addition of the adsorbed material

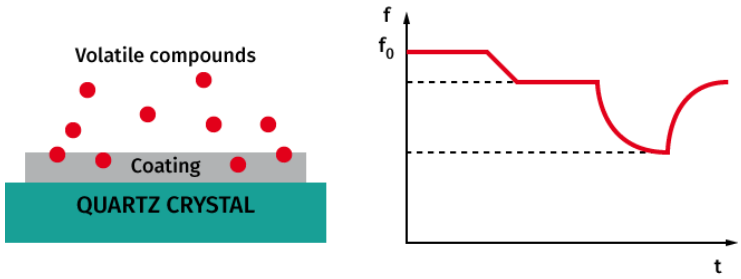

Figure 62: Curve of a typical QCM response

When the bonds established between the sensitive material and the adsorbed molecules are weak, it is possible to bring the sensor to the initial condition using a flow of inert gas, such as nitrogen or argon, at room temperature to remove the adsorbed molecules.

Sauerbrey, in 1959, was the first scientist who mathematically formalized the relationship between the inertial mass change, due to adsorption of the molecules, and the frequency variation [58]:

$$\Delta f = \frac{-2f_0^2 \Delta m}{A\sqrt{\mu_g \rho_q}}$$

Where:

Δf is the frequency variation (Hz)
Δm is the mass variation (g)
f_0 is the resonance frequency of the quartz crystal (Hz)
A is the acoustic active area of the quartz (Area between electrodes, cm^2)
μ_g is the shear modulus of quartz for AT-cut crystal (2.947×10^{11} g cm^{-1} s^{-2})
ρ_q is the quartz density (2.648 g cm^{-3})

Because the film is treated as an extension of thickness, Sauerbrey's equation only applies to systems in which the following three conditions are met: the deposited mass must be rigid, the deposited mass must be distributed evenly and the frequency change $\frac{\Delta f}{f_0} = \frac{f_0 - K m_{coating}}{f_0} < 0.02$.

The sensitivity of the quartz is affected by several parameters. In fact, the calculation of sensitivity must take into account mechanical, electrical and the experimental conditions:

$$\Delta f = \frac{\partial f}{\partial m}\Delta \mathrm{m} + \frac{\partial f}{\partial c}\Delta \mathrm{c} + \frac{\partial f}{\partial \varepsilon}\Delta \varepsilon + \frac{\partial f}{\partial \sigma}\Delta \sigma + \frac{\partial f}{\partial T}\Delta \mathrm{T} + \frac{\partial f}{\partial P}\Delta \mathrm{P} + \cdots$$

Where:

$\Delta \mathrm{m}$ is the mass variation
$\Delta \mathrm{c}$ is the coating variation
$\Delta \varepsilon$ is the relative permittivity variation
$\Delta \sigma$ is the conductivity variation
$\Delta \mathrm{T}$ is the temperature variation
$\Delta \mathrm{P}$ is the pressure variation

Therefore the sensitivity can be obtained as the frequency variation compared to all the parameters that affect it. Assuming that the mass variation is the only parameter that significantly affects the frequency variation, we can ignore all the other parameters

$$S = \frac{\Delta f}{\Delta m} = \frac{-2f_0^2}{A\sqrt{\mu_g \rho_q}} \left[\frac{Hz}{g}\right]$$

According to the Sauerbrey's law, the sensitivity, $\frac{\Delta f}{\Delta m}$, is directly proportional to the square of the resonance frequency of the quartz, then increasing the f_0, the sensitivity will greatly improve.

The amount of N adsorbed molecules, establishing chemical and physical reversible interactions with the surface the coating sensing material, depends on the concentration (partial pressure P) of the volatile molecules, on their affinity with the sensitive material (k) and on the temperature (T):

$$N = f(P, k, T)$$

Generally the temperature is assumed to be constant

The adsorption process is modelled through the formulation of certain assumptions, concerning the temperature and the surface of the adsorbent material resulting in the Langmuir's isotherm model that well describes simple systems close to the conditions of idealism [59].

The adsorption process according to the Langmuir's model is based on the following assumptions:

- The adsorbing surface is flat
- The number of adsorption sites is constant
- The adsorption process involves only the first layer of the molecules of the adsorbent material
- Adsorbed molecules have no mechanical energy when they impact with the adsorbent surface
- Each site can be occupied only by a single molecule
- Collisions with busy sites are elastic
- Desorption can only happen when sufficient energy is transferred from the molecular matrix underlying the surface
- Equilibrium is reached if the adsorption rate is equal to the desorption rate
- There are no interactions between adjacent sites

The Langmuir's model is a linear system of differential equations:

$$\begin{cases} \left(\frac{dn}{dt}\right)_{ads} = k_a \cdot P \cdot (N_s - n) \\ \left(\frac{dn}{dt}\right)_{des} = k_d \cdot n \end{cases}$$

where

N_s active sites (cm^{-2})
n occupied sites (cm^{-2})
k_a adsorption constant per site

k_d desorption constant per site

At the equilibrium:

$$k_a \cdot P \cdot (N_s - n) = k_d \cdot n$$

$$N = N_s \frac{K \cdot P}{1 + K \cdot P} \qquad K = \frac{k_a}{k_d}$$

$$\Theta = \frac{N}{N_s}$$

Where Θ is the fractional occupancy of the adsorption sites

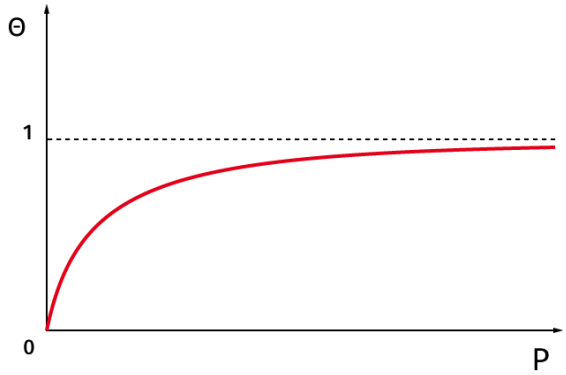

Figure 63: Evolution of **Θ** versus molecules concentration (P partial pressure)

E-nose system design and realization

A complex system, based on an array of quartz micro-balance sensors above described, has been designed and implemented to perform analysis on gas sample. The system consists of the following elements:

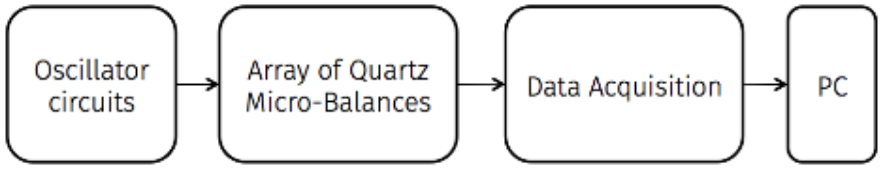

Figure 64: Block diagram of the e-nose system

The developed e-nose uses an array of 8 QCM with a resonance frequency of about 32MHz. Custom oscillator circuits were designed and realized to drive the QCMs. A data acquisition stage was developed to collect the frequency output of the QCMs array and visualize and store the data on a PC.

Oscillator circuits

An electronic oscillator is an electronic circuit that produces a periodic, oscillating electronic signal, generally an armonic wave or a square wave. They provide an output signal of desired amplitude and frequency, without the necessity of any input signal.

A generic oscillator circuit is made of two principal blocks: an amplification block and a positive feedback block.

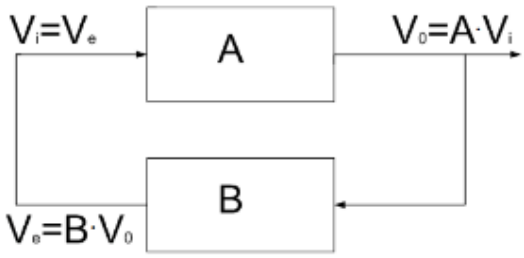

Figure 65: Block diagram of a generic oscillator circuit

The oscillation of the circuit is establish when:

$$V_0 = A(j\omega) \cdot V_i = A(j\omega) \cdot V_e = A(j\omega) \cdot B(j\omega) \cdot V_0$$

$$A(j\omega) \cdot B(j\omega) = 1$$

The latter condition, called Barkhausen's condition, shows that the signal must be neither amplified nor attenuated crossing the feedback loop. Also the total phase shift of the signal must be zero to ensure the presence of the positive feedback:

$$\begin{cases} |A(j\omega) \cdot B(j\omega)| = 1 \\ \phi\big(A(j\omega) \cdot B(j\omega)\big) = 0 \end{cases}$$

The Barkhausen's condition mathematically guarantees the presence of self-produced oscillations. In fact, on one hand if $|A(j\omega) \cdot B(j\omega)| > 1$ the system will saturate and on the other if $|A(j\omega) \cdot B(j\omega)| < 1$ the oscillations will lapse.

A real oscillator circuit is design to have a $|A(j\omega) \cdot B(j\omega)|$ slightly higher than one in order to ensure that the oscillations will start to occur. According to these initial conditions the system will start to oscillate, but the amplitude of the oscillations will start to increase. To avoid that the amplitude of the oscillations become too high, causing the distortion of the desired signal, a controller is needed to bring back $|A(j\omega) \cdot B(j\omega)|$ to the unitary value.

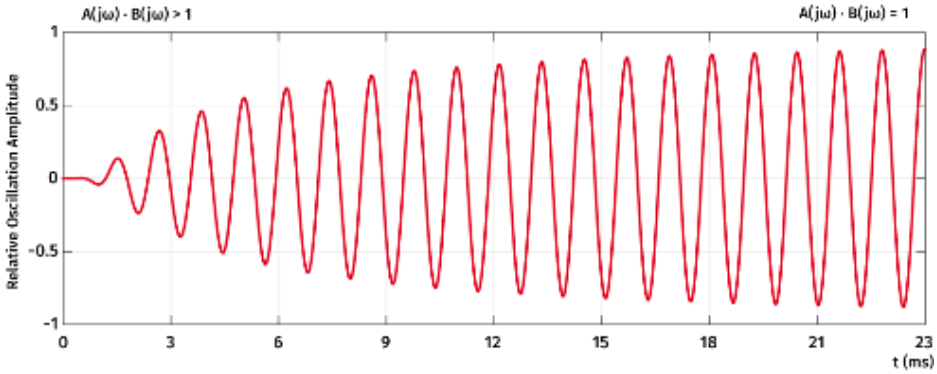

Figure 66: Behaviour of the oscillator circuit.

Oscillator circuits can be classified according to several parameters [60]:

- The waveform of the generated signal: the oscillator circuits are classified in sinusoidal oscillators, also called harmonic oscillators, and not sinusoidal, also called relaxation oscillators, which generate square, rectangular or saw-tooth waveforms with frequencies up to 20 MHz.
- The frequency of the generated signal: the oscillators can be classified into two categories based on the oscillation frequency. Low frequency oscillators, which generate signals with frequency not higher than 100kHz, and the high frequency oscillators, which generate signals with frequency higher than 100kHz.
- The electric elements used in the circuit: RC oscillators, LC oscillators and crystal oscillators. RC oscillators use resistor and capacitors in the feedback loop and generate low frequency signals. LC oscillators employ inductors and capacitors to adjust the oscillation frequency. Usually they are used to generate high-frequency signals. Quartz oscillators, employ a quartz crystal to simulate an RLC circuit: they guarantee the generation of a very stable signal with a frequency up to tens of MHz.

The oscillator circuits can be unstable, stable or asymptotically stable. An oscillator is unstable if its oscillations continuously increase, while an oscillator is asymptotically stable if the amplitude of the signal tends to zero. Finally, an oscillator is stable if the output signal has constant amplitude over time. The stability of an oscillator is affected by several parameters:

- The operating point
- The elements of the circuit may vary their characteristics because of temperature variations
- The power supply can affect directly the frequency,
- The external load can cause a variation of the quality factor
- The parasitic capacitances

Colpitts Oscillator

The Colpitts oscillator uses a capacitive voltage divider network as its feedback source. The two capacitors, C1 and C2 are placed across a single common inductor, L as shown. Then C1, C2 and L form the tuned tank circuit with the condition for oscillations being: XC1 + XC2 = XL.

The advantage of this type of capacitive circuit configuration is that with less self and mutual inductance within the tank circuit, frequency stability of the oscillator is improved along with a more simple design.

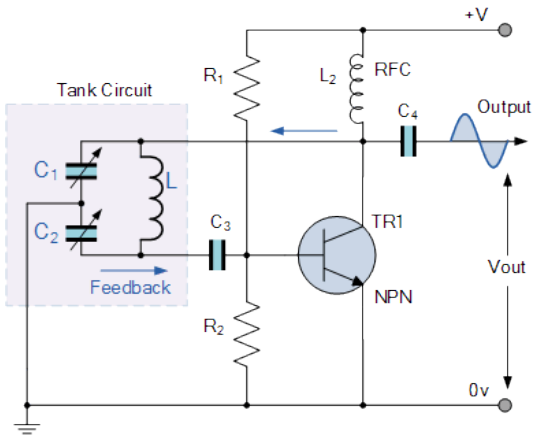

Figure 67: Basic Colpitts Oscillator Circuit

The frequency of the Colpitts oscillator circuit can be calculated by imposing:

$$\frac{1}{j\omega C_1} + \frac{1}{j\omega C_2} + L = 0$$

$$f_0 = \frac{1}{2\pi\sqrt{LC}} \qquad C = \frac{C_1 C_2}{C_1 + C_2}$$

This circuital configuration produces a total phase shift of 360°: the transistor causes a first phase shift of 180° of the input signal and the feedback circuit adds another phase shift of 180° because of the two capacitance and the inductance.

Replacing the LC circuit with a quartz crystal, it is possible to obtain a quartz oscillator circuit:

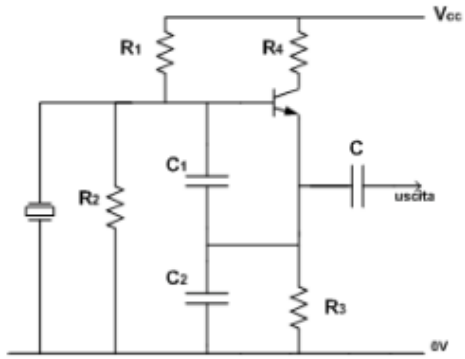

Figure 68: Quartz Colpitts Oscillator

The circuit shown fig. 70 uses a capacitances network (C_1 and C_2) as feedback loop. The output signal of the circuit can be collected on the transistor Emitter. The R_1 and R_2 resistor network sets the DC bias level on the Base while Emitter resistor R_3 sets the output voltage level. Resistor R_2 is set as large as possible to prevent loading to the parallel connected crystal. Capacitors C_1 and C_2 provide the feedback signal and are limited by the gain of the transistor. Resistor R_4 is necessary to properly drive the transistor.

The elements of the circuit must be suitably dimensioned according to the range of operating frequencies, as reported in Table 9.

	C_1 (pF)	C_2 (pF)	R_1 (kΩ)	R_2 (kΩ)	R_3 (kΩ)
1-3 MHz	220	330	33	33	6.8
3-6 MHz	150	220	33	33	6.8
6-10 MHz	150	220	33	33	4.7
10-20 MHZ	100	150	33	33	2.2

Table 9: Frequency range and elements values

Pierce Oscillator

The Pierce oscillator takes advantage of a TTL or CMOS inverter as active element: this oscillator can be realized using a odd number N of inverters in order to respect the Barkhausen's criterion.

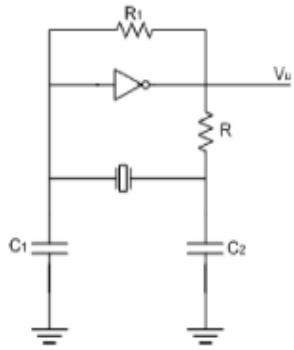

Figure 69: Pierce oscillator circuit

The output signal is collected on the inverter: resistance R_1 is used to keep the operating point in the linear region of the inverter that works as an amplifier. The quartz doesn't allow the passage of the DC signals, so without resistor R_1 it would not be possible to control the quartz. Thus the direct current will flow totally on R_1 to the output pin of the inverter. R_1 acts as a feedback resistor, biasing the inverter in its linear region of operation and effectively causing it to function as a high gain inverting amplifier. To see this, assume the inverter is ideal, with infinite input impedance and zero output impedance. The resistor forces the input and output voltages to be equal. Hence the inverter will neither be fully on nor fully off, but will operate in the transition region where it has gain.

The value of this resistance must be chosen considering the frequency of the oscillator circuit:

Frequency	R_1
32.8 kHz	10 - 15 MΩ
1 MHz	5 - 10 MΩ
10 MHz	1 - 5 MΩ
20 MHz	470 kΩ – 5 MΩ

Table 10: Frequency range and R1 values

Resistor R is necessary to limit the current flowing out from the output pin of the inverter and its value is never higher than 40-100kΩ and depends on the oscillation frequency. Capacitors C_1 and C_2 allow the oscillation of the circuit, but the oscillation occurs if the crystal quartz acts as an inductor between the series and parallel resonance frequencies. Usually C_1 and C_2 values are in the order of tens of pF [61].

In order to increase the stability of the system and the amplitude of the oscillations it's possible to realize a Pierce oscillator circuit using three inverters:

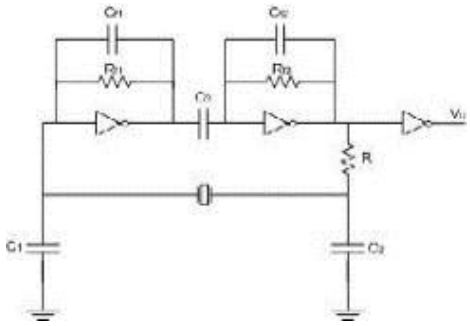

Figure 70: Three inverters Pierce oscillator

Capacitors C_{f1} e C_{f2}, in parallel with resistors R_{f1} and R_{f2}, stabilize the saturation of the first and second inverters. Capacitor C_3 decouples the two amplification stages of the inverters. The output signal can be collected on the output pin of the third inverter.

Simulation model of the crystal quartz

Several simulation tests were performed in the SPICE simulation environment NI Multisim 13.0 (National Instruments, USA) in order to design a quartz oscillator circuit with a operating frequency of 30 MHz: the Colpitts and the Pierce configurations were simulated.

The 30MHz quartz crystal was implemented in the simulation environment using the Butterworth-Van Dyke model. Thus the quartz crystal can be modelled as a RLC circuit with the circuital elements C_1, R_1, L_1, and C_0. The values of the model elements can be extracted from the technical datasheet of the HC49/4HSMX, a real 30MHz quartz crystal made by IQD Frequency Products Inc. [62].

HC49/4HSMX parameters	
Frequency	3.2 to 100.0 MHz
Frequency Tolerance	±10.00ppm to ±100.00ppm
Tolerance Condition	@ 25°C ±2°C
Frequency Stability	±15.00ppm to ±500.00ppm
Shunt Capacitance (C0)	7pF max
Equivalent Series Resistance	40Ω @ 8.0 – 40.0MHz

The values of C_1 and L_1 are not present in the datasheet, but they can be estimated:

$$f_0 = 30\ MHz = \frac{1}{2\pi\sqrt{C_1 L_1}}$$

Considering that C_1 takes values lower than C_0, it was decided to set the value of C_0 at 1.9fF. Thus the inductor L_1 will have a value of 14mH.

The quality factor of the quartz crystal oscillating at 30 MHz is:

$$Q = \frac{2\pi f_0 L_1}{R_1} = 69743.3$$

Simulation of Colpitts oscillator

The Colpitts oscillator circuit was simulated in the SPICE simulation environment NI Multisim 13.0 (National Instruments, USA). The simulated circuit is shown in Fig 71:

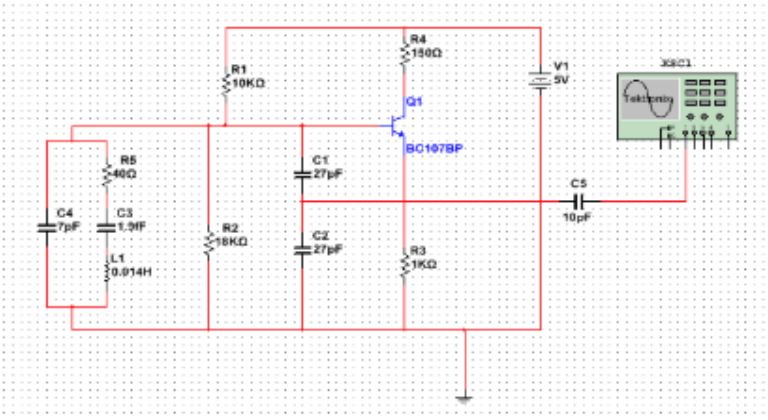

Figure 71: Colpitts oscillator circuit

The real quartz crystal was modelled with an equivalent circuit using the electrical parameters previously estimated. The transistor used is the BC107BP.

The results of the transient analysis of the circuit behaviour is shown in Fig. 72

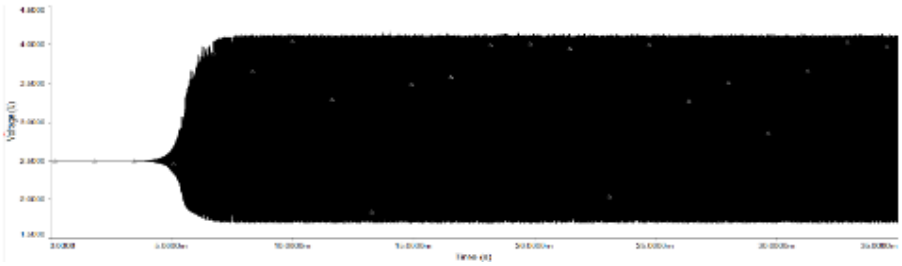

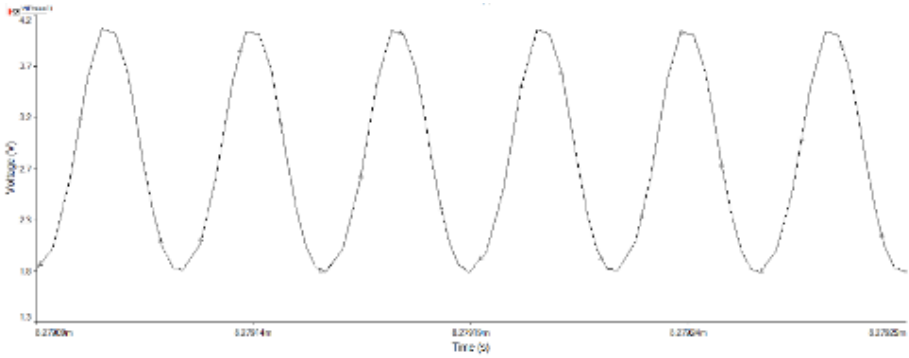

Figure 72: Transient analysis results

The evolution over time of the circuit oscillations shows the typical behaviour of a asymptotic stable oscillator: in fact, the amplitude of the oscillations increases and becomes constant when the system reaches the steady state, satisfying the Barkhausen's criterion.

It's possible to measure the frequency of the oscillation in the steady state: the period of the output signal is 33,3ns and so the oscillation frequency is about 30MHz.

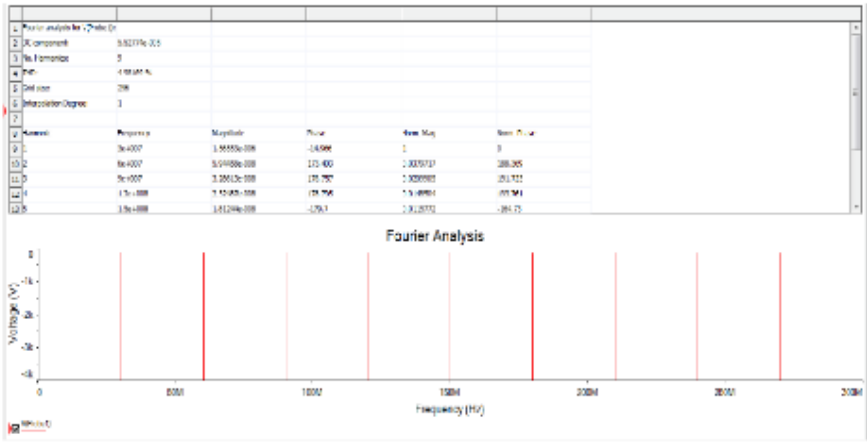

Figure 73: FFT analysis

FFT analysis results show the harmonic peaks of the oscillator circuit. Fundamental harmonic is situated at 30Mhz and the overtone harmonics are at 60, 90, 120, 150, 180, 210, 240, 290MHz.

Simulation of Pierce oscillator

The Pierce oscillator circuit was simulated in the SPICE simulation environment NI Multisim 13.0 (National Instruments, USA). The simulated circuit is shown in Fig 74:

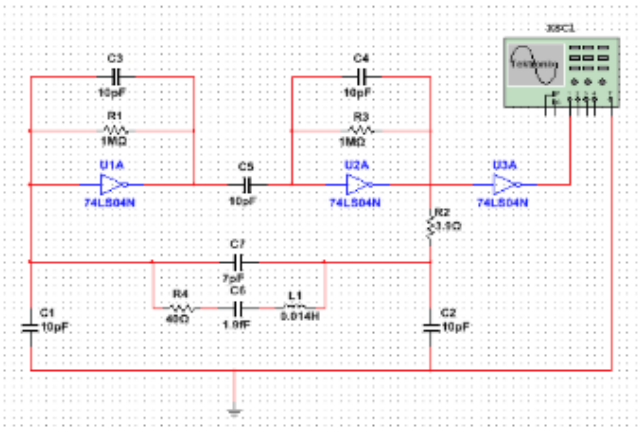

Figure 74: Pierce oscillator circuit

The quartz crystal was modelled with its equivalent circuit and the inverter used is the SN74LS04N. The values of C_1 and C_2 were calculated according to the parasite capacitor C_S, produced by the metal connections, and the load capacitor C_L. Usually the parasite capacitor has a value of 10pF. The value of the capacitor C_L can be extracted from the datasheet of the HC49/4HSMX crystal quartz: the value is 15pF.

Thus it's possible to calculate the value of C_1 and C_2:

$$C_L - C_S = \frac{C_1 C_2}{C_1 + C_2}$$

$$C_1 = C_2 = 10pF$$

The value of the resistor R_2 can be calculated examining the voltage divider composed of the resistor R_2 and the capacitor C_2:

$$R_2 = \frac{1}{2\pi f_0 C_2} = 530.51\Omega$$

The first simulations showed that R_2 value is too high to let the circuit oscillate. The proper value for the resistor R_2 should not be higher than 4Ω: using a R_2 of 3.9Ω it's possible to obtain the asymptotic stable behaviour of the oscillator circuit.

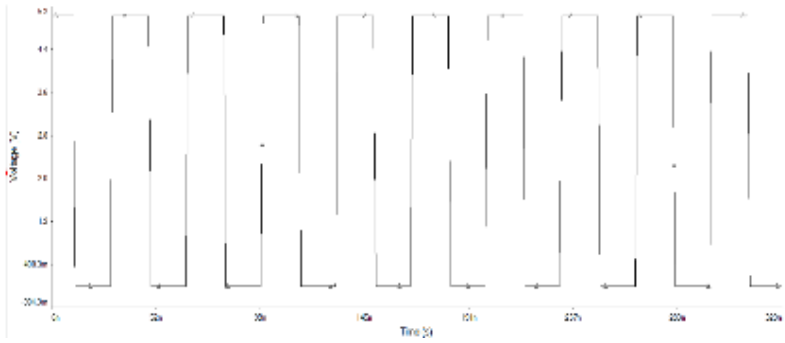

Figure 75: Output signal of the simulated Pierce oscillator

Analysing the output signal, it's possible to extract the period of the oscillation that is equal to about 33,3ns. So the frequency of the signal is about 30MHz.

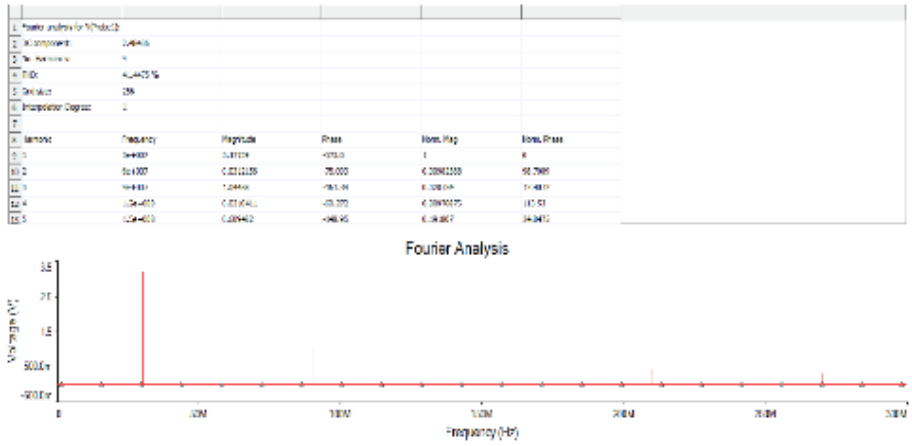

Figure 76: FFT analysis

FFT analysis results show the harmonic peaks of the oscillator circuit. Fundamental harmonic is situated at 30Mhz and the overtone harmonics are at 60, 90, 120, 150, 180, 210, 240, 290MHz. Overtone harmonics have a decreasing amplitude because the circuit produce a square waveform as output signal.

PCB design and realization

The layout of the two simulated oscillators was designed using EAGLE 7.1.0 (Easily Applicable Graphical Layout Editor, Cadsoft Computer GmbH). The QCMs and the other electric elements were properly placed in order to allow the future housing of the sensors into a measuring chamber. Each PCB contains 8 oscillator modules to drive totally 8 QCMs. The designed PCBs have two signal layers. All the elements belong to the through-hole category.

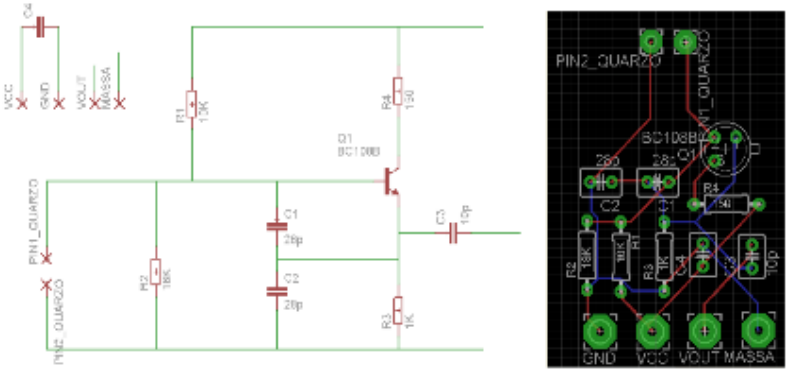

Figure 77: Design of the Colpitts oscillator: schematic of the PCB (left), layout of the PCB (right)

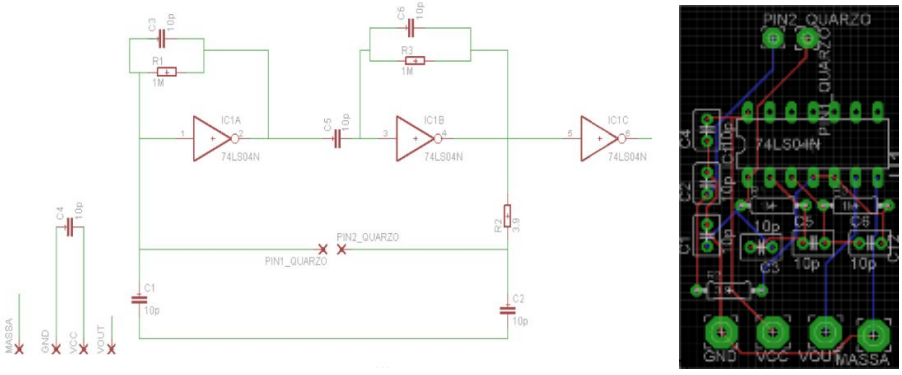

Figure 78: Design of the Pierce oscillator: schematic of the PCB (left), layout of the PCB (right)

The PCBs were fabricated by OSH Park LLC, a community PCB service based in USA (www.oshpark.com).

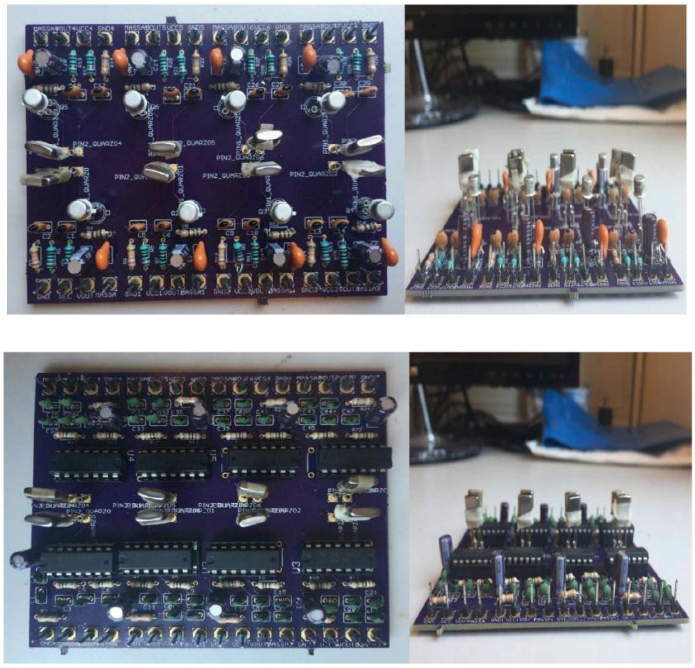

Figure 79: Manufactured PCBs: Colpitts (left) and Pierce oscillator (right)

PCBs test

The oscillator modules were supplied using Laboratory DC Power Supplies. The output signal was acquired using a digital oscilloscope, the Teledyne LeCroy HDO6054-MS: both the shape and the frequency of the output signal were analysed. The used QCMs are custom fabricated with a working frequency of about 32MHz.

Tests of Colpitts oscillator

The output signals generated by the 8 Colpitts oscillators modules are shown in Figures 80-87:

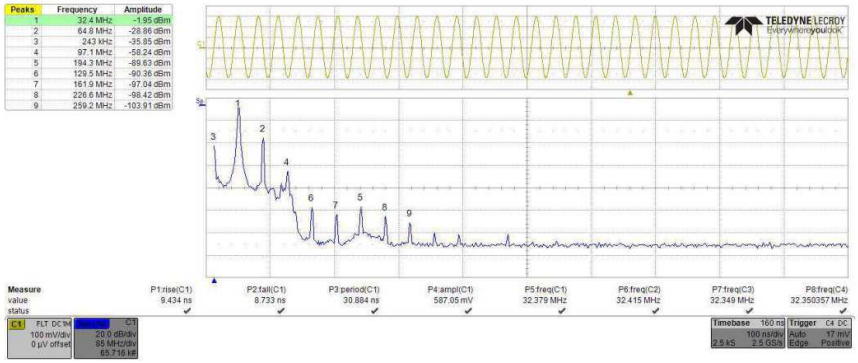

Figure 80: Output signal of the first Colpitts oscillator module. Each PCB contains 8 oscillator modules to drive totally 8 QCMs.

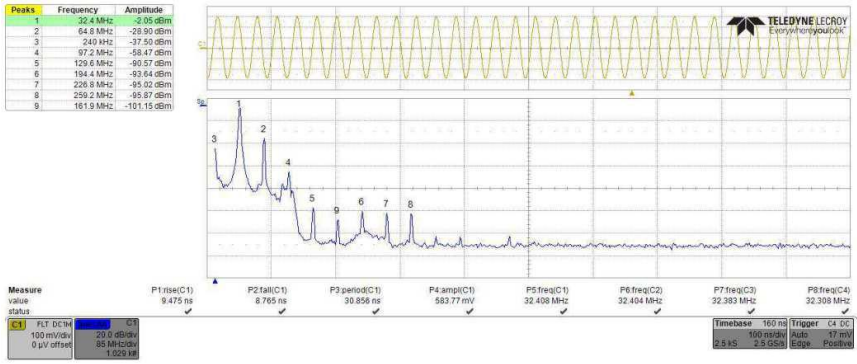

Figure 81: Output signal of the second Colpitts oscillator module. Each PCB contains 8 oscillator modules to drive totally 8 QCMs.

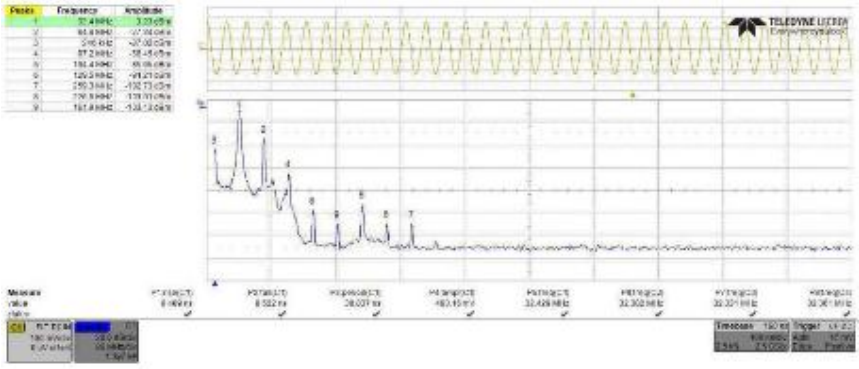

Figure 82: Output signal of the third Colpitts oscillator module. Each PCB contains 8 oscillator modules to drive totally 8 QCMs.

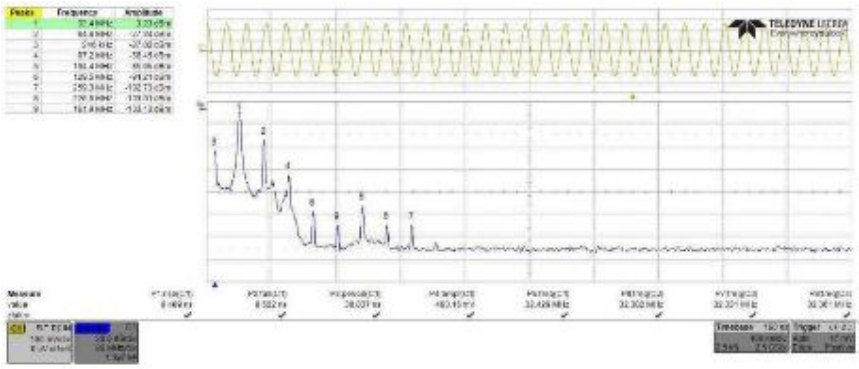

Figure 83: Output signal of the fourth Colpitts oscillator module. Each PCB contains 8 oscillator modules to drive totally 8 QCMs.

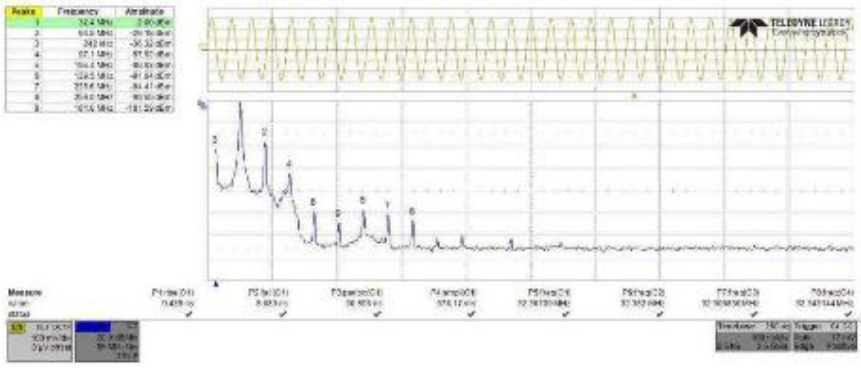

Figure 84: Output signal of the fifth Colpitts oscillator module. Each PCB contains 8 oscillator modules to drive totally 8 QCMs.

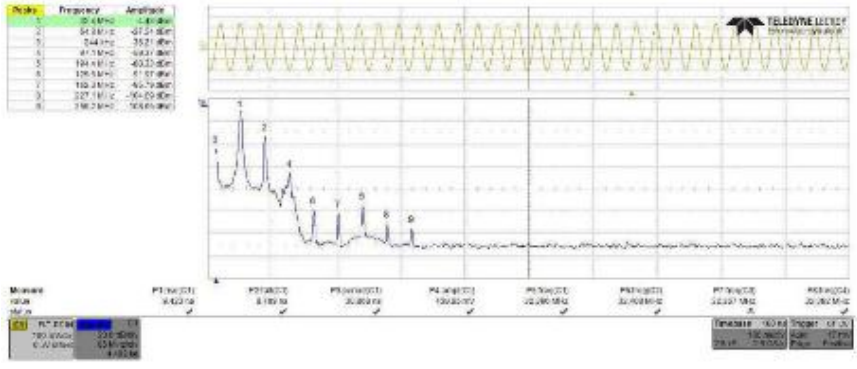

Figure 85: Output signal of the sixth Colpitts oscillator module. Each PCB contains 8 oscillator modules to drive totally 8 QCMs.

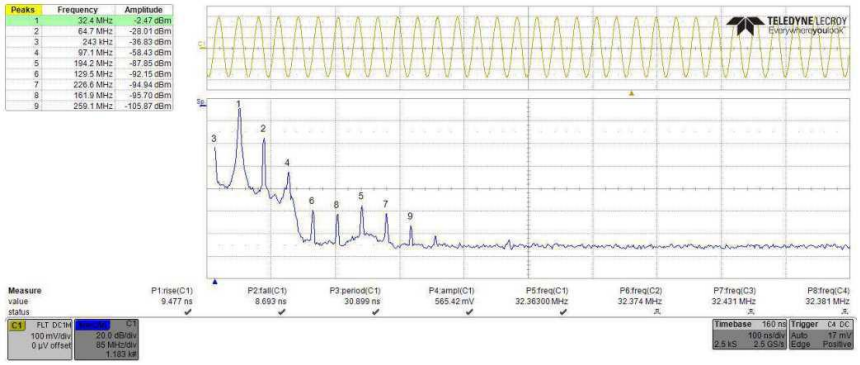

Figure 86: Output signal of the seventh Colpitts oscillator module. Each PCB contains 8 oscillator modules to drive totally 8 QCMs.

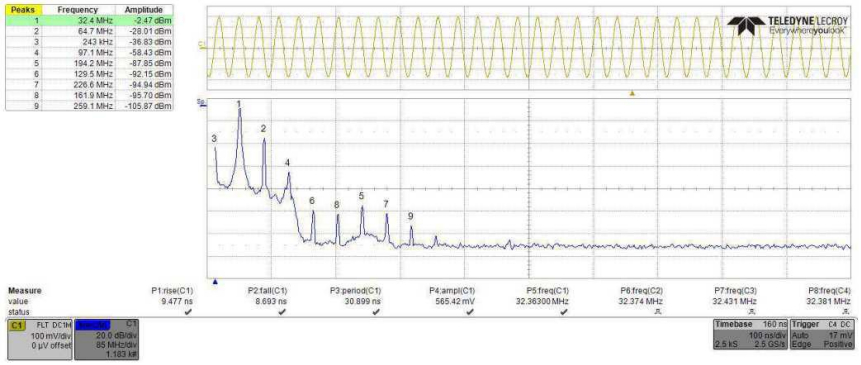

Figure 87: Output signal of the eighth Colpitts oscillator module. Each PCB contains 8 oscillator modules to drive totally 8 QCMs.

The frequency of the 8 oscillator modules is of about 32MHz, which matches the resonance frequency of the crystal quartz. Observing the FFT analysis, below each signal chart, it is possible to notice that the fundamental harmonic is located at 32MHz and that overtone harmonics are located at frequency values that are multiple of the fundamental.

The waveform of the signals is sinusoidal, as expected from the simulations. So that the oscillation occurs, the circuit must be supplied with a minimum voltage of 2.5V. The maximum possible voltage is the maximum voltage allowed by the used transistors (BC107BP).

At this stage it was possible to define the design specifications of a squaring circuit that is necessary for the successive steps of the measuring chain: in fact the output signal generated by the Colpitts oscillator must be squared to be read in the data acquisition stage, performed by a microcontroller.

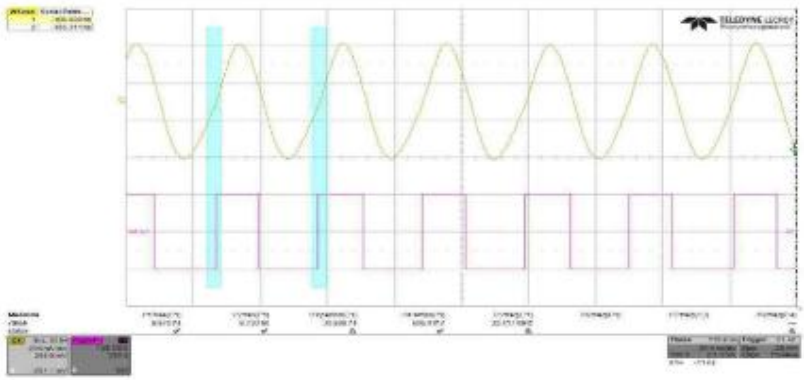

Figure 88: Squared output signal

The design specifications of the squaring circuit, obtained from the analysis of Fig 88, are reported in table 11:

Frequency	Rise time	Fall time	Amplitude
≈ 32.4MHz	≈ 9.4ns	≈ 8.6ns	≈ 545.2mV

Table 11: Parameters for the design of the squaring circuit

Tests of Pierce oscillator

The output signals generated by the Pierce oscillators modules are shown in Figures 89-96:

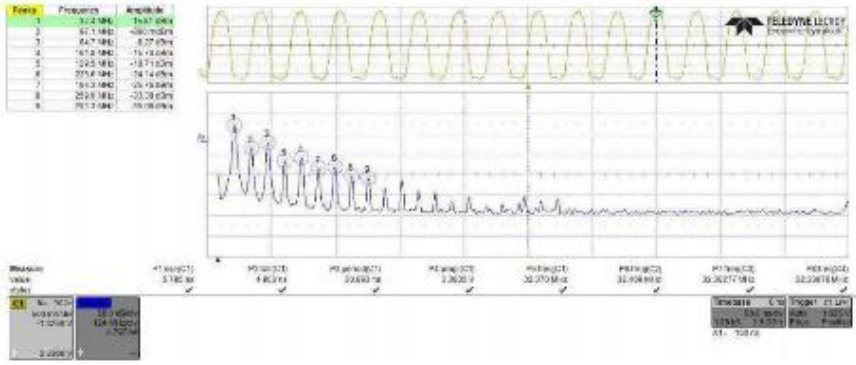

Figure 89: Output signal of the first Pierce oscillator module. Each PCB contains 8 oscillator modules to drive totally 8 QCMs.

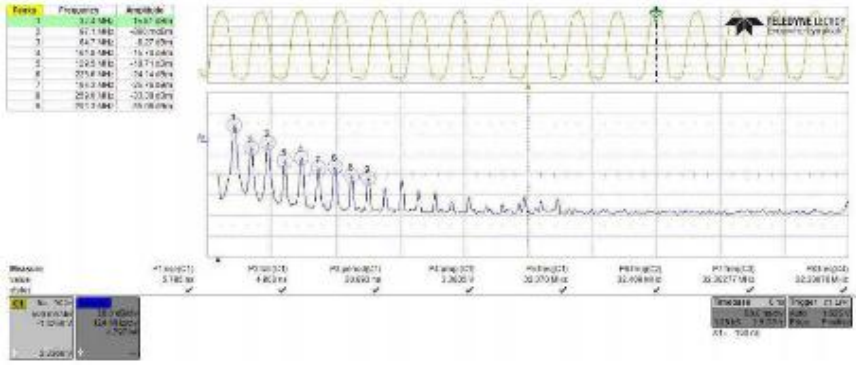

Figure 90: Output signal of the second Pierce oscillator module. Each PCB contains 8 oscillator modules to drive totally 8 QCMs.

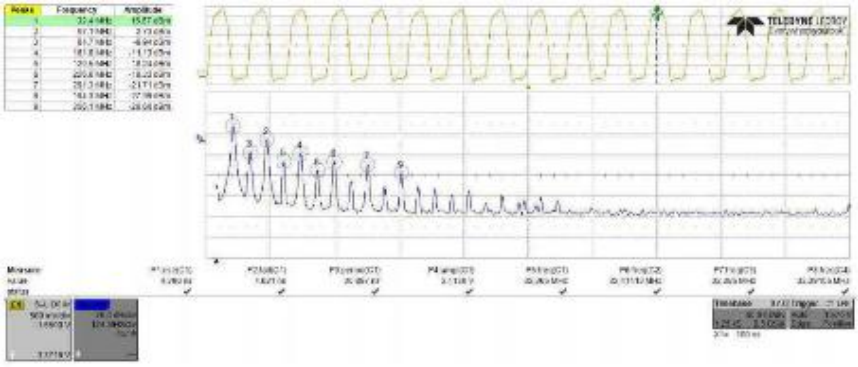

Figure 91: Output signal of the third Pierce oscillator module. Each PCB contains 8 oscillator modules to drive totally 8 QCMs.

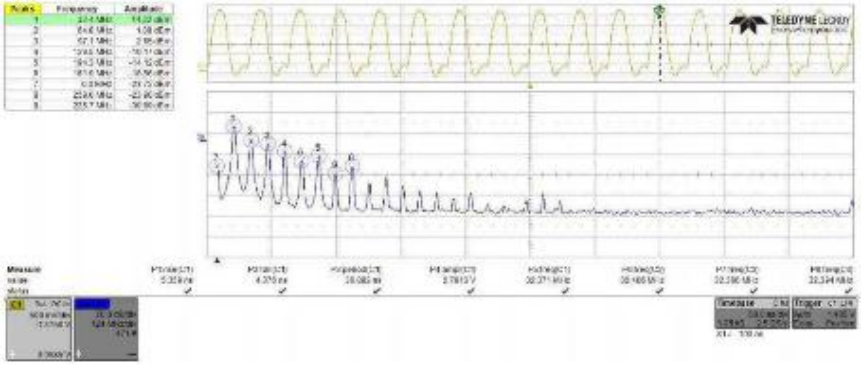

Figure 92: Output signal of the fourth Pierce oscillator module. Each PCB contains 8 oscillator modules to drive totally 8 QCMs.

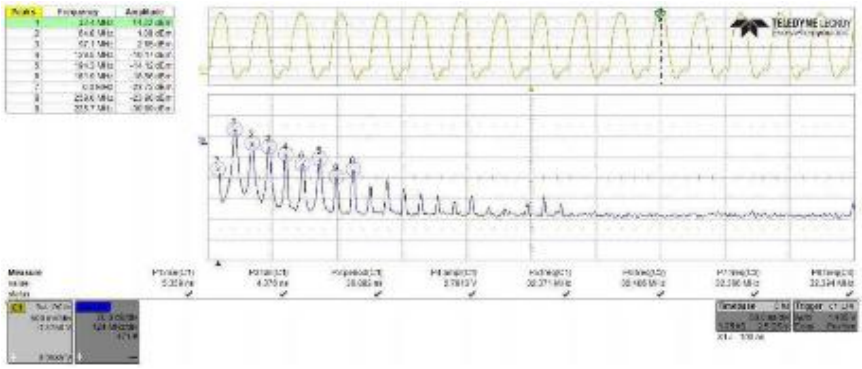

Figure 93: Output signal of the fifth Pierce oscillator module. Each PCB contains 8 oscillator modules to drive totally 8 QCMs.

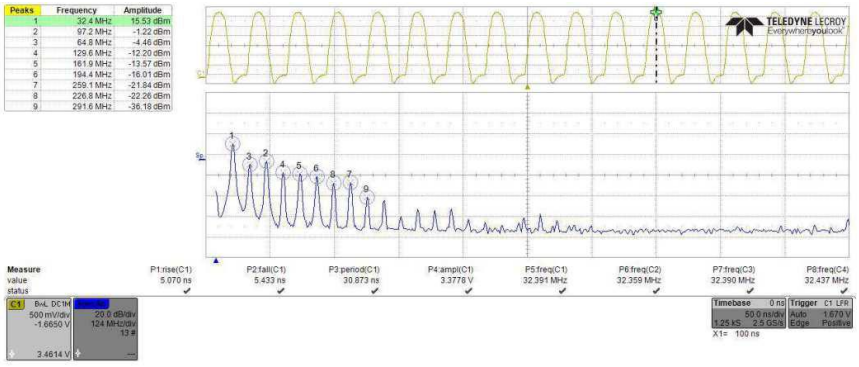

Figure 94: Output signal of the sixth Pierce oscillator module. Each PCB contains 8 oscillator modules to drive totally 8 QCMs.

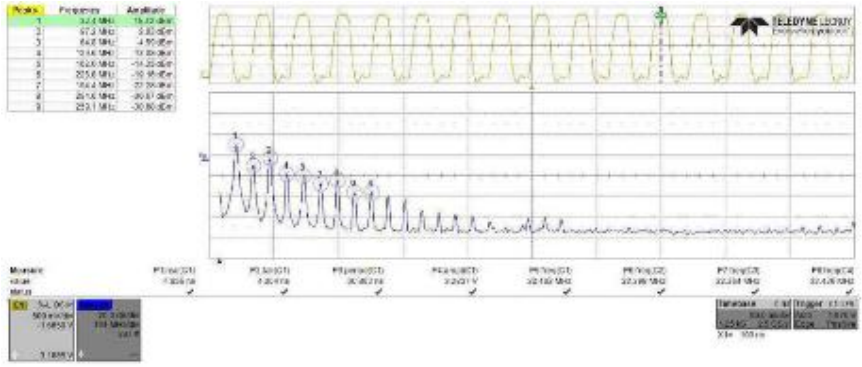

Figure 95: Output signal of the seventh Pierce oscillator module. Each PCB contains 8 oscillator modules to drive totally 8 QCMs.

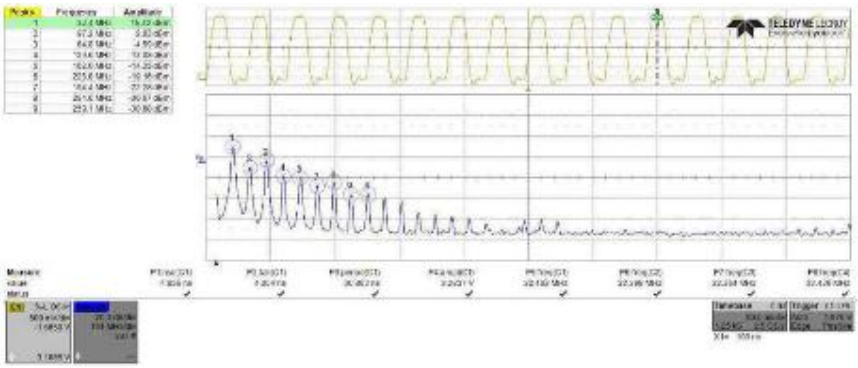

Figure 96: Output signal of the eighth Pierce oscillator module. Each PCB contains 8 oscillator modules to drive totally 8 QCMs.

The frequency of the 8 oscillator modules is of about 32MHz, which matches the resonance frequency of the crystal quartz. Observing the FFT analysis, below each signal chart, it is possible to notice that the fundamental harmonic is located at 32MHz and that overtone harmonics are located at frequency values that are multiple of the fundamental.

The stability of voltage supply is a critical parameter for the Pierce oscillator: the oscillation occurs only if the voltage supply is 3.00V. The circuit is not affected by cross-talk issues and each module oscillates independently.

At this stage it was possible to define the design specifications of a squaring circuit that is necessary for the successive steps of the measuring chain: in fact the output signal generated by the Pierce oscillator must be squared to be read in the data acquisition stage, performed by a microcontroller.

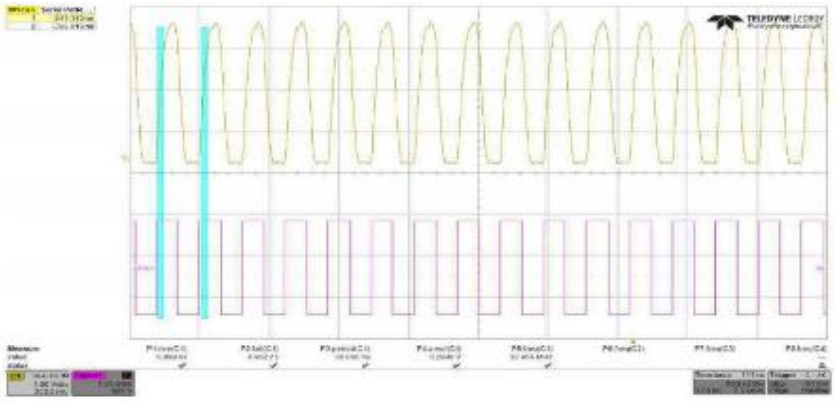

Figure 97: Squared output signal

The design specifications of the squaring circuit, obtained from the analysis of Fig. 97, are reported in table 12:

Frequency	Rise time	Fall time	Amplitude

≈ 32.4MHz	≈ 5ns	≈ 4.5ns	≈ 3.2V

Table 12: Parameters for the design of the squaring circuit

Signal conditioning and acquisition

The output signal generated by the Colpitts and Pierce oscillators must be squared to be compatible with the data acquisition stage.

The squaring stage takes advantage of the Texas Instrument comparator TLV3501 that is compatible with both CMOS and TTL logics. The TLV3501 feature a fast 4.5-ns propagation delay and operation from 2.7 V to 5.5 V. The maximum commutation frequency is 80MHz with a rise/fall time of 1.5ns that is perfectly compatible with the design specifications previously set (Tables 11 and 12).

TLV3501 Sepcifications	
V_S Supply Voltage	2.2 – 5.5V
T_{pd} Propagation delay time	4.5 ns
T_R Rise time	1.5 ns
T_F Fall time	1.5 ns
f_{MAX} Maximum toggle frequency	80 MHz

Table 13: TLC3501 Specifications

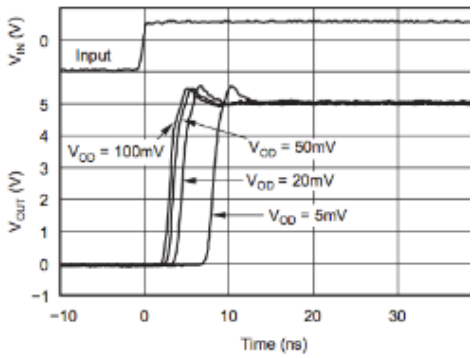

Figure 98: Output Response for Various Overdrive Voltages (Rising)

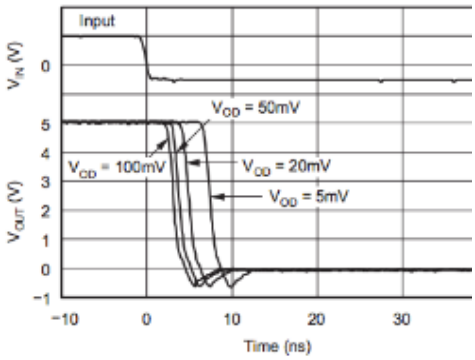

Figure 99: Output Response for Various Overdrive Voltages (Falling)

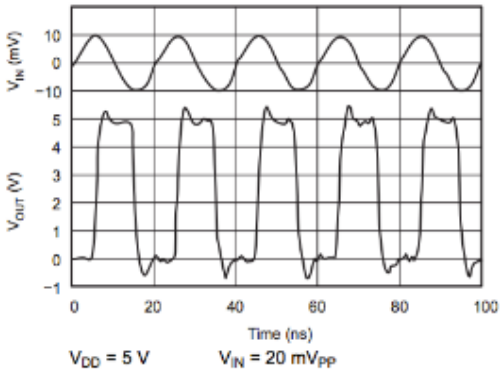

Figure 100: Response to 50-MHz Sine Wave

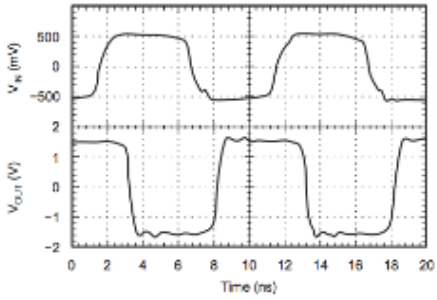

Figure 101: Response to 100-MHz Sine Wave (±2.5-V Dual Supply into 50-Ω Oscilloscope Input)

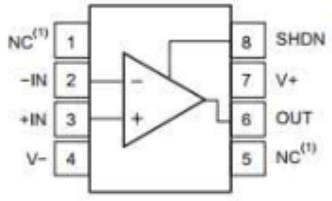

Table 14: Package layout of TLV3501

PIN		Description
- IN	2	Negative Input (Inverting)
+ IN	3	Positive Input (Non inverting)
NC	1 , 5	Not connected
OUT	6	Output signal

SHDN	8	Shutdown (the device is off when the pin is HIGH)
V-	4	Negative Voltage Supply
V+	7	Positive Voltage Supply

Table 15: Pin layout of TLV3501

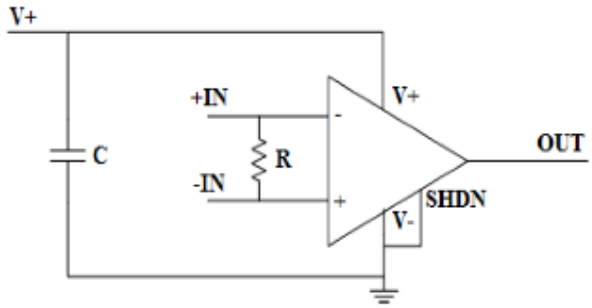

Figure 102: Schematic of the TLV3501 circuit

The comparator was supplied with a positive supply voltage of 3V applied on the V+ pin; the V- pin was connected to ground. The V+ and V- pins were decoupled using a 0.1µF capacitor. Also the +IN pin was grounded and the −IN pin was connected to the input signal to square, generated by the Colpitts and Pierce oscillator modules. The +IN and −IN pins were connected with a 1kΩ resistor acting as a feedback signal to stabilize the comparator oscillation between the LOW and HIGH logic signal. SHDN pin was grounded and the output signal was collected on the OUT pin.

Squared signals: Colpitts oscillators

The output signal generated by the Colpitts oscillator modules were squared using the TLV3501 comparator circuit. The output signals are shown in Figures 103-110:

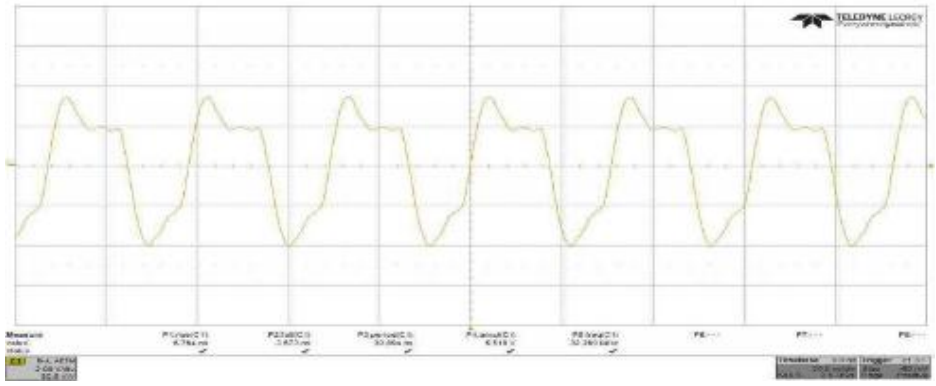

Figure 103: Squared output signal of the first Colpitts oscillator module, generated by the TLV3501 comparator circuit. Each PCB contains 8 oscillator modules to drive totally 8 QCMs.

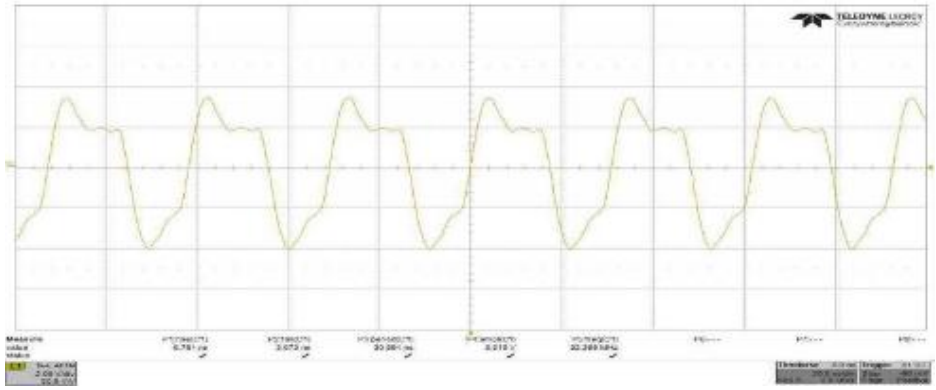

Figure 104: Squared output signal of the second Colpitts oscillator module, generated by the TLV3501 comparator circuit. Each PCB contains 8 oscillator modules to drive totally 8 QCMs.

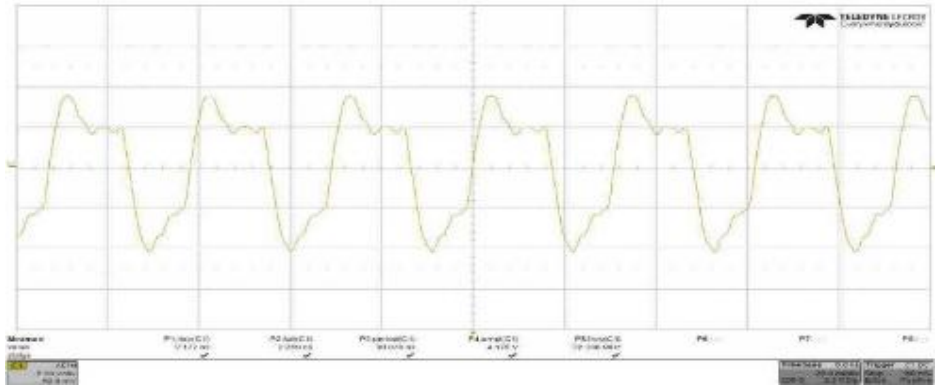

Figure 105: Squared output signal of the third Colpitts oscillator module, generated by the TLV3501 comparator circuit. Each PCB contains 8 oscillator modules to drive totally 8 QCMs.

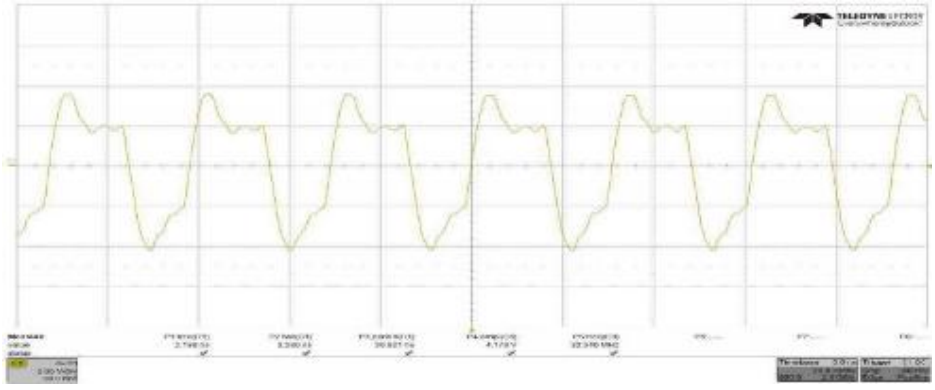

Figure 106: Squared output signal of the fourth Colpitts oscillator module, generated by the TLV3501 comparator circuit. Each PCB contains 8 oscillator modules to drive totally 8 QCMs.

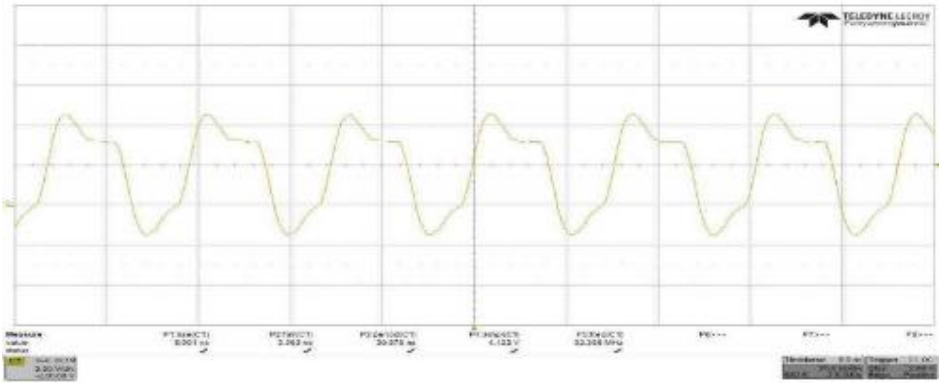

Figure 107: Squared output signal of the fifth Colpitts oscillator module, generated by the TLV3501 comparator circuit. Each PCB contains 8 oscillator modules to drive totally 8 QCMs.

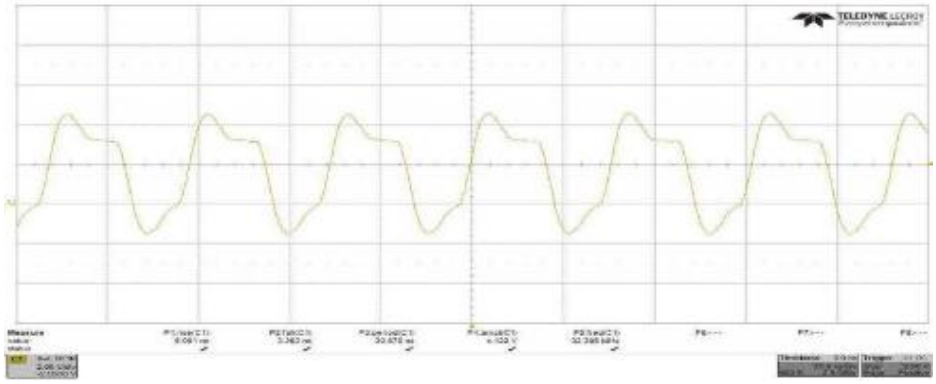

Figure 108: Squared output signal of the sixth Colpitts oscillator module, generated by the TLV3501 comparator circuit. Each PCB contains 8 oscillator modules to drive totally 8 QCMs.

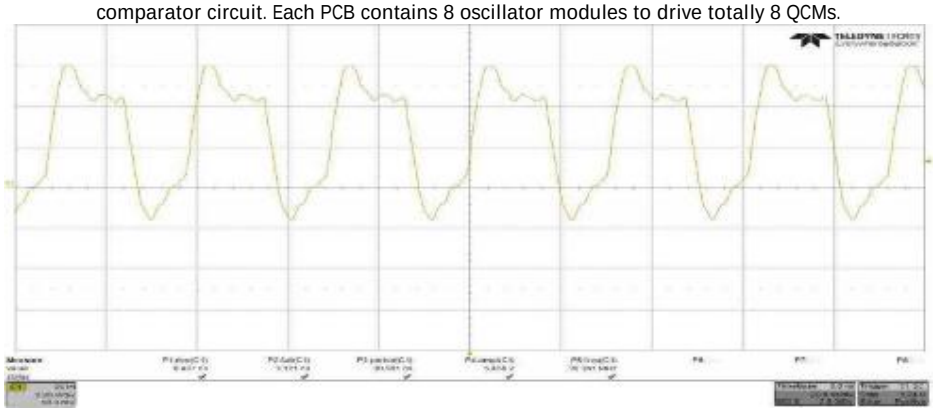

Figure 109: Squared output signal of the seventh Colpitts oscillator module, generated by the TLV3501 comparator circuit. Each PCB contains 8 oscillator modules to drive totally 8 QCMs.

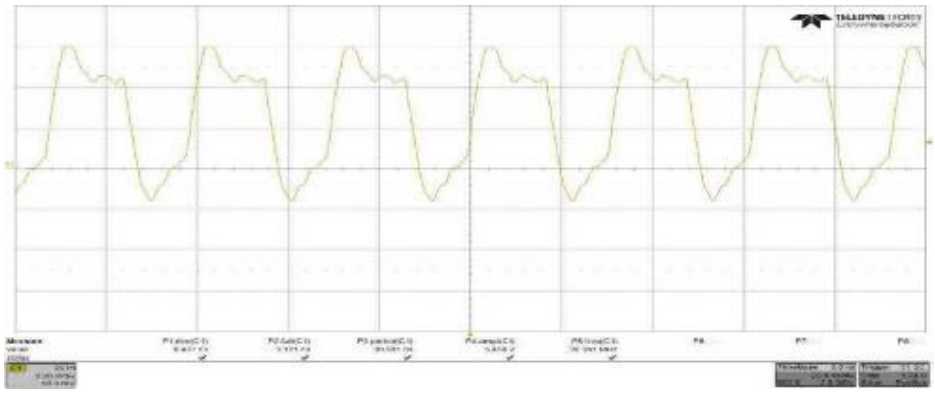

Figure 110: Squared output signal of the eighth Colpitts oscillator module, generated by the TLV3501 comparator circuit. Each PCB contains 8 oscillator modules to drive totally 8 QCMs.

The over/undershoot phenomena of the squared signal are due to compensation issues of the probes and to the asymmetry of the sinusoidal input wave. However, the frequency of the squared signals is of about 32.4MHz with a peak-to-peak amplitude of about 4.8V that is compatible with the input logical levels of the acquisition stage.

Squared signals: Pierce oscillators

The output signal generated by the Pierce oscillator modules were squared using the TLV3501 comparator circuit. The output signals are shown in Figures 111-118:

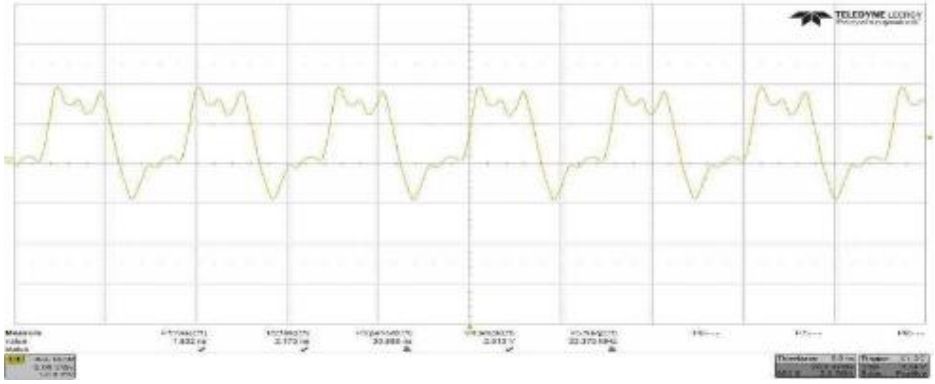

Figure 111: Squared output signal of the first Pierce oscillator module, generated by the TLV3501 comparator circuit. Each PCB contains 8 oscillator modules to drive totally 8 QCMs.

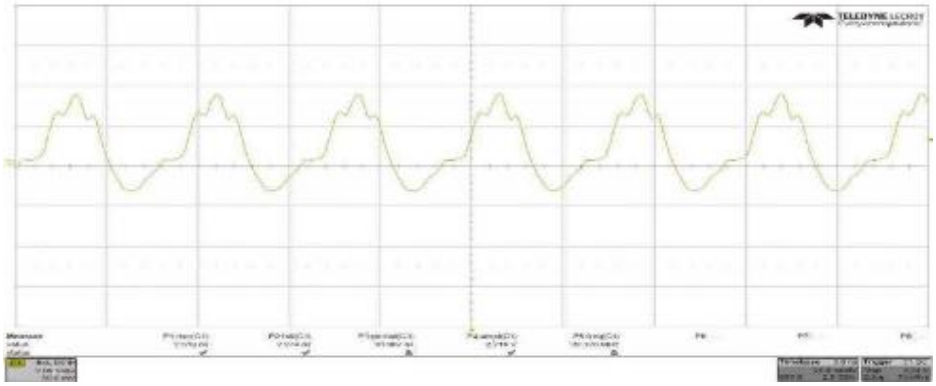

Figure 112: Squared output signal of the second Pierce oscillator module, generated by the TLV3501 comparator circuit. Each PCB contains 8 oscillator modules to drive totally 8 QCMs.

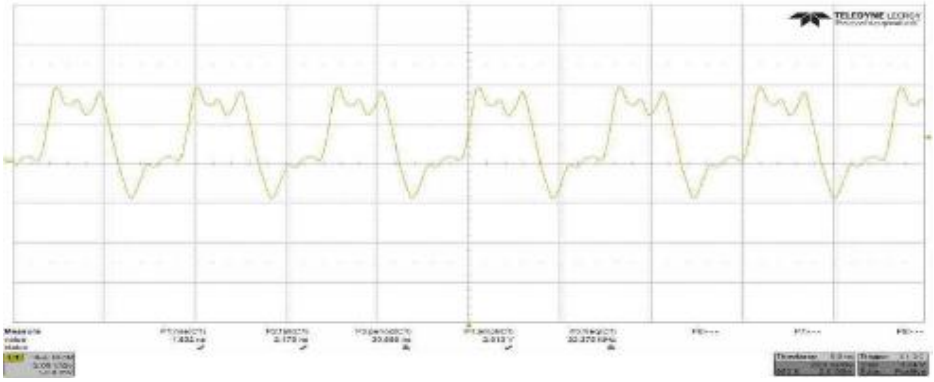

Figure 113: Squared output signal of the third Pierce oscillator module, generated by the TLV3501 comparator circuit. Each PCB contains 8 oscillator modules to drive totally 8 QCMs.

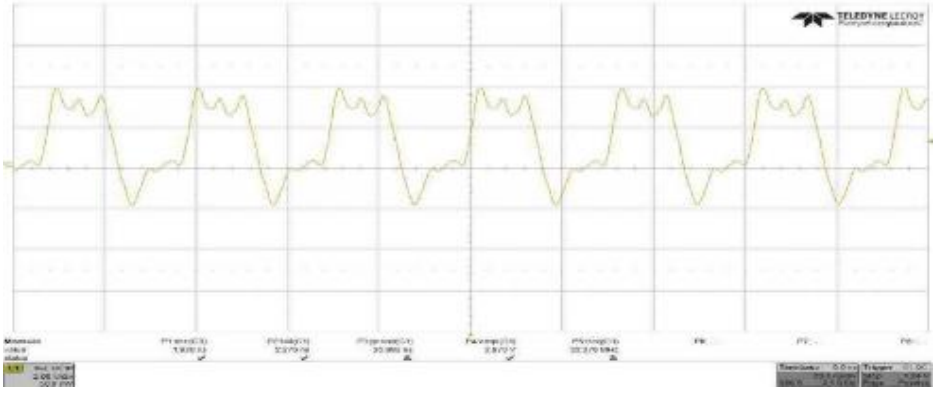

Figure 114: Squared output signal of the fourth Pierce oscillator module, generated by the TLV3501 comparator circuit. Each PCB contains 8 oscillator modules to drive totally 8 QCMs.

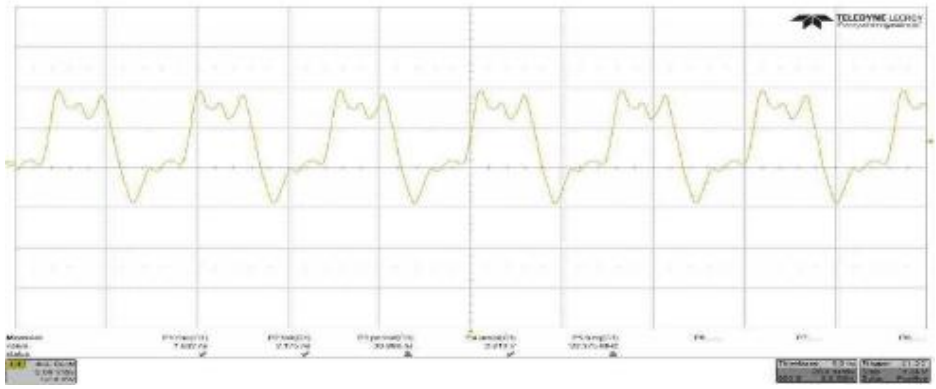

Figure 115: Squared output signal of the fifth Pierce oscillator module, generated by the TLV3501 comparator circuit. Each PCB contains 8 oscillator modules to drive totally 8 QCMs.

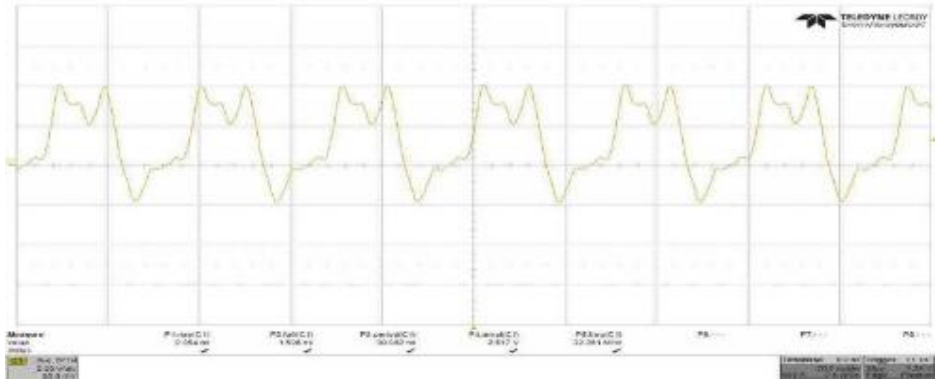

Figure 116: Squared output signal of the sixth Pierce oscillator module, generated by the TLV3501 comparator circuit. Each PCB contains 8 oscillator modules to drive totally 8 QCMs.

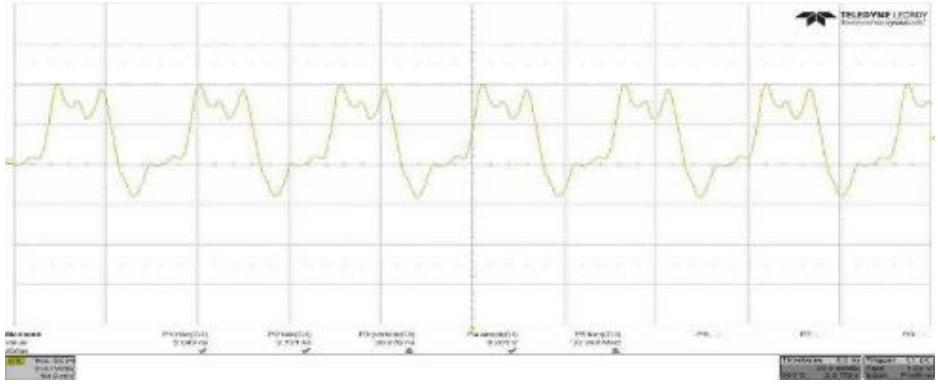

Figure 117: Squared output signal of the seventh Pierce oscillator module, generated by the TLV3501 comparator circuit. Each PCB contains 8 oscillator modules to drive totally 8 QCMs.

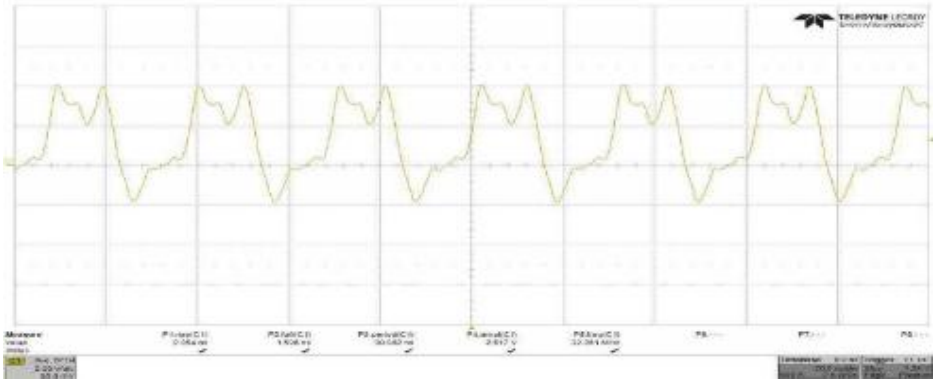

Figure 118: Squared output signal of the eighth Pierce oscillator module, generated by the TLV3501 comparator circuit. Each PCB contains 8 oscillator modules to drive totally 8 QCMs.

The over/undershoot phenomena of the squared signal are due to compensation issues of the probe. However, the frequency of the squared signals is of about 32.4MHz with a peak-to-peak amplitude of about 2.75V.

Signal acquisition and conversion

The acquisition of the squared signals generated by the TLV3501 comparator circuits was performed using the Atmel AT91SAM3X8E microcontroller, implemented in the Arduino DUE board. A custom GUI was realized in MATLAB in order to visualize and save the output data. The Arduino Due is a microcontroller board based on the Atmel AT91SAM3X8E.

Microcontroller	AT91SAM3X8E
Operating Voltage	3.3V
Input Voltage (recommended)	7-12V
Input Voltage (limits)	6-16V
Digital I/O Pins	54 (of which 12 provide PWM output)
Analog Input Pins	12
Analog Output Pins	2 (DAC)
Total DC Output Current on all I/O lines	130 mA
DC Current for 3.3V Pin	800 mA
DC Current for 5V Pin	800 mA
Flash Memory	512 KB all available for the user applications
SRAM	96 KB (two banks: 64KB and 32KB)
Clock Speed	84 MHz

Table 16: Arduino DUE technical specifications

Figure 119: Arduino DUE board

To measure the frequency of the signal generated by the QCMs, it's necessary to take advantage of the AT91SAM3X8E internal registers: each of the three 32bit Timer Counter (TC) modules includes three identical TC channels. Each TC channel can be independently programmed to perform a wide range of functions including frequency measurement, event counting, interval measurement, pulse generation, delay timing and pulse width modulation.

Each channel has three external clock inputs, five internal clock inputs and two multi-purpose input/output signals, which can be configured by the user. Each channel drives an internal interrupt signal, which can be programmed to generate processor interrupts.

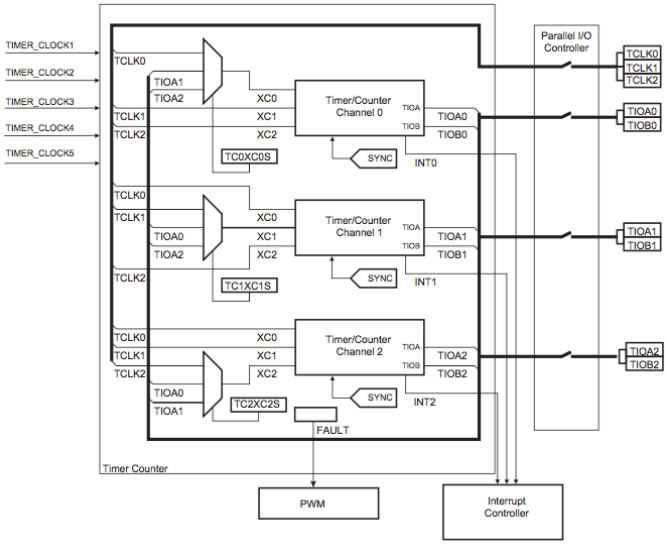

Figure 120: Timer Counter Block Diagram

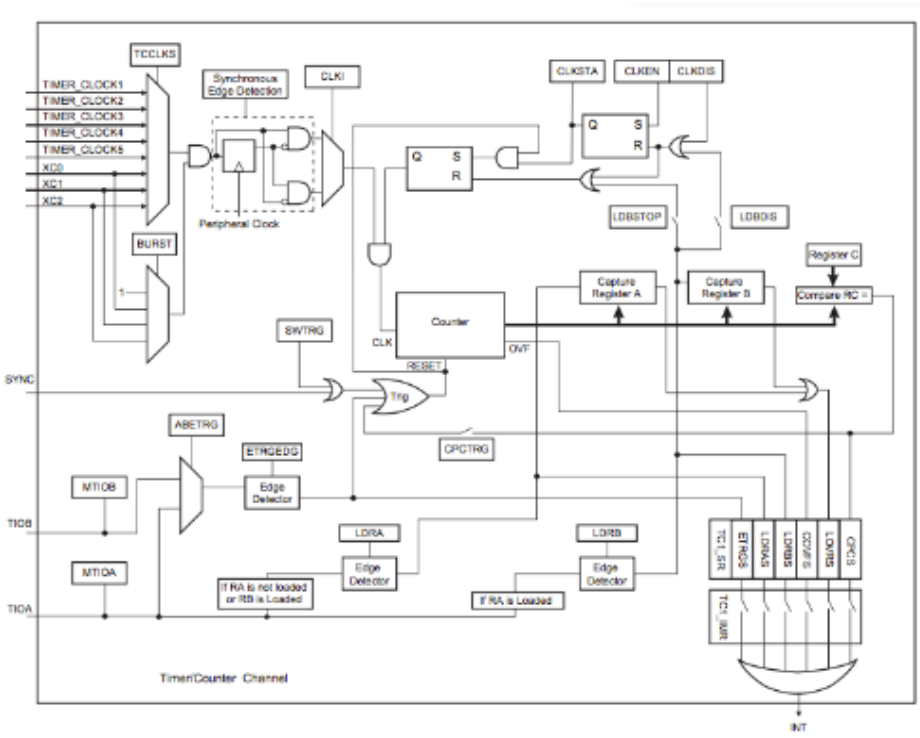

Figure 121: Counter Block Diagram

Obtaining the frequency of a digital signal is quite simple. For a simple digital signal, such as a square wave, the period is simply the time between rising edges, or even falling edges.

$$Period\,(s) = \frac{1}{Frequency}\,(Hz)$$

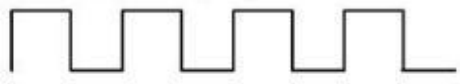

Figure 122: Ideal Square Waveform

For a high-frequency signal, it's necessary to use two counters. A paired counter (two counters) generates a pulse train with a user-specified period, "measurement time" (see Fig. 97), much larger than that of the signal you are measuring but small enough to prevent counter overflow.

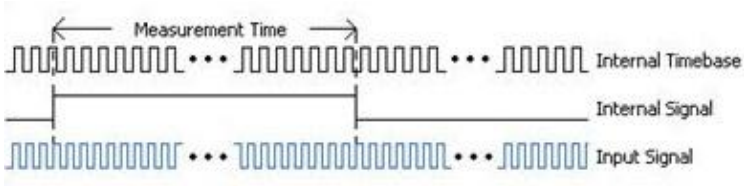

Figure 123: Digital Signal Frequency Measured with Two Counters (High Frequency)

The number of ticks of the Input Signal is counted over the known period of time provided by the Internal Signal. Dividing the number of ticks by the known measurement time gives the frequency of the Input Signal.

$$f = \frac{ticks\ number}{measurement\ time\ (s)}$$

To have a good frequency measurement, it is necessary to use a stable reference clock that generates a very precise time-base and so a very precise measurement time window. The used external time-base clock is the IQXO-350, a commercial oscillator produced by the IQD Frequency Products Inc. It produces a square wave with a frequency of 10Mhz and a tolerance of ±25ppm. The supply voltage of the oscillator is 5V.

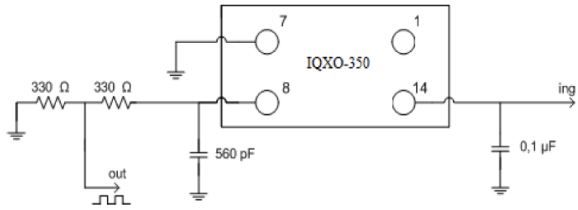

Figure 124: IQXO-350 circuit

So the external clock, based on the IQXO-350, generates the Internal time-base signal and Input Signal is generated by each QCMs connected to the counter registers of the microcontroller.

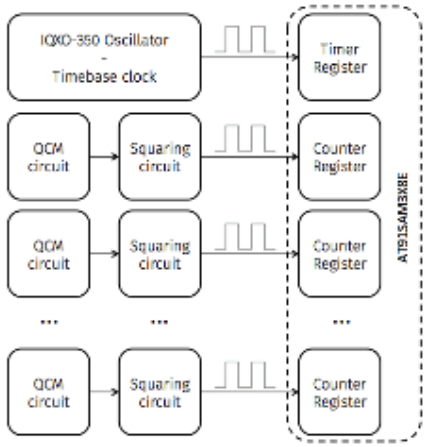

Figure 125: Logical layout of the frequency measurement strategy

One timer register of the AT91SAM3X8E microcontroller was connected to the IQXO-350 and receives as input the 10MHz square wave. This signal is the internal time-base that controls the measurement time window. The measurement time was set at 1s: the microcontroller was programmed so that every 1 million clock ticks (equal to 1s) the timer counter triggers an interrupt routine acquires the ticks number stored in the counter registers connected to the QCMs.

Module	TC	Channel	Port Pin of µC	Pin on Arduino Due Board
IQXO-350	TC0	0	PB 26	Digital Pin 22
Module 1	TC0	1	PA 4	Analog In 5
Module 2	TC0	2	PA 7	Digital Pin 31
Module 3	TC1	0	PA 22	Analog In 3
Module 4	TC1	1	PA 23	Analog In 2
Module 5	TC1	2	PB 16	DAC1
Module 6	TC2	0	PC 27	/
Module 7	TC2	1	PC 30	LED "RX"
Module 8	TC2	2	PD 9	Digital Pin 30

Table 17: Connection between oscillator modules and microcontroller registers

A custom GUI was developed in the MATLAB programming environment: the GUI allows the visualization of the measured frequency of the signals generated by each QCM. The measured values are shown both graphically into a chart and numerically, below the graph. The visualized data are stored and can be salved at the end of the measurement into a .mat file.

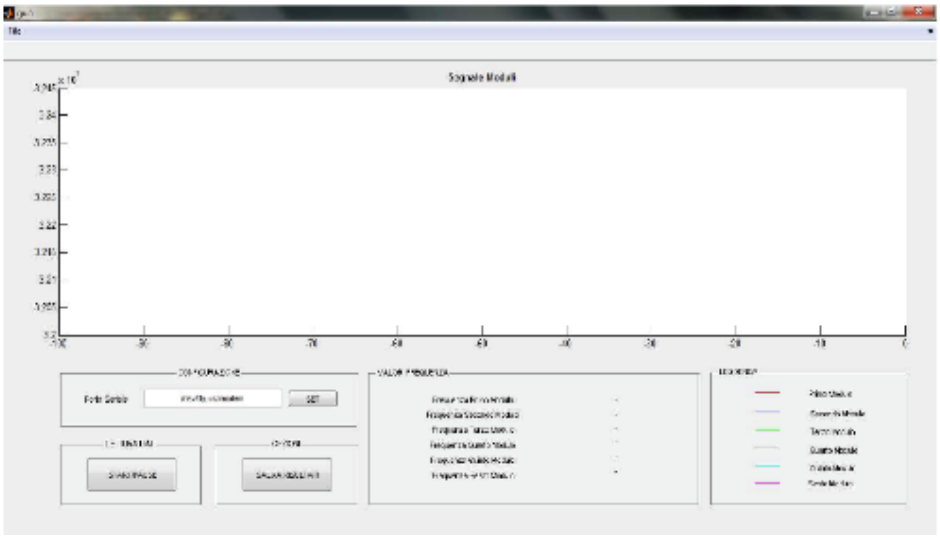

Figure 126: MATLAB GUI

Surface functionalization of the quartz crystals

The quartz crystals need to be properly processed to become gas sensors: the surface of the adsorbent material plays a fundamental role in the analysis of adsorption phenomenon because it is directly related with the sensitivity, the selectivity, the stability and the reversibility of the sensor. The surface of the quartz crystal is functionalized through the deposition of a layer of sensitive material on the acoustically active area.

The QCMs were functionalized using anthocyanins, natural pigments widely distributed in nature. They are produced by plants as secondary metabolites responsible for the pigmentation of many flowers, fruits and vegetables [63]. Regardless to the heterogeneous nature of the molecule, all the anthocyanins belong to the flavonoid group of polyphenols and share a common structure. The main part of an anthocyanin is the flavylium cation, which contains conjugated double bonds and is responsible for light absorption. This peculiar feature makes the pigments to appear coloured to the human eye [64]. Thanks to the complexity of the biological matrix in which the molecules are naturally embedded, the anthocyanins can interact with themselves as well as with other compounds including co-pigments and metal ions [65].

So far, the anthocyanin class of molecules with its extensive complexity and heterogeneous chemical behaviour seems to represent an excellent candidate for fundamental studies in the material science context and for a variety of innovative applications, by using them as sensing materials for opportune transducers.

The deposition of the anthocyanin layer was performed using the drop-casting technique (Fig. 127): the method is to dissolve the anthocyanins into a volatile solvent (methanol) and then to drop a known quantity of solution on the

surface to functionalize. When the solvent is completely evaporated, a thin film of anthocyanins will be created on the surface of the quartz crystals.

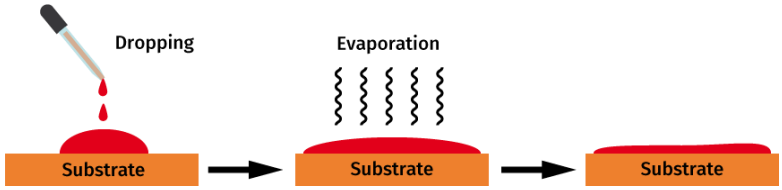

Figure 127: Drop-casting technique scheme

In principle, film thickness depends on the volume of solvent and the particle concentration, both of which can be easily varied. There are also other variables that affect the film structure such as how well the solvent wets the substrate, evaporation rate, capillary forces associated with drying, etc.

One drawback of drop-casting is that even under near ideal conditions, differences in evaporation rates across the substrate or concentration fluctuations can lead to variations in film thickness or internal structure. However, drop-casting does serve a quick and accessible method to generating thin films on relatively small substrates.

E-nose system testing: experimental setup

A specific experimental setup was developed to test the performances of the e-nose system. The layout of the experimental layout is shown in Fig. 128:

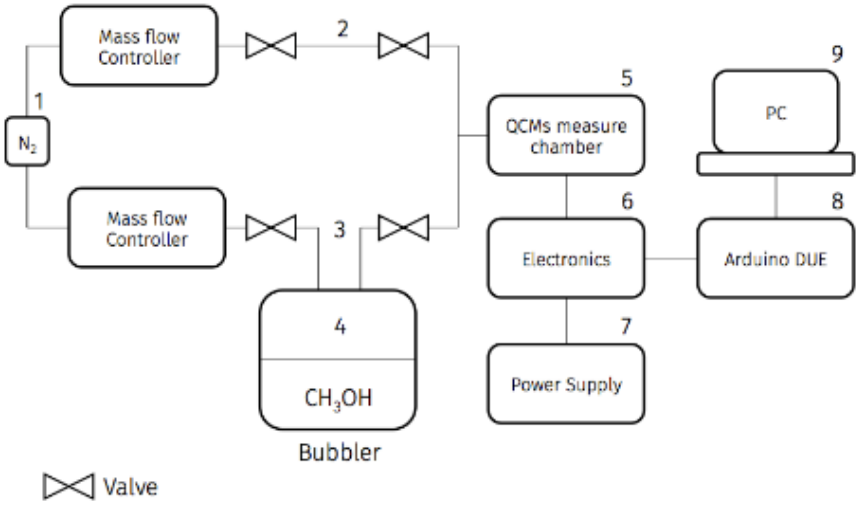

Figure 128: Logical layout of the experimental setup

The experimental setup is made up of several elements:

1. Nitrogen source
2. Nitrogen channel: in this channel pure nitrogen flows
3. Methanol channel: in this channel nitrogen flows into a Methanol bubbler generating a CH_3OH saturated gas flow.
4. Methanol bubbler: this chamber contains liquid methanol
5. QCMs measure chamber: the measure chamber contains the QCM sensor. The measurand gas flow composed by a percentage of pure nitrogen and a percentage of methanol reaches the QCM sensors into the measuring channel.
6. Electronics needed to drive the QCMs
7. Power supply
8. Arduino Due measures the frequency if the QCMs
9. PC

Channels 2 and 3 are joined together before reaching the measuring chamber: so it's possible to produce a total gas flow with a desired methanol concentration mixed with a nitrogen gas flow used as carrier. The QCMs are located inside the measure chamber and are electrically connected with the driver electronic circuit and the reference clock circuit. The oscillation frequency of the QCMs is measured using the Arduino DUE board. The measured data are sent to the PC to be visualized and saved.

Experimental protocol

The performances of two e-nose system based on QCMs with different resonance frequencies were compared:

1. E-nose system based on 20MHz QCMs
2. E-nose System based on 30Mhz QCMs using Colpitts oscillators

It was decided to study only the 30Mhz e-nose system based on Colpitts oscillators because it showed a better stability compared to the 30MHz e-nose system based on Pierce oscillators.

The responses of the two systems for different methanol concentrations were measured following 2 different experimental protocols:

Protocol I: the methanol concentrations were measured using non functionalized QCMs. An initial cleaning stage of the sensors is performed using a 100% nitrogen flow of 400sccm for 1 hour. The experimental protocol consists of gas flow containing methanol percentages (5, 10, 15, 20%) randomly sent into the measure chamber for 2 minutes, alternated to cleaning stages obtained using absolute nitrogen gas flow for 6 minutes. Each concentration is measured 5 times.

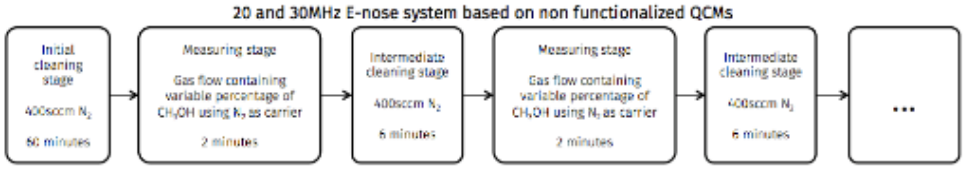

Protocol II: the methanol concentrations were measured using QCMs functionalized with antocyanins extracted from red cabbage plants. The functionalization was performed using the drop casting technique: a 1µL drop of solution, containing $1\frac{ng}{\mu L}$ of antocyanins, was placed on the surface of the quartz crystals; the crystal was subsequently baked at 40°C for about 1 hour to let the solvent evaporate, using an annealing process.

The functionalization process caused a mass variation of the QCMs and then a shift from the fundamental frequency: using the Sauerbrey equation it is possible to estimate the variation of the baseline frequency.

$$\Delta f = \frac{-2f_0^2}{A\sqrt{\mu_g \rho_q}}\Delta m$$

	Δm	f_0	A	μ_g	ρ_q	ΔHz
30 MHz QCMs	1 ng	32 Mhz	1,26 cm^2	2.947 x 10^{11} g $cm^{-1}s^{-2}$	2.648 g cm^{-3}	≈ 18 Hz
20 MHz QCMs	1 ng	20 Mhz	1,96 cm^2	2.947 x 10^{11} g $cm^{-1}s^{-2}$	2.648 g cm^{-3}	≈ 7 Hz

An initial cleaning stage of the sensors is performed using a 100% nitrogen flow of 400sccm for 2 hours. The experimental protocol consists of gas flow containing methanol percentages (5, 10, 15, 20%) randomly sent into the measure chamber for 3 minutes, alternated to cleaning stages obtained using absolute nitrogen gas flow for 9 minutes. Each concentration is measured 5 times.

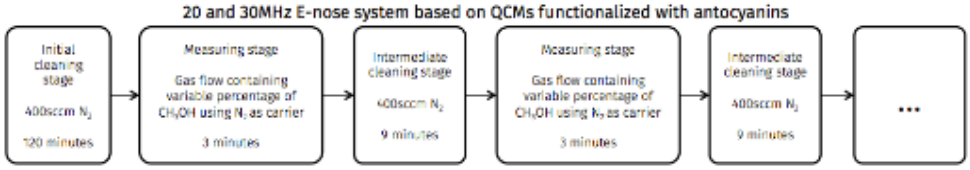

Protocol I: Experimental results

E-nose system based on non-functionalized 30MHz QCMs

Only one oscillator module with the relative QCM was tested to evaluate the performances of the system: in fact one single module can be considered perfectly representative of the entire system that has a completely modular structure.

The typical response of a QCM to a gas flow containing a variable methanol concentration is shown in Fig. 130:

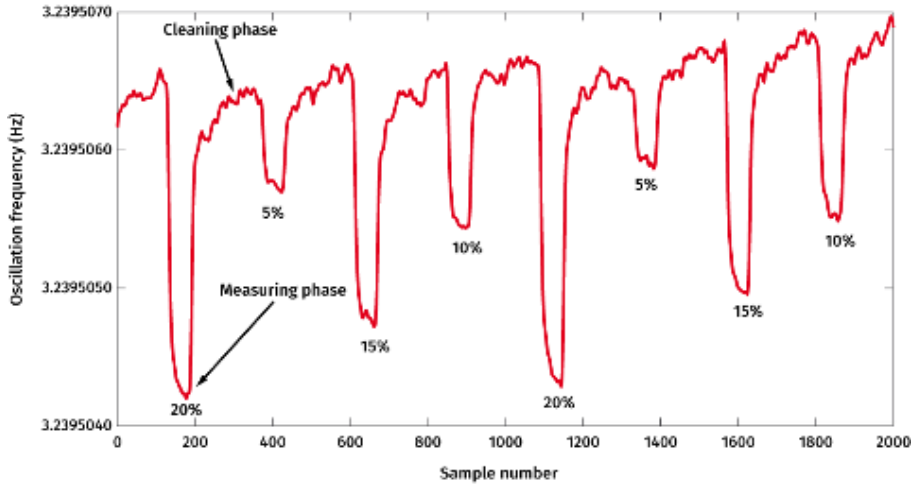

Figure 129: Sensor response to a gas flow containing a variable methanol concentration

The frequency variation of the QCM oscillation was calculated using difference between the average value of the last ten frequency values of each cleaning stage and the average value of the last ten frequency values of each measuring stage. Frequency variations are shown in Fig. 130:

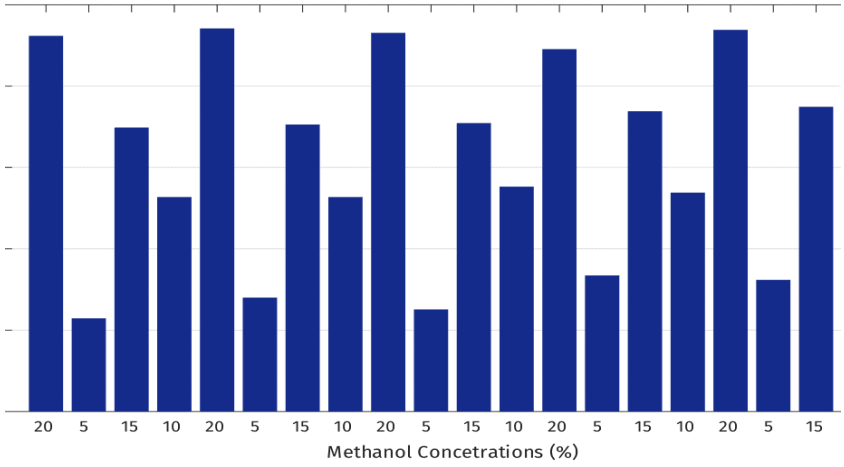

Figure 130: Frequency variations versus methanol concentrations

CH_3OH	CH_3OH	**Δf frequency**	Standard	Percentage error

concentration [%]	concentration [ppm]	variation [Hz]	deviation [Hz]	[%]
5	8293.51	7.09	1.13	7.16
10	16587.02	13.58	0.46	1.52
15	24880.53	18.00	0.55	1.38
20	33174.04	23.12	0.50	0.98

Table 18: Frequency variations, standard deviations and percentage errors of the measurements performed using the 30MHz QCMs.

A calibration curve was obtained fitting the responses of the QCMs for the measured methanol concentrations:

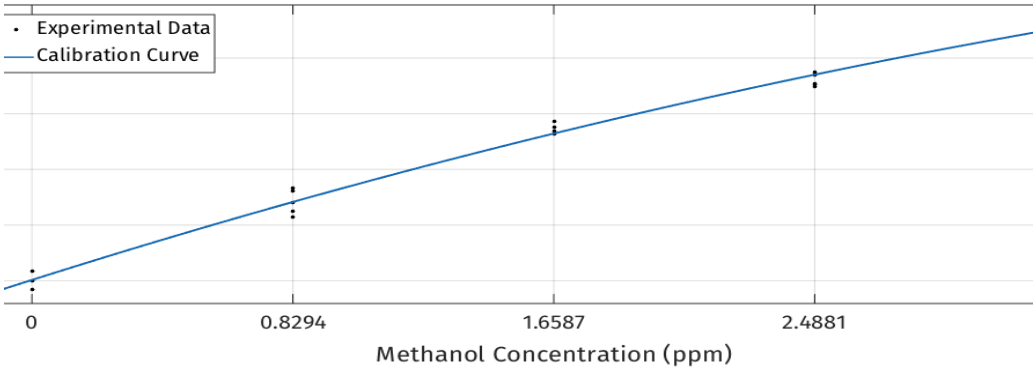

Figure 131: Frequency variations vs methanol concentrations

The output data can be fitted using a quadratic function:

$$f(x) = p_1 x^2 + p_2 x + p_3$$

$$\begin{aligned} p_1 &= \text{-6.231} \times 10^{-9} \\ p_2 &= 8.96 \times 10^{-4} \\ p_3 &= 7.013 \times 10^{-2} \\ R^2 &= 0.9921 \end{aligned}$$

The sensitivity and the resolution of the system can be expressed as:

$$S = \frac{\partial f(x)}{\partial x} = p_1 x + p_2$$

$$R = \frac{f_{NOISE}}{S} = \frac{1\ Hz}{p_1 x + p_2}$$

Where f_{NOISE} is equal to the minimum frequency variation that can be read by the data acquisition stage.

Methanol concentrations [%]	Methanol concentrations [ppm]	Sensitivity [Hz/ppm]	Resolution [ppm]

5	8293.51	0.0008443	1184.41
10	16587.02	0.0007927	1261.51
15	24880.53	0.0007410	1349.52
20	33174.04	0.0006893	1450.74

Table 19: Sensitivity and resolution performances of the system

E-nose system based on non-functionalized 20MHz QCMs

Only one oscillator module with the relative QCM was tested to evaluate the performances of the system: in fact one single module can be considered perfectly representative of the entire system that has a completely modular structure.

CH_3OH concentration [%]	CH_3OH concentration [ppm]	**Δf frequency** variation [Hz]	Standard deviation [Hz]	Percentage error [%]
5	8293.51	6.4	0.58	4.11
10	16587.02	11.4	0.67	2.64
15	24880.53	15.83	0.32	0.91
20	33174.04	18.30	0.89	2.19

Table 20: Frequency variations, standard deviations and percentage errors of the measurements performed using the 20MHz QCMs.

A calibration curve was obtained fitting the responses of the QCMs for the measured methanol concentrations:

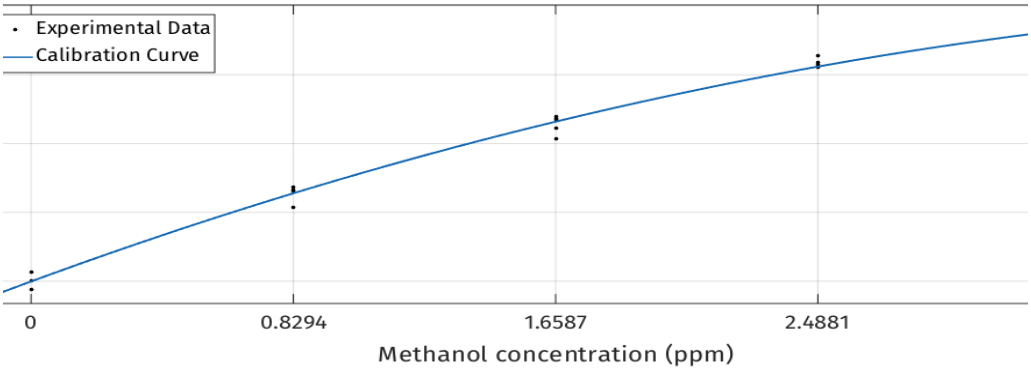

Figure 132: Frequency variations vs methanol concentrations

The output data can be fitted using a quadratic function:

$$f(x) = p_1 x^2 + p_2 x + p_3$$

$$p_1 = \text{-8.74} \times 10^{-9}$$
$$p_2 = 8.45 \times 10^{-4}$$

$$p_3 = \text{-2.44} \times 10^{-2}$$
$$R^2 = 0.9918$$

Methanol concentrations [%]	Methanol concentrations [ppm]	Sensitivity [Hz/ppm]	Resolution [ppm]
5	8293.51	0.0007728	1293.99
10	16587.02	0.0007002	1428.16
15	24880.53	0.0006278	1592.86
20	33174.04	0.0005552	1801.15

Table 21: Sensitivity and resolution performances of the system

Results comparison

The 30MHz QCMs showed better performances than the 20MHz QCMs: they have a better dynamic response and higher sensitivity. The comparison between frequency responses of the two systems are exposed in Fig 107:

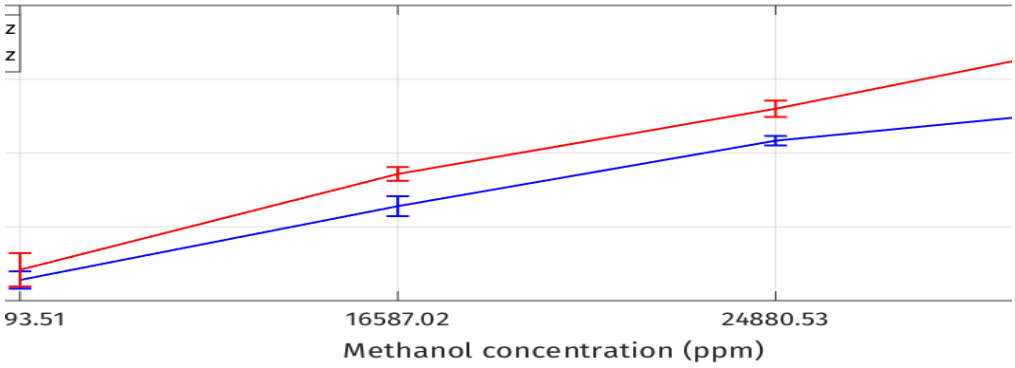

Figure 133: Comparison between 20 and 30 Mhz QCM responses

In Fig 89, the average Δf (frequency variation) and the standard deviations of the measure of the different methanol concentrations are presented: it's clear that the average responses of the 30MHz QCMs are always higher than the 20MHz QCMs responses.

Moreover, the sensitivity and resolution of the two systems were compared:

Methanol concentrations [ppm]	Sensitivity [Hz/ppm]	Sensitivity ratio of 30 and 20MHz QCMs [S_{30MHz}/S_{20MHz}]
8293.51	S_{30MHz} = 0.0008443	1.0925
	S_{20MHz} = 0.0007728	
16587.02	S_{30MHz} = 0.0007927	1.1321

	S_{20MHz} = 0.0007002	
24880,53	S_{30MHz} = 0.0007410	1.1803
	S_{20MHz} = 0.0006278	
33174,04	S_{30MHz} = 0.0006893	1.2415
	S_{20MHz} = 0.0005552	

Table 22: Sensitivities comparison

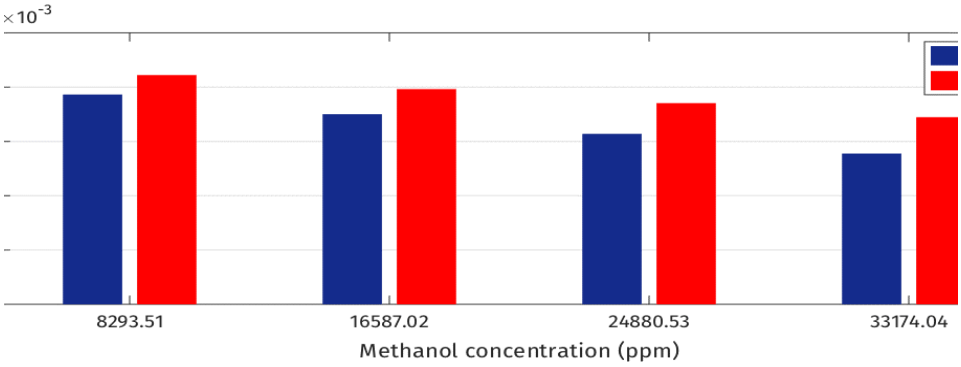

Figure 134: Sensitivities comparison

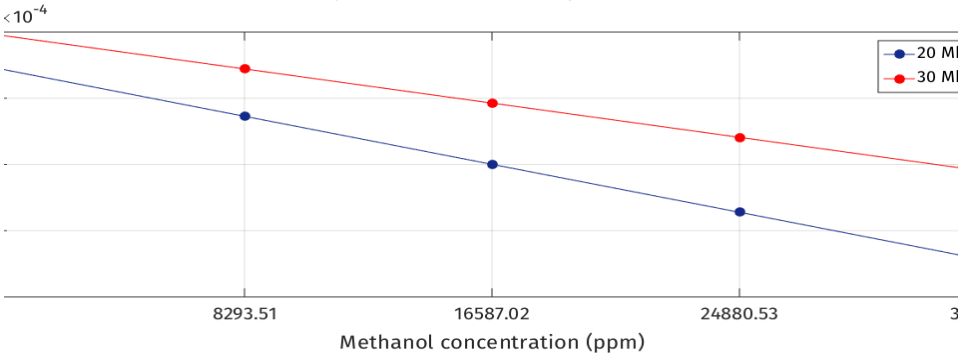

Figure 135: Sensitivities comparison

The sensitivity of the 30MHz QCM is always higher than the sensitivity of the 20MHz QCM.

Protocol II: Experimental results

E-nose system based on 30MHz QCMs functionalized with antocyanins

Only one oscillator module with the relative QCM was tested to evaluate the performances of the system: in fact one single module can be considered perfectly representative of the entire system that has a completely modular structure.

The frequency variation of the QCM oscillation was calculated using difference between the average value of the last ten frequency values of each

cleaning stage and the average value of the last ten frequency values of each measuring stage.

CH_3OH concentration [%]	CH_3OH concentration [ppm]	**Δf frequency** variation [Hz]	Standard deviation [Hz]
5	8293.51	43.33	4.15
10	16587.02	87.36	1.22
15	24880.53	145.87	4.50
20	33174.04	193.57	2.12

Table 23: Frequency variations and standard deviations of the measurements performed using the functionalized 30MHz QCMs.

A calibration curve was obtained fitting the responses of the QCMs for the measured methanol concentrations:

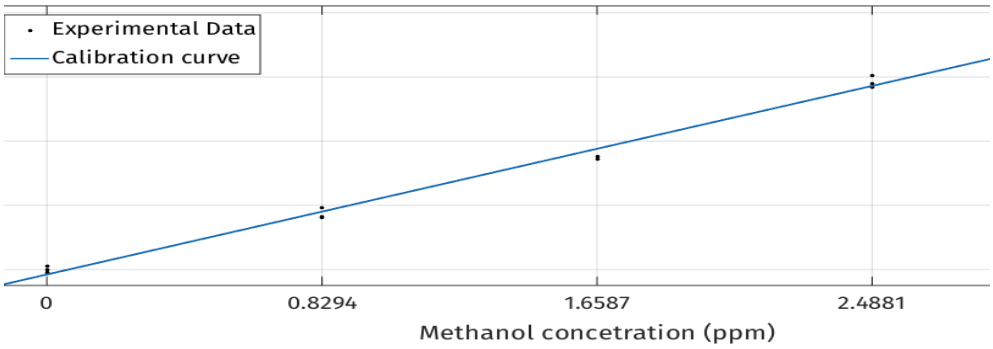

Figure 136: Frequency variations vs methanol concentrations

The output data can be fitted using a linear function:

$$f(x) = p_1 x + p_2$$

$$p_1 = \quad 5.905 \times 10^{-3}$$
$$p_2 = \quad -3.909$$
$$R^2 = \quad 0.9956$$

The sensitivity is constant for all the methanol concentrations:

$$S = \frac{\partial f(x)}{\partial x} = p_1 = 0.005905 \ \frac{Hz}{ppm}$$

$$R = \frac{f_{NOISE}}{S} = \frac{1\ Hz}{p_1} = 169.3480\ ppm$$

Where f_{NOISE} is equal to the minimum frequency variation that can be read by the data acquisition stage.

E-nose system based on 20MHz QCMs functionalized with antocyanins

Only one oscillator module with the relative QCM was tested to evaluate the performances of the system: in fact one single module can be considered perfectly representative of the entire system that has a completely modular structure.

The frequency variation of the QCM oscillation was calculated using difference between the average value of the last ten frequency values of each cleaning stage and the average value of the last ten frequency values of each measuring stage.

CH_3OH concentration [%]	CH_3OH concentration [ppm]	**Δf frequency** variation [Hz]	Standard deviation [Hz]
5	8293.51	8.97	0.88
10	16587.02	24.09	1.22
15	24880.53	45.52	5.87
20	33174.04	64.30	6.37

Table 24: Frequency variations and standard deviations of the measurements performed using the functionalized 20MHz QCMs.

A calibration curve was obtained fitting the responses of the QCMs for the measured methanol concentrations:

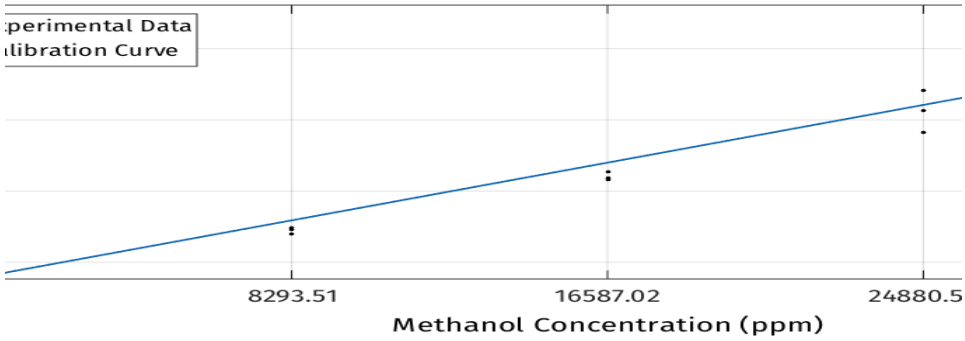

Figure 137: Frequency variations vs methanol concentrations

The output data can be fitted using a linear function:

$$f(x) = p_1 x + p_2$$

$$p_1 = \quad 1.955 \times 10^{-3}$$

$$p_2 = \quad -4.455$$
$$R^2 = \quad 0.9587$$

The sensitivity is constant for all the methanol concentrations:

$$S = \frac{\partial f(x)}{\partial x} = p_1 = 0.001195 \ \frac{Hz}{ppm}$$

$$R = \frac{f_{NOISE}}{S} = \frac{1 \ Hz}{p_1} = 511.5090 \ ppm$$

Where f_{NOISE} is equal to the minimum frequency variation that can be read by the data acquisition stage.

Results comparison

The functionalized 30MHz QCMs showed better performances than the functionalized 20MHz QCMs: they have a better dynamic response and higher sensitivity. The comparison between frequency responses of the two systems are exposed in Fig 138:

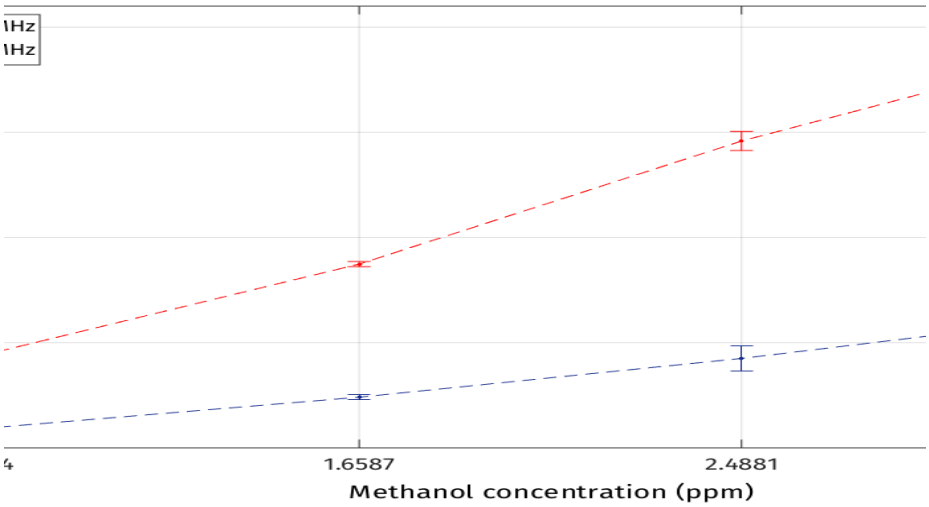

Figure 138: Comparison between 20 (blue) and 30 (red) MHz QCM responses

In Fig 138, the average Δf (frequency variation) and the standard deviations of the measure of the different methanol concentrations are presented: it's clear that the average responses of the fictionalized 30MHz QCMs are always higher than the fictionalized 20MHz QCMs responses.

Moreover, the sensitivity and resolution of the two systems were compared:

	Functionalized 30MHz QCMs	Functionalized 20MHz QCMs
Sensitivity [Hz/ppm]	0.005905	0.001955
Sensitivity ratio of 30 and 20MHz QCMs [S_{30MHz}/S_{20MHz}]	3.0205	

Table 25: Sensitivities comparison table

Comparison between functionalized and non- functionalized 30 MHz QCMs

The use of 30MHz QCMs ensures a better stability of the dynamic response and a higher sensitivity of the sensor system. Comparing the output data of functionalized and non- functionalized 30MHz QCMs, it's possible to notice that the functionalized QCMs shown a frequency variation larger than the variation of the non-functionalized QCMs on equal methanol concentrations.

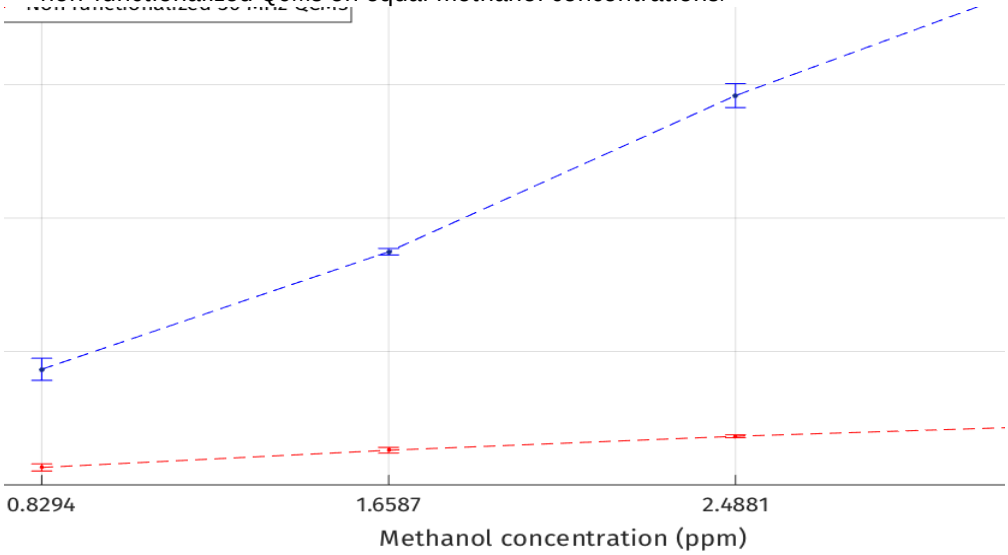

Figure 139: Comparison between output data obtained using funcionalized 30MHz QCMs (blue) and non-funcionalized 30MHz QCMs (red)

The two systems differ also in the sensitivity response: in fact non-functionalized QCMs present a non-linear (quadratic function) calibration curve across the measuring range and, on the contrary, functionalized QCMs present a linear response that generates a constant sensitivity.

Methanol concentration [ppm]	Sensitivity [Hz/ppm]	Ratio of functionalized and non-functionalized QCMs sensitivity
8293.51	$S_{non\text{-}functionalized}$ = 0.0008443 $S_{functionalized}$ = 0.005905	7.64
16587.02	$S_{non\text{-}functionalized}$ = 0.0007927	8.43

	$S_{functionalized}$ = 0.005905	
24880.53	$S_{non\text{-}functionalized}$ = 0.0007410	9.41
	$S_{functionalized}$ = 0.005905	
33174.04	$S_{non\text{-}functionalized}$ = 0.0006893	10.64
	$S_{functionalized}$ = 0.005905	

Table 26: Sensitivities comparison table

The experimental tests demonstrated that a e-nose sensor system based on QCMs with a resonance oscillation of 30MHz owns better measuring performances than a e-nose sensor system based on QCMs with a resonance oscillation of 20MHz. The use of an array of gas sensors based on 30MHz QCMs provides a new approach for the realization of a high-performance e-nose device.

Tested Applications

The multi-sensory device has been tested on several applications in the last two years: the gas and liquid sensor systems were tested severally and together into a combined device.

Particularly the e-nose system has been tested in the medical field in order to diagnose diseases like lung cancer, prostate cancer, asthma, COPDs and in food industry field applications analysing dry-cured ham, fish, mushrooms and truffles.

Also the e-tongue system has been tested in the medical field on several organic samples as urine, salive, blood and in food industry applications on olive oil, wine, water and fruit juices.

Subsequently the last tested applications are reported: all the following studies have been published on scientific journals.

E-Tongue Applications

Characterization of drinkable water [66]

Introduction

The quality of drinkable water largely influences health status and metabolism. The legislation (Directive of The European Parliament and of the Council 1998, 2009) provides criteria for the evaluation of the physicochemical and microbiological characteristics of mineral waters, setting off health-risk threshold values for some standard parameters with respect to contamination. The water potability, then, is the result of a complex examination, which takes into account epidemiological and toxicological criteria [99].

Many sensors have been developed for the analysis of water solutions with two main approaches: selective and non-selective. The ion selective electrodes (ISEs) allow potentiometric measurements, which show some advantages such as linear response and affordable determination of the ionic concentration levels. Non-selective liquid sensor arrays are based on the use of cyclic voltammetry [100] allowing the detection of qualitative changes with a good signal/noise ratio.

The application of these systems for the classification and characterization of water samples could be a topic of considerable interest and particularly in certain geographic areas where the drinking water supply lacks the usual treatments of correction and purification.

The novel e-tongue, developed in this doctoral study and previous described, was applied to perform cyclic voltammetry analysis on drinkable water samples. The device provided quick, stable and reproducible responses. The instrument, once calibrated, can be used on field allowing real-time control of bottled-water content, on-line monitoring of the distribution process and domestic verification of bottled and tap-water.

Materials and methods

Liquid sensors device

The novel e-tongue system is inspired by electrochemical measuring techniques and was designed and implemented to perform cyclic voltammetry analysis on liquid samples.

The system consists of an electrode, an input signal generator stage, a signal conditioning stage and a data acquisition stage. The device can send the acquired data to a PC; using a GUI it's possible to visualize and save the acquired data.

The electrode is a screen-printed electrode fabricated by DropSens S.L. (Llanera (Asturias), Spain): the working (4 mm diameter) electrode is made of gold, the counter electrode is made of platinum, the reference electrode is made of Ag and electric contacts are made of silver. Its dimensions (3.4 × 1.0 × 0.05 cm—Length × Width × Height) are ideal for working with 50µL volume.

Experimental set-up

The applied input signal consists of a triangular waveform, from -1 V to +1 V. The frequency of the input signal has been set to 0.01 Hz. The output signal is acquired with a sampling rate of 1 s thus collecting 100 samples of the output current, treated as a single 'fingerprint' composed of a virtual array of 100 sensors.

A volume of 3 mL is considered for each water sample and spilled in a 4 mL cuvette (normally used for spectrophotometric analysis). Then, the sensor probe is immersed in the cuvette and four cycles were run for each sample. The time duration of the complete measurement process is of about 90 s. All output data are stored in a flash memory.

A total number of 14 bottled water were analysed. Their names and characteristics are reported in Table 27. Each of them was consecutively analysed four times and the experiments on the whole set of 14 water samples were repeated five times.

Calibration procedure

In order to test the device relevance to water analysis, a preliminary calibration procedure was conducted with the following saline matrices: sodium, potassium, magnesium and calcium chlorides, diluted in distilled water at the common concentration levels of bottled and tap-water. In particular, the following concentration ranges were tested for each salt: NaCl (5, 15, 30, 50, 75 mg/L); $CaCl_2$ (20, 60, 120, 240, 360 mg/L); KCl (0.5, 1.5, 5, 20, 50 mg/L); $MgCl_2$ (5, 10, 25, 40, 50 mg/L).

Commercial Name	Dry Residue (mg/L)	Electrical conductivity **(µs/cm)**	Calcium (mg/L)	Bicarbonates (mg/L)	Sodium (mg/L)	Potassium (mg/L)
Amorosa	28	43	0.7	7.3	4.7	0.11
Levissima	80.2	118	19.9	57	1.9	1.7
Panna	141	222	32	103	6.7	0.9
Fiuggi	145	165	21	98	6.3	7
Rocchetta	177.5	281.8	57.69	181.6	4.52	0.5

Tione	180	213	16.7	98	16.4	21
S. Benedetto	313	492	87.9	330	4	1.2
Vitasnella	400	584	86	314	3.3	1.4
Di Nepi	576	785	77.5	415	29.9	42.5
Egeria	650	940	86.5	491.2	41.5	63
Uliveto	762	1122	172	574	73.1	7.3
Lete	840	1264	306	960	5	1.9
S. Pellegrino	915	1125	174	245	33.3	2.2
S. Gemini	932	1365	326	1155	19.5	3.43
Ferrarelle	1370	1850	392	1433	50	50

Table 27: Parameters of considered water samples

Data analysis

The 100 current values, acquired during a single voltammetry cycle, were treated as 100 different virtual sensors and analysed via multivariate data analysis techniques, such as principal component analysis (PCA) and partial least square discriminant analysis (PLS-DA). Multivariate data analysis was performed using PLSToolbox (Eigenvector Research Inc., Manson, WA, USA) in Matlab Environment (The MathWorks, Natick, MA, USA).

The technique used for the validation of the model is the leave one out: each of the measurements composing the data set is used as test-sample when it is left-out (leave-one-out) of the train set, formed by all the other measurements.

Results and discussion

Calibration

The PLS-DA models calculated on the calibration data set of each saline solution showd Root Mean Square Error in Cross Validation of 2.9 mg/L, 17.3 mg/L, 1.9 mg/L, 1.3 mg/L for NaCl, $CaCl_2$, KCl, $MgCl_2$, respectively. These performances confirm an affordable utilization of the sensor system in the analysis of water samples.

Different bottled-water samples discrimination

A PCA model was calculated on the collected data, obtaining the score plot of the first two principal components (PCs) reported in Fig. 140.

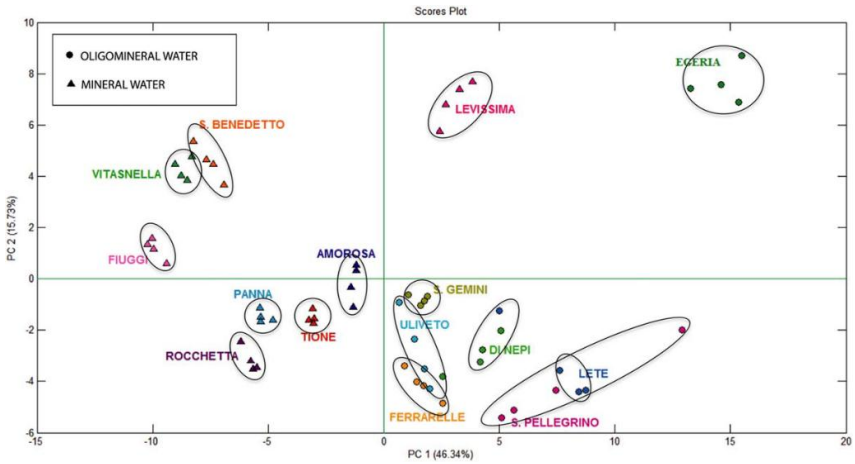

Figure 140: PCA Results: Scores plot. Principal component 1 (PC1), explained variance 45.05%; Principal component 2 (PC2), explained variance 16.80%.

Fig. 140 shows a good discrimination between water samples with a total dissolved solids (or dry residue) value lower and higher than 500 mg/L, which is the threshold discriminating between oligomineral (triangular labels in the figure 140) and mineral waters (circular label in the figure 114).

Moreover each different water sample shows a compact cluster allowing the discrimination of the 14 typologies as characterized in Tab. 27.

Physicochemical parameters prediction

A linear regression model (based on PLS technique) was built, using the same data employed for the PCA model, in order to make the system capable of providing information on unknown water samples or monitoring the shifting with respect to the parameters reported on the labels.

The device was used to predict the physicochemical parameters extracted by the commercial labels of the water samples: examining the scatter plots in Fig. 141, a good performance is evident for each of the considered parameters.

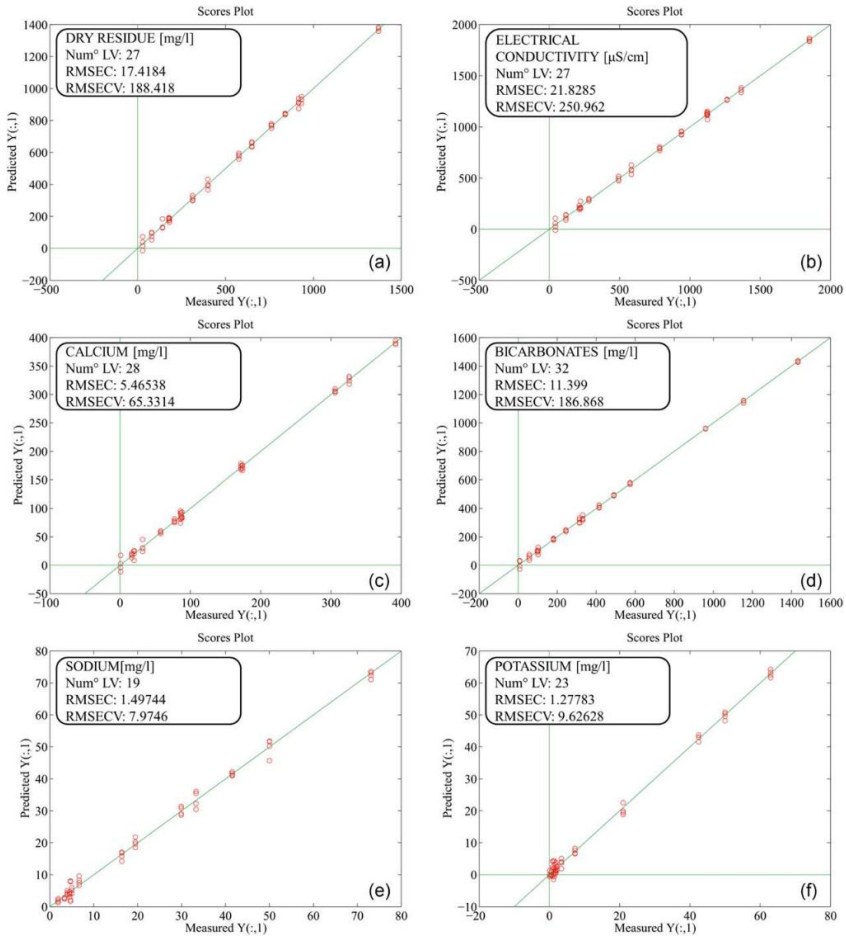

Figure 141: PLS scatter plots: predicted Y (y-axis) versus measured Y (x-axis), where Y is respectively: (a) Dry residue, (b) electrical conductivity, (c) calcium, (d) bicarbonates, (e) sodium, (f) potassium.

It is worth remarking that the 'measured' values were taken from bottle labels and not measured during this research. These parameters reliability is based on the purveyors' measurements and not on further measurements performed during the current study. In fact, the values reported on the label are relative to the analysis performed in 'one-shot' (periodical: 5 years) measurement, by an external laboratory certifying the water content of the bottle and they are not relative to the same water sample measured with the system here tested.

Thus, a considerable part of the calculated errors is because of the variability of the values of the concentration used as 'measured' and reported on the water bottle.

Conclusions

The developed e-tongue system is able to discriminate different samples of commercial drinkable water without any chemical functionalization. The device

is also able to predict physicochemical parameters reported on the bottle-label with an acceptable error.

In particular, using the PCA, the system is able to distinguish samples with a dry residue lower and higher than 500 mg/L, which corresponds to the distinction between oligomineral and mineral waters.

The developed system can provide an online analysis to monitor the water before and after bottling thus evidencing anomalies during production processes, distribution and conservation.

Non-invasive monitoring of lower-limb ulcers [67]

Introduction

Cutaneous ulcers consist of a loss of substances from epidermic, dermic and deeper layers down to the bones; healing process needs of at least 6 weeks [68]. Among them, lower-limb ulceration has an overall incidence of 1.2-3.2% , which is of 5% [69] for people aged over 65; it heavily affects quality of life with a considerable economical and social impact.

Different methods have been developed to predict the outcome of skin ulcers and to measure the effectiveness of treatment. Most commonly, these methods are based on the visual monitoring of the initial area of the ulcer and its changes over time, compared with the predicted healing time of the lesion [70]. These approaches are not easily implemented because their results may be influenced by measurement errors, especially in case of irregular ulcers or depending on the experience of the operator. Another approach is based on biopsy for the measurement of the local degree of inflammation and cytokine production, but this is not routinely used in the clinical practice. A promising approach is based on the analysis of elastase and metalloproteinase activity on ulcers exudate [71].

Thus, the main goal of this experimental study was to test the electrochemical fingerprinting of biological samples in solution in term of diagnostic accuracy and of feasibility when applied to the study of lower-limb ulcers, where the biological sample consists of ulcer's exudate.

The developed e-tongue system was tested as diagnostic device of non-invasive monitoring of lower-limb ulcers via electrochemical analysis of the ulcers exudate, together with its ability of classifying disease stage and evolution, also in relation with critical parameters.

Materials and Methods

Liquid Sensors System

The used e-tongue system is inspired by electrochemical measuring techniques and was designed and implemented to perform cyclic voltammetry analysis on liquid samples.

The system consists of an electrode, an input signal generator stage, a signal conditioning stage and a data acquisition stage. The device can send the acquired data to a PC; using a GUI it's possible to visualize and save the acquired data.

The electrode is a screen-printed electrode fabricated by DropSens S.L. (Llanera (Asturias), Spain): the working (4 mm diameter) electrode is made of gold, the counter electrode is made of platinum, the reference electrode is made of Ag and electric contacts are made of silver. Its dimensions (3.4 × 1.0 × 0.05 cm—Length × Width × Height) are ideal for working with 50µL volume.

The applied input signal consists of a triangular waveform, from -1 V to +1 V. The frequency of the input signal has been set to 0.01 Hz. The output signal is acquired with a sampling rate of 1 s thus collecting 100 samples of the output

current, treated as a single 'fingerprint' composed of a virtual array of 100 sensors. The time duration of the complete measurement process is of about 90 s.

Study Population

This was a single-center study with 30-days follow-up carried out at the outpatient clinic of the Campus Biomedico teaching hospital in Rome between January and April 2015. The study was approved by the Ethic Committee of the Campus Biomedico University of Rome.

We enrolled 13 patients with 22 leg ulcers (many of them have more than 1 ulcer). Inclusion criteria were age ≥ 60 years and leg ulcers due to arteriosclerosis, chronic venous insufficiency, or diabetes mellitus.

Sampling method and key parameters

At baseline and after 30 days, samples were obtained from ulcer exudate and healthy skin at the proximal thigh using the same method. After careful washing with normal saline, a sterile gauze was directly applied over the site (healthy skin or ulcers), with a bandage to keep the gauze in place and protected from contamination by external agents. After 24 hours, the gauze was removed with a sterile procedure and put in a sterile container with 20 cc of normal saline. The sample was stored at 20° C for no more than 1 hour before the analysis.

Clinical evaluation

The cause of the ulcer was ascertained according to standard clinical algorithms including Doppler examination of arteries and veins of the lower limb, CT scan for the study of vessels, elettroneurography, as appropriated.

At baseline, information was collected on cardiovascular risk factors, active diseases, and current therapy. Ulcers were classified using the Leg Ulcer Measurement Tool (LUMT) [72].

A total number of 30 clinical parameters have been collected for the medical characterization of each patient. The most significant are: etiology of ulcers and severity of vascular problems (using the Leriche and CEAP classification for peripheral artery disease and chronic venous insufficiency, respectively), peripheral oxygen saturation of hemoglobin (SpO2), Transcutaneous oxygen pressure (TcPO2), diagnosis of diabetes mellitus, hypertension, hepatic cyrrhosis, chronic obstructive pulmonary disease, heart failure, malignancies and presence of anemia. Smoking exposure was also recorded, as well as results from vascular Doppler scans and angio-CT scans.

Data Analysis

We sampled twice (at the first and second evaluation, after therapy) a total of 20 ulcers (of the 22 ones measured) and corresponding areas of healthy skin.

Several models have been elaborated using the Partial Least Square Discriminant Analysis (PLS-DA) in MATLAB environment with following aims:

- Ulcers-healthy skin discrimination using the BIONOTE dataset (100-dimensional)
- Discrimination between first and second evaluation of the same ulcers using the BIONOTE dataset (100-dimensional)
- Discrimination between first and second evaluation of the same ulcers using the Clinical parameters' dataset (30-dimensional)
- Discrimination between first and second evaluation of the same ulcers using the dataset based on the 30 clinical parameters collected (30-dimensional) and using the data set based on the merge of the BIONOTE and of the clinical data (130-dimensional)
- The BIONOTE ability in the prediction of the 30 clinical parameters
- The prediction of ulcer evolution, based on the following three classes:
    - Mild/moderate healing: (LUMT I evaluation – LUMT II evaluation) in the interval from 0 to 14.
    - Good/very-good healing: (LUMT I evaluation – LUMT II evaluation) in the interval from 15 to 30.
    - Negative evolution of the ulcer: (LUMT I evaluation – LUMT II evaluation) in the interval from 0 to -30.

Results

The discrimination of the ulcer with respect to healthy skin based on BIONOTE data was correct in of 89% of the cases.

The correct discrimination percentage between the ulcer analysed at the first and at the second evaluation based on clinical data was of 75%, while the same classification problem based on the BIONOTE data shown a better performance, with a 90% of ulcers correctly identified. A model built on the BIONOTE and clinical data fusion, obtained the best performance in the correct identification of ulcers at the first and at second evaluation, giving a correct classification of 97.5%.

A model based on the BIONOTE data correctly predicted three of the 30 clinical parameters: SpO2 (Root Mean Square Error in Calibration (RMSEC): 0.99, Root Mean Square Error in Cross Validation (RMSECV): 2.37), LUMT (RMSEC: 8.21, RMSECV: 9.80) TcPO2 (RMSEC: 21.20, RMSECV: 26.16).

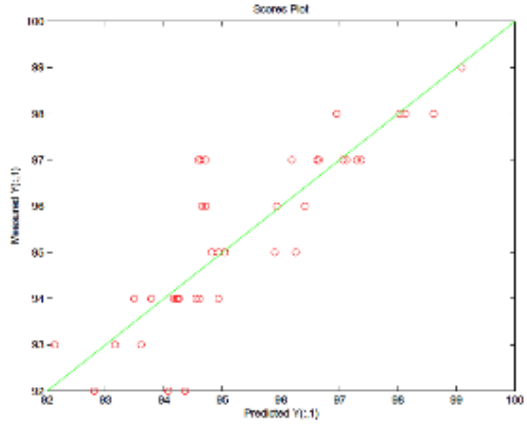

Figure 142: Predicted vs measured SpO2. The prediction is given by the PLS model built on the e-tongue data.

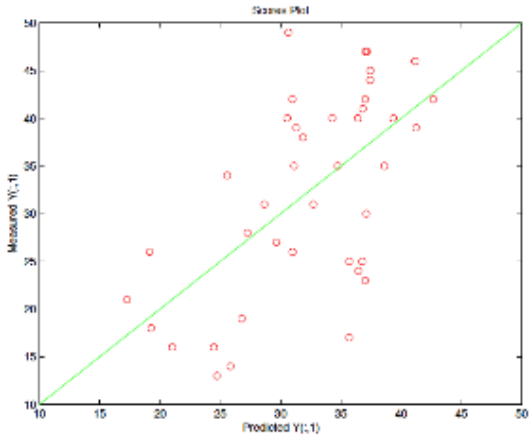

Figure 143: Predicted vs measured LUMT. The prediction is given by the PLS model built on the e-tongue data.

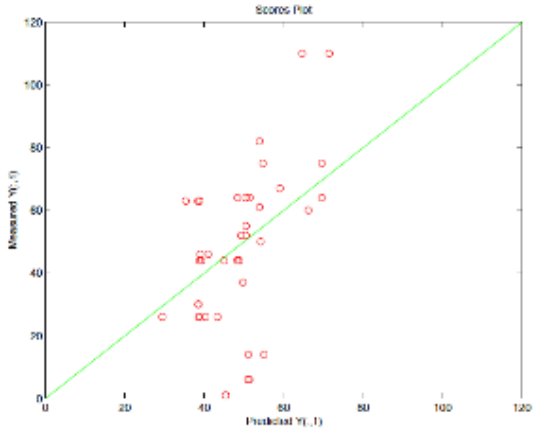

Figure 144: predicted vs measured TcPO2. The prediction is given by the PLS model built on the e-tongue data.

In order to test e-tongue ability in the evolution of the ulcers, for each lesion the healing process has been evaluated by the difference between LUMT at the first and at the second evaluation (as explained in the method section). Three classes have been defined on the basis of this differential value: The predictive power of the e-tongue system with respect to LUMT evolution based on these three classes was 100%, this means that the class of each ulcer has been correctly identified.

Conclusions

The novel developed e-tongue system could discriminate ulcers from healthy skin: this is not relevant to the diagnostic and prognostic practice, but it represents a fundamental step for the validation of the method.

Moreover the e-tongue output data correlate with SpO2, TcPO2 e LUMT, which are the most significant clinical parameters in terms of prognostics of ulcers. Thus the proposed method for ulcers' study has a predictive and discriminative potentiality.

This technique has shown to be non-invasive, easy and low cost, and to be able to increase diagnostic sensitivity of the current routine clinical practice, and to obtain the best result by a clinical and e-tongue data fusion.

The relationship between fingerprint and LUMT eventually emerged from the study. The small sample size seems adequate for a single one to one relationship in a pilot study. Indeed, such a study does not definitively prove this relationship, but it discloses it as sufficiently solid to be worthy of testing in larger and properly designed studies.

Research is needed to test this method in a more complex and numerous populations and to derive measures summarizing its classificatory and prognostic potential.

E-Nose Applications

Breath print analysis of cirrhotic patients [73]

Introduction

Chronic liver disease (CLD) has reached epidemic proportion in Western countries, and cirrhosis has become a significant global health burden all over the world [74]. Factors influencing this clinical course of CLD are extremely variable and many prognostic models and scores have been proposed in the last decades.

Among these, the Child-Pugh Classification (CPC) [75][76] and the Model for End-stage Liver Disease (MELD) [77] represent the most reliable scores for predicting mortality in end-stage liver disease. The CPC is intuitive and easy to perform at bedside, nevertheless, it has several downsides [78][79]. Therefore, estimating the prognosis of patients with cirrhosis, taking into account all the possible conditioning factors still remains a challenging issue.

Breath analysis for medical purposes may represent a new prognosis approach: it is an ancient approach, which has been validated in more recent years by the use of novel technology able to characterize the spectrum of volatile organic compounds (VOCs) in the exhaled breath [80].

It has been recently shown that a different spectrum of VOCs, identified both by e-nose [81] and by analytical technique [82] characterizes the exhaled breath of patients with cirrhosis and, among those, of patients with worse hepatic function, as described by CPC. However, the association of these different BreathPrints (BPs) with clinically relevant outcomes has not been described yet.

In this experimental application of the developed e-nose device, we aimed to compare the performance of the novel sensing system with the classical prognosis scores (CPC and MELD), associating the different BPs, identified by the sensing device, mortality and the need of hospital admission in patients with cirrhosis.

Patients and Methods

Study design and participants

89 consecutive patients with cirrhosis were recruited between November 2012 and May 2015 from those attending the Internal Medicine and Hepatology Unit of the University Hospital Campus Bio-Medico of Rome (Italy) as in-or outpatients.

The diagnosis of cirrhosis was based on the combination of clinical, biochemical, radiological and endoscopic findings, with confirmatory liver biopsy in doubtful cases. Inclusion was not restricted by aetiology of cirrhosis. Co-morbid diseases, such as diabetes mellitus, lung and heart disease, were recorded through a systematic and careful clinical history registration.

Breath collection and analysis

The e-nose used in this study is based on an array of seven quartz microbalances covered by seven different anthocyanins extracted by three different plant tissues: red rose, red cabbage, blue hortensia.

Breath collection was performed at morning with patients fasting and smoking free for at least 12 hours. Each patient was required to breath at tidal volume for 3 minutes into a dedicated storage device for direct sampling of exhaled breath (Pneumopipe®, European patent n. 12425057.2, Rome, Italy) onto an adsorbing cartridge (Tenax GR, by Supelco [83]).

The cartridge content is desorbed in four different steps (at 50, 100, 150 and 200°C) and independently processed into the sensors' chamber. Finally, the cleaning of the cartridge was obtained holding the temperature at 300°C for 5 minutes.

Once desorbed from the adsorbing cartridge, VOCs of the exhaled breath chemically bind with different anthocyanins above the seven quartz microbalances of the e-nose, inducing a frequency shift from the fundamental resonance frequency that is registered as the sensor response. The final fingerprint of the exhaled breath (BreathPrint, BP) is composed of 28 responses, given by the seven sensors' outputs at four different temperatures (50–100–150–200°C). BPs have been represented with radar plots, where the length of each equiangular radius represents the magnitude of 1 of the 28 responses.

Statistical method

The complete data set of the 28 response values was analysed by K-means clustering in order to allocate each observation into K clusters. K was fixed at 4, corresponding to the lowest value that maximized the explained variance of the model (between cluster variance/total variance = 73.7%).

Patients owning to each BP cluster were compared with respect to demographic, anthropometric and clinical characteristics. Also bilirubin, albumin and international normalized ratio (INR) were included as continuous variables and they did not show co-linearity with CPC. Presence of ascites and hepatic encephalopathy were not included in the multivariate models since they showed significant co-linearity with CPC that already includes these two variables in its algorithm.

Data were described as mean (standard deviations) or median (interquartile range) if, respectively, normally or not normally distributed and continuous, or as numbers and percentages if categorical.

Comparisons among groups were assessed by ANOVA test and statistical significance was assumed at $P<0.05$.

Results

Eighty-nine patients with cirrhosis (CPC A/B/C 37/33/19 patients) were enrolled and followed up for a median time of 23.0 months (95% CI 20.3–25.7). Mean age was 64.8 (11.3) years and 33.7% (30 subjects) were females.

Using K-means cluster analysis, four different BP clusters (labelled A, B, C and D) were identified. Mean sensor responses within each cluster have been represented on radar plot in Fig. 145.

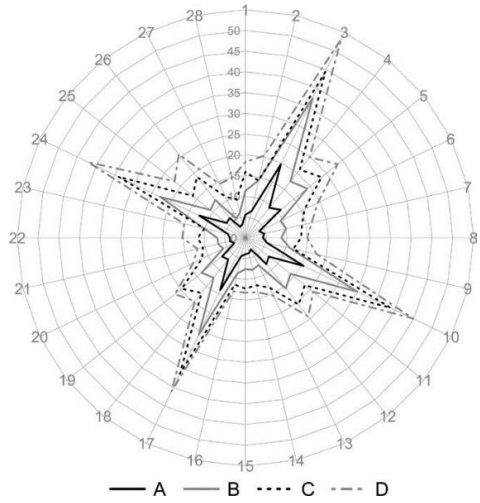

Figure 145: Radar plots of mean BP belonging to different clusters.

During the follow-up period, 37 (41.6%) participants died. The overall mortality was 33.3 per 100 person-years with mortality rates of 90.8, 23.9, 19.3, 40.9 per 100 person-years in the BP clusters A, B, C and D respectively. The corresponding mortality rate ratios were 0.3 (95% CI 0.1–0.7), 0.2 (95% CI 0.1–0.5) and 0.5 (95% CI 0.2–1.2) for BP clusters B, C and D compared to the cluster with the highest observed mortality rate (A).

Fifty subjects (56.2%, 53.5 per 100 person/years) underwent hospital admission with a hospitalization rate of 150.0, 50.9, 28.5 and 70.6 per 100 person-years among participants in the BP clusters A, B, C and D respectively. The corresponding hospitalization rate ratios were 0.3 (95% CI 0.2–0.7), 0.2 (95% CI 0.1–0.4) and 0.5 (95% CI 0.2–1.1) for BP clusters B, C and D compared to the cluster with the highest observed hospitalization rate (A).

Figure 146 shows the Kaplan-Meier estimator of the risk of mortality (panels A and C) and first hospital admission (panels B and D) associated with BP clusters. Overall, BP clusters A and D showed the worst curve of occurrence of both outcomes (log-rank P<.01).

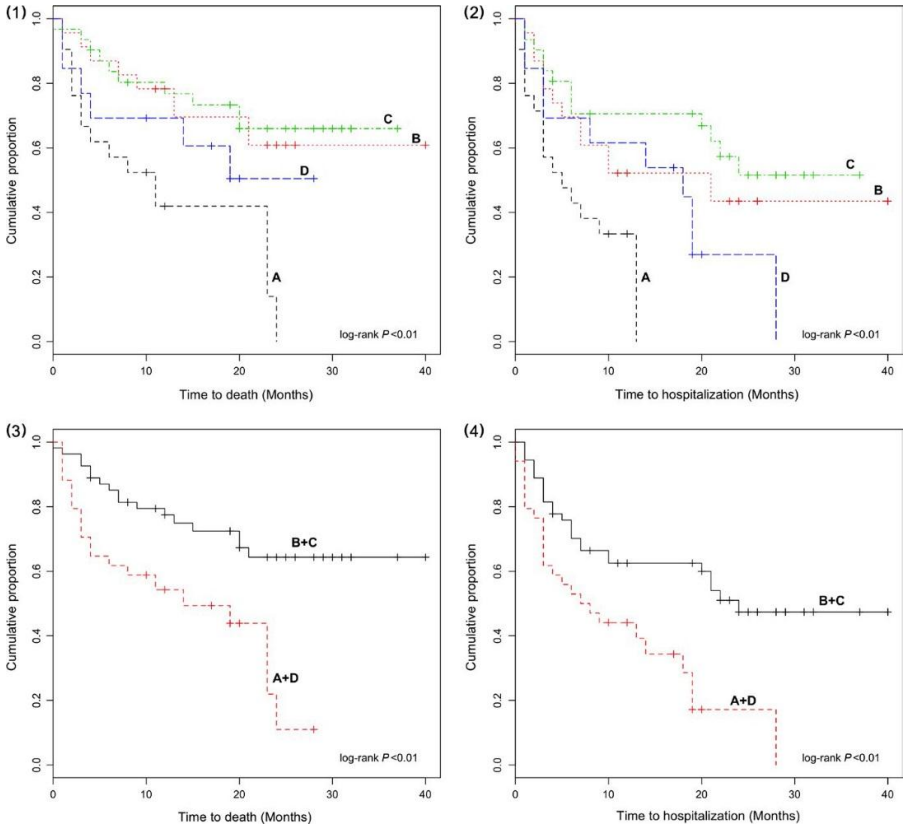

Figure 146: Kaplan–Meier curves for mortality (panels 1 and 3) and hospitalization-free survival (panels 2 and 4) for the different breath-print clusters.

Moreover, BP clusters A and D were associated with a significantly increased risk of mortality (HR 2.9, 95% CI 1.5–5.6; Table 28) and hospitalization (HR 2.6, 95% CI 1.4–4.6; Table 29) in patients with cirrhosis, even in multiple adjusted models including also CPC and MELD score (adjusted HR 2.8, 95% CI 1.1–7.0 for mortality and 2.2, 95% CI 1.1–4.2 for hospitalization; Tables 28 and 29).

CPC, but not MELD, remained the strongest factor associated with both mortality (aHR for CPC C 17.6, 95% CI 1.8–174.0; Table 28) and hospitalization (aHR for CPC C 12.4, 95% CI 2.0–75.8; Table 29).

		Univariate analysis			Multivariate analysis		
Variable		HR	Lower 95% CI	Upper 95% CI	aHR	Lower 95% CI	Upper 95% CI
Sex	F/M	1.49	0.77	2.88	0.92	0.35	2.43
Age (years)	Unit	1.01	0.98	1.05	0.99	0.94	1.05
Aetiology	Inf/n-inf	1.14	0.59	2.18	–	–	–
Child-Pugh class B	B/A	5.24	1.75	15.67	5.61	0.84	37.47

Child-Pugh class C	C/A	23.15	7.58	70.69	17.58	1.77	174.03
MELD	Unit	1.18	1.10	1.27	1.00	0.86	1.16
Number of hospitalization during FU	Unit	1.20	1.08	1.34	1.05	0.84	1.32
Hospitalization within 60 days from enrolment	Yes/no	4.88	1.90	12.56	0.54	0.13	2.33
eGFR (mL/min)	Unit	0.99	0.98	0.99	0.99	0.98	1.01
Albumin (g/dL)	Unit	0.36	0.20	0.65	0.54	0.25	1.17
Bilirubin (mg/dL)	Unit	1.40	1.23	1.59	1.32	1.01	1.72
INR	Unit	5.44	1.86	15.91	0.24	0.02	2.26
CHF	Yes/no	2.34	0.55	9.88	–	–	–
COPD	Yes/no	1.40	0.43	4.56	–	–	–
Diabetes mellitus	Yes/no	1.37	0.72	2.62	–	–	–
Current smoker	Yes/no	1.45	0.73	2.88	–	–	–
BP cluster	A-D/B-C	2.89	1.49	5.61	2.77	1.10	6.98

Table 28: (2) Cox proportional hazard models for mortality. eGFR, estimated glomerular filtration rate; MELD, Model for End-Stage Liver Disease; CI, confidence interval; FU, follow-up period; CHF, congestive heart failure; COPD, chronic obstructive pulmonary disease; inf, infective; n-inf, not infective; INR, International Normalized Ratio.

Variable		Univariate analysis			Multivariate analysis		
		HR	Lower 95% CI	Upper 95% CI	aHR	Lower 95% CI	Upper 95% CI
Sex	F/M	1.55	0.88	2.74	1.37	0.63	3.01
Age (years)	Unit	1.01	0.99	1.04	0.98	0.94	1.03
Aetiology	Inf/n-inf	1.23	0.71	2.15	–	–	–
Child-Pugh class B	B/A	4.33	1.99	9.38	5.22	1.37	19.81
Child-Pugh class C	C/A	10.69	4.71	24.24	12.38	2.02	75.84
MELD	Unit	1.18	1.11	1.27	1.08	0.94	1.24
Hospitalization within 60 days from enrolment	Yes/no	3.65	1.82	7.32	0.74	0.25	2.22
eGFR (mL/min)	Unit	0.99	0.98	1.00	1.00	0.99	1.02
Albumin (g/dL)	Unit	0.53	0.33	0.87	0.86	0.42	1.78
Bilirubin (mg/dL)	Unit	1.30	1.16	1.45	1.23	0.95	1.95
INR	Unit	5.04	1.99	12.73	0.15	0.02	1.10
CHF	Yes/no	7.45	2.16	25.71	2.74	0.67	11.25
COPD	Yes/no	1.65	0.65	4.17	–	–	–
Diabetes mellitus	Yes/no	1.24	0.70	2.17	–	–	–
Current smoker	Yes/no	1.40	0.74	2.65	–	–	–
BP cluster	A-D/B-C	2.56	1.44	4.57	2.16	1.10	4.19

Table 29: (3) Cox proportional hazard models for hospitalization. eGFR, estimated glomerular filtration rate; MELD, Model for End-Stage Liver Disease; CI, confidence interval; FU, follow-up period; CHF,

congestive heart failure; COPD, chronic obstructive pulmonary disease; inf, infective; n-inf, not infective; INR, International Normalized Ratio.

Discussion

Our data showed that BP analysis by e-nose could identify cirrhotic patients with a significantly higher risk of mortality and hospitalization. The association between BP clusters and both outcomes was independent of any potential confounding factors and, to note, also from "classical" prognostic indices, such as CPC and MELD.

This study was the logical continuation of our recent study [81], which explored the discriminative and classificatory properties of BPs, detected by e-nose, in patients with cirrhosis and different stages of hepatocellular failure. By means of partial least squares—discriminant analysis (PLS-DA), we showed that different BPs distinguished patients with cirrhosis and, among them, patient with increasing CPC. On the basis of these results and according with the observed relation with CPC, we hypothesized that BP could own an original and independent prognostic information.

The possible pathophysiological explanation could rely on the progressive dysregulation of hepatic metabolic processes during the course of liver disease. These alterations may, then, lead to the accumulation of endogenous compounds in the blood, which, if volatile, can be found in the exhaled breath and characterize different BPs. Accordingly, it has been shown that the exhaled breath of cirrhotic patients is enriched of alkanes, alkenes, terpenes, ketones and S-compounds compared to healthy controls [82][84][85].

This was the first study exploring the association of exhaled breath analysis by e-nose system with clinically relevant endpoint. To our knowledge, despite the huge number of published work on the diagnostic performances of different techniques for exhaled breath sampling and analysis, this issue has never been investigated so far. Furthermore, this study relies upon a non-invasive, easy to perform and standardized technology for breath analysis, that is feasible for execution at bedside.

Noteworthy, the whole measure chain for breath analysis by the e-nose system is much cheaper (around 6.000 euro) than the other analytical techniques (GC-MS, IMS or PTR-MS) and each procedure costs around 10 euro (considering costs of cartridges and consumables).

Combined Systems Applications

Control quality analysis of Olive Oil [86]

Introduction

Olive oil is the most popular vegetable oil produced and consumed in Mediterranean countries. According to international standards [87], olive oils have to be obtained exclusively from the fruit of the olive tree (Olea europaea) using cold pressing techniques and in conditions that do not alter the organoleptic properties of the oil at all. Olive oils can be classified as extra virgin olive oil (EVOO), virgin olive oil, and other low-quality olive oil typologies.

Recently, the authentication of products labelled as olive oil has become a fundamental issue for either commercial or health aspects [88][89]. In fact, the high price of olive oil and its increased popularity as a potential health food have made it an ideal target for frauds [90]: common olive oil adulterations include accidental contaminations during production stages, deliberate mislabelling of less expensive oil categories and, more often, the admixtures of expensive olive oils with low quality oils.

Actually, no rapid and universal method exists that is officially recognized for all the authenticity issues [91]. Since the existing methods require valuable instrumentation and highly qualified staff, authentication is a time consuming and expensive process, which is not applicable as routine analysis.

In this experimental study, a combined system, consisting of a novel developed e-nose and e-tongue, was employed to analyse olive oil samples. The system, which embeds gas and liquid sensors having a common biologically derived sensing interface, allows the simultaneous analysis of the vapour and liquid phase of the samples. At the end of the analytical procedure, similarities and differences between the samples are highlighted.

Materials & Methods

Oil Samples

Twelve EVOO samples, indicated in the paper as EVOO #1, #2, #3, and so on, were obtained from twelve different Italian orchards. Several characteristics of the oils are reported (Table 30). The commercial EVOO as well as the pomace, soybean, sunflower seeds, and peanut oils were bought at a local market.

Oil Sample	Geographical Origin	Year of Production	Oil Variety
EVOO #1	Laterba	2013/2014	Picoline
EVOO #2	Castellaneta	2013/2014	Leccino
EVOO #3	Laterba	2013/2014	Picoline (Organic)
EVOO #4	Laterba	2013/2014	Arbequina (Organic)
EVOO #5	Grottaglie and Crispiano	2013/2014	Picoline (50%), Nociara (35 %), Leccino (15%)
EVOO #6	Crispiano	2013/2014	Leccino
EVOO #7	Grottaglie	2013/2014	Ogliarola
EVOO #8	Grottaglie	2013/2014	Picoline

EVOO #9	Grottaglie	2012/2013	Cellina di Nardò
EVOO #10	Laterba	2013/2014	Leccino
EVOO #11	Crispiano	2012/2013	Cellina di Nardò
EVOO #12	Crispiano	2012/2013	Cima di Melfi

Table 30: General EVOOs characteristics

Gas Sensors System

The e-nose used in this study is based on an array of six quartz microbalances covered by six different anthocyanins extracted by three different plant tissues: red rose, red cabbage, blue hortensia.

In order to perform homogeneous gas measurements the following experimental set-up was used. A volume of 2 mL for each olive oil sample was placed in a 50 mL glass flask and kept for 10 min at room temperature to obtain an adequate headspace. Dehumidified reference air was pumped into the sensors chamber at a flow rate of 3 L/min for 10 min to desorb any volatile trace from sensors surface before every measure. Oil samples were analysed five times, setting a sampling interval of 90 s.

Volatile compounds released in the system headspace at room temperature were characterized through their interaction with the functionalized sensors, resulting in a reproducible pattern response.

Liquid Sensors System

The used e-tongue system is inspired by electrochemical measuring techniques and was designed and implemented to perform cyclic voltammetry analysis on liquid samples.

The system consists of an electrode, an input signal generator stage, a signal conditioning stage and a data acquisition stage. The device can send the acquired data to a PC; using a GUI it's possible to visualize and save the acquired data.

The electrode is a screen-printed electrode fabricated by DropSens S.L. (Llanera (Asturias), Spain): the working (4 mm diameter) electrode is made of gold, the counter electrode is made of platinum, the reference electrode is made of Ag and electric contacts are made of silver. Its dimensions (3.4 × 1.0 × 0.05 cm—Length × Width × Height) are ideal for working with 50µL volume.

The applied input signal consists of a triangular waveform, from -1 V to +1 V. The frequency of the input signal has been set to 0.01 Hz. The output signal is acquired with a sampling rate of 1 s thus collecting 100 samples of the output current, treated as a single 'fingerprint' composed of a virtual array of 100 sensors.

Olive oil samples for liquid sensor analysis were prepared following the procedure reported below.

Briefly, a volume of 1 mL of oil was poured into a tube with 3 mL of methanol 70% (v/v) and mixed vigorously for 1 min. The vial containing the oil-alcohol emulsion was centrifuged for 5 min at 1000 RCF and 4 °C to separate the two phases efficiently. Finally, the methanol phase was collected and stocked in ice up until the analysis.

A volume of 3 mL of the methanol phase for each olive oil sample was spilled in a 4 mL cuvette (normally used for spectrophotometric analysis). Then, the

sensor probe was immersed in the cuvette and four cycles were run for each sample. The time duration of the complete measurement process is of about 90 s.

Chemical Quality Control Analyses

Polyphenol content, free acidity, peroxide value, ΔK, and refractive index of olive oil samples have been assessed following the standard chemical testing methods [92].

Data Analysis

Multivariate data analysis: Principal Component Analysis (PCA) and Partial Least Square Discriminant Analysis (PLS-DA), was performed using PLS-Toolbox (Eigenvector Research Inc., Manson, WA, USA) in the Matlab Environment (The MathWorks, Natick, MA, USA). PLS-DA models have been calculated in order to detect EVO adulteration and investigate BIONOTE relevance to the chemical parameters.

Results

Olive Oil BIONOTE Characterization

A data fusion of the information deriving from the e-nose and e-tongue devices was accomplished. The obtained data set has been evaluated by Principal Component Analysis (PCA) and the ability of the system to sharply discriminate the twelve EVOOs was demonstrated.

The score plot of the first two Principal Components (PCs), accounting for 76.94% of the explained variance, is reported (Figure 147). Ten of the twelve oil samples clustered in three separate regions along the Principal Component 2 (PC2). EVOOs #1, #6, and #12 formed a group in the bottom part of the plane. EVOOs #5, #8, #10, and #11 distributed in a second area at the interception of the two PCs. EVOOs #2, #4, and #9 clustered in the upper portion of the plane (Figure 147). Nevertheless, within the groups almost every oil sample can be discriminated from the others along the Principal Component 1 (PC1). EVOOs #3 and #7 were distinguished from the rest of the analyzed samples by positioning at the upper end and at the left edge of the plane, respectively (Figure 147).

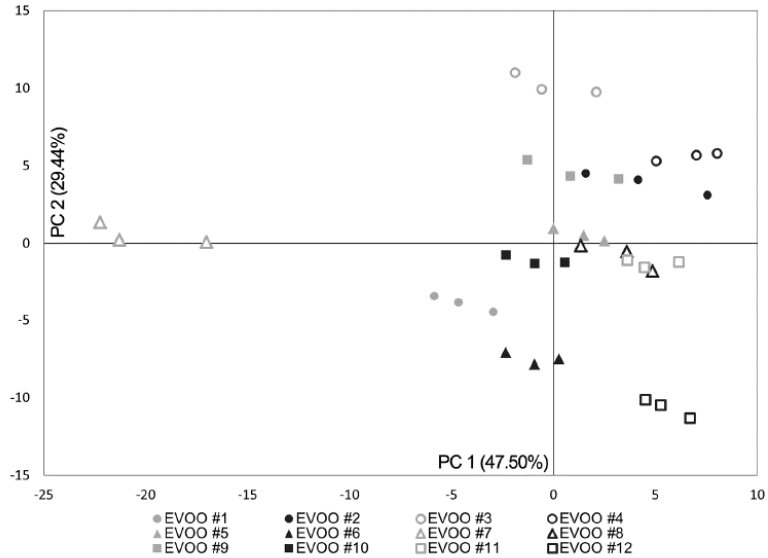

Figure 147: Score Plot of the first two principal components deriving from the data fusion of the liquid and gas sensors systems responses.

Olive Oil Chemical Characterization

To assess the quality of the EVOOs, common chemical analyses were also performed. The obtained results confirmed the excellent quality of the oil samples, highlighting the absence (in terms of usual parameters) of significant differences between the EVOOs themselves.

Oil Sample	Free Acidity (mg/100g Oleci Acid)	Peroxide Value (mEq O_2/Kg)	**ΔK**	Refractive Index
EVOO#1	3.4±0.1	15.0±0.4	0.0020	1.469
EVOO#2	3.4±0.1	12.2±0.1	0.0045	1.468
EVOO#3	4.9±0.2	6.0±0.1	0.0065	1.468
EVOO#4	2.0±0.1	6.9±0.1	0.0015	1.467
EVOO#5	7.3±0.1	8.7±0.1	0.0015	1.468
EVOO#6	6.0±0.1	9.5±0.3	0.0005	1.467
EVOO#7	5.3±0.1	7.2±0.4	0.0030	1.467
EVOO#8	4.3±0.2	18.1±0.2	0.0045	1.468
EVOO#9	2.8±0.1	9.9±0.2	0.0035	1.468
EVOO#10	3.9±0.1	13.5±0.4	0.0015	1.467
EVOO#11	6.1±0.2	9.4±0.5	0.0030	1.467
EVOO#12	3.1±0.2	9.9±0.3	0.0160	1.467

Table 31: EVOO purity and quality characteristics according to the International Olive Council [87].

Olive Oil Adulteration

A commercial EVOO was bought at local market and mixed with four vegetable oils (pomace, soybean, sunflower seeds, and peanut oils) at different blending concentrations (1.25%, 5%, 10%, and 25% (v/v)).

The prepared EVOO's admixtures were analysed using the combined e-nose/e-tongue system.

The output data were used to calculate a PLS-DA model that highlighted the ability of the system to distinguish an authentic EVOO from an adulterated one in all the tested cases, showing also a rather high degree of efficiency in the concentration discrimination (Figure 148). The Root Mean Square Error in Cross Validation (RMSECV), using the Leave One Out criterion, was slightly different among the four kinds of sophistication.

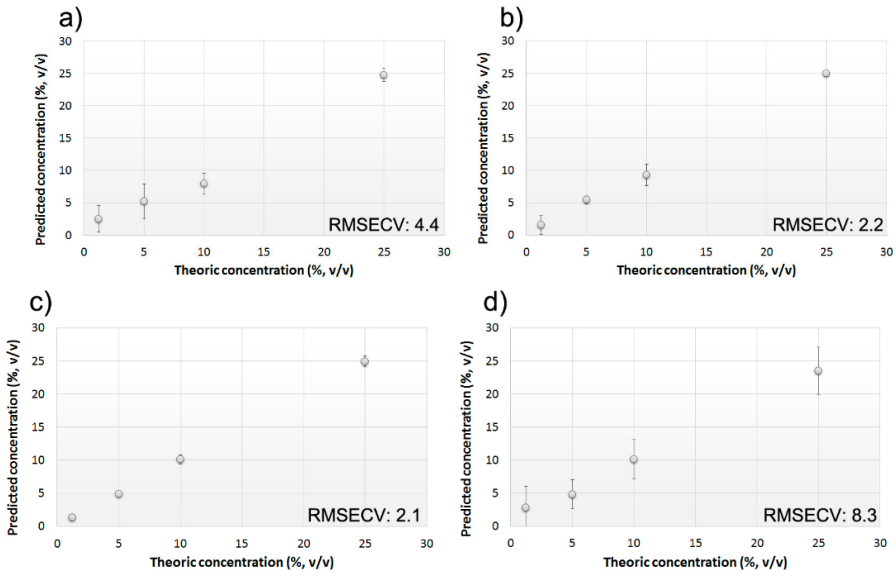

Figure 148: Calculated PLS-DA model for the prediction of contaminating oils concentration. Calibration model has been built using a commercial EVOO sophisticated with 0%–25% (v/v) of (a) soybean oil; (b) sunflower seeds oil; (c) peanut oil; and (d) pomace oil. RMSECV associated with the models are reported.

Prediction of Chemical Parameters

The ability of the combined e-nose/e-tongue system to predict chemical parameters of the oil samples was investigated: calculating four different models to predict polyphenols content, free acidity, peroxide value, and TEAC on the gas and liquid sensor array data.

The results obtained are very promising (see Figure 149, panel a: polyphenols; panel b: free acidity; panel c: peroxide value; and panel d: TEAC).

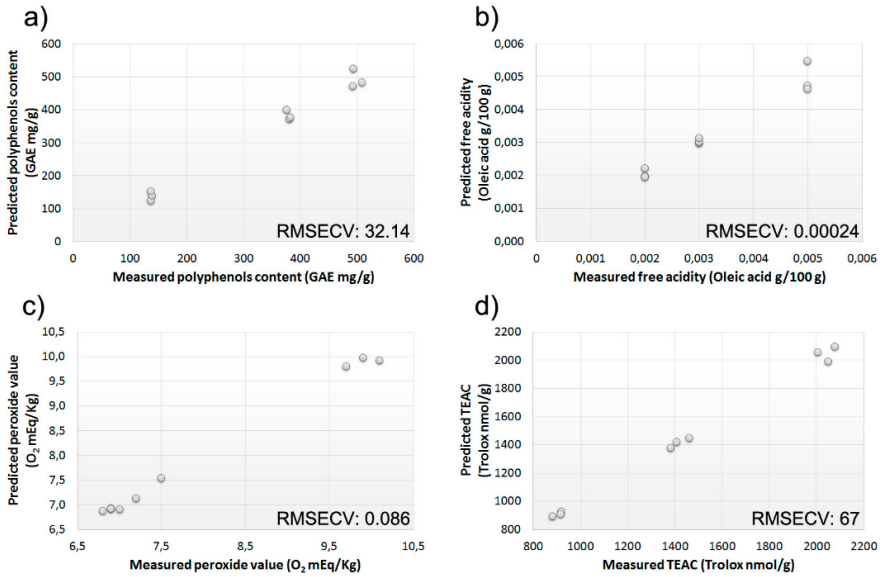

Figure 149: Measured versus predicted (PLS-DA model based on BIONOTE data) values of (a) polyphenols; (b) free acidity; (c) peroxide value; and (d) TEAC.

Conclusions

So far, numerous modern techniques have been proposed to support or replace official standard methods in the task of olive oil authentication [93][94][95][96][97]. However, those do not offer clear advantages yet, because their adulteration detection limits, being usually greater than 10% of contamination, are worse in comparison with chromatographic techniques' ones.

In this experimental study, a novel system able to characterize EVOOs in terms of genuineness and authenticity has been presented. The multi-sensors platform takes advantage of either liquid and gas analysis to accomplish a multi-parametric characterization, giving comprehensive information about the sample [98]. The overall sensors' responses are elaborated through multivariate data analysis techniques to highlight similarities and differences, resulting in a correct classification rate of 100%, even when similar EVOOs have been analyzed.

The combined e-nose/e-tongue system was challenged with different kind of EVOO sophistications, covering concentrations lower than 10% (v/v), and in all cases it was able to distinguish authentic oil from an adulterated one. The system detected the presence of fraudulent admixing of extraneous vegetable oils (soybean, sunflower seeds and peanut oils) up to concentrations lower than 5%. However, when the pomace oil was used, system performance decreased. This discrepancy, leading to an increment of the detection limit to about 8%, could be probably explained by the shared origin between EVOO and pomace oil.

Moreover the result highlighted the capability of multi-sensors platform not only to identify EVOOs against lower grade olive oils, but also to discriminate

between EVOOs obtained from different olive cultivars. This is a notable outcome because this issue is usually addressed via more complex genetic approaches.

The novel multi-sensors platform could represent a real opportunity thanks to its reduced time and costs of analysis.

However, due to the qualitative approach on which the system is based on, the platform has not been intended to replace the high specificity of the official chromatographic methods. Hence, it is proposed as a rapid tool for preliminary high-throughput screening, aimed to detect samples that require further analytical verifications.

Conclusions and future developments

The PhD research activities, presented in this thesis, have led to the development of novel multi-sensory platform: a new e-nose sensor system based on QCMs with a resonance oscillation of 30MHz and a new electrochemical e-tongue system based on cyclic voltammetry techniques were designed, developed and tested.

The experimental tests demonstrated that an e-nose sensor system based on QCMs with a resonance oscillation of 30MHz owns better measuring performances than an e-nose sensor system based on traditional QCMs with a resonance oscillation of 20MHz: the developed device could provide a new approach for the realization of high-performance gas sensing systems and could become a new standard for the realization of e-nose systems based on AT cut quartz crystals.

Moreover it was experimentally demonstrated that the developed e-tongue system is a very versatile liquid sensor device: the system can perform electrochemical analysis on liquid samples without the need of specific functionalization. The system is able to analyse and discriminate liquid samples. Both sensing systems were successfully tested in several applications ranging from the medical to the food industry field and many more applications can be explored in other areas.

Though the developed sensing systems have already showed excellent performances applied separately or combined in a gas/liquid sensor system, some improvements could be made:

- Further studies are needed to optimize the QCMs functionalization, that is a crucial factor for the performances and the repeatability of the measuring device;
- The electrodes driver stage, used in the e-tongue, could be improved to provide the best possible input signal to the electrochemical cells: actually the triangular input wave is approximated by a voltage steps sequence. The amplitude of the voltage steps should be lowered, optimizing the input signal for a specific frequency of the signal.
- The e-tongue electrodes could be functionalized in order to optimize specific applications, mostly in the medical field.

All the proposed developments are fully accessible with appropriate research activities.

Future developments are also needed to transform the e-nose and the e-tongue systems from advanced prototype devices to robust and user-friendly commercial products.

Bibliography

[1] Boron, Walter F., and Emile L. Boulpaep. Medical physiology. Elsevier Health Sciences, 2016.

[2] Stone, Leslie M., et al. "Taste receptor cells arise from local epithelium, not neurogenic ectoderm." Proceedings of the National Academy of Sciences 92.6 (1995): 1916-1920.

[3] T.R. Scott, C.R. Plata-Salaman, Coding of taste quality in Smell and Taste in Health and Disease, Raven, New York, 1991, pp. 345–368.

[4] T. Yamamoto, N. Yuyama, Y. Kawamura, Central processing of taste perception in Brain Mechanisms of Sensation, Wiley, New York, 1981, pp. 197–207.

[5] McLaughlin, S., & Margolskee, R. F. (1994). The sense of taste. American Scientist, 82(6), 538-545.

[6] Lundy, R. F., & Contreras, R. J. (1999). Gustatory neuron types in rat geniculate ganglion. Journal of neurophysiology, 82(6), 2970-2988.

[7] Erickson, R. P. (2000). The evolution of neural coding ideas in the chemical senses. Physiology & behavior, 69(1), 3-13.

[8] Lindemann, B. (2001). Receptors and transduction in taste. Nature, 413(6852), 219-225.

[9] Bachmanov, A. A., Beauchamp, G. K., & Tordoff, M. G. (2002). Voluntary consumption of NaCl, KCl, CaCl2, and NH4Cl solutions by 28 mouse strains. Behavior genetics, 32(6), 445-457.

[10] Lindemann, B. (1996). Taste reception. Physiological reviews, 76(3), 719-766.

[11] Buck, L. B. (2004). Olfactory receptors and odor coding in mammals. Nutrition reviews, 62(suppl 3), S184-S188.

[12] Saberi, M., & Seyed-allaei, H. (2016). Odorant receptors of Drosophila are sensitive to the molecular volume of odorants. Scientific reports, 6.

[13] Jones, D. T., & Reed, R. R. (1989). Golf: an olfactory neuron specific-G protein involved in odorant signal transduction. Science, 244(4906), 790-795.

[14] Malnic, B., Hirono, J., Sato, T., & Buck, L. B. (1999). Combinatorial receptor codes for odors. Cell, 96(5), 713-723.

[15] Gibson, J. J. (1966). The senses considered as perceptual systems.

[16] Stein, B. E., & Meredith, M. A. (1993). The merging of the senses. The MIT Press.

[17] De Araujo, I. E., Rolls, E. T., Kringelbach, M. L., McGlone, F., & Phillips, N. (2003). Taste-olfactory convergence, and the representation of the pleasantness of flavour, in the human brain. European Journal of Neuroscience, 18(7), 2059-2068.

[18] Gardner, J. W., & Bartlett, P. N. (1994). A brief history of electronic noses. Sensors and Actuators B: Chemical, 18(1), 210-211.

[19] Sberveglieri, G. (Ed.). (2012). Gas sensors: principles, operation and developments. Springer Science & Business Media.

[20] Banerjee, R., Tudu, B., Bandyopadhyay, R., & Bhattacharyya, N. (2016). A review on combined odor and taste sensor systems. Journal of Food Engineering, 190, 10-21.

[21] Winquist, F., Lundstrom, I., Wide, P., 1999. Combination of an electronic tongue and an electronic nose. Sens. Actuators B Chem. 58 (1-3), 512-517.

[22] Wide, P., Winquist, F., Bergsten, P., Petriu, E.M., 1998. The human-based multisensor fusion method for artificial nose and tongue sensor data. IEEE Trans. Instrum. Meas. 47 (5), 1072e1077.

[23] Sundic, T., Marco, S., Samitier, J., Wide, P., 2000. Electronic tongue and electronic nose data fusion in classification with neural networks and fuzzy logic based models. In: Conference Record e IEEE Instrumentation and Measurement Technology Conference 3, pp. 1474e1479.

[24] Di Natale, C., Paolesse, R., Macagnano, A., Mantini, A., D'Amico, A., Legin, A., Lvova, L., Rudnitskaya, A., Vlasov, Y., 2000a. Electronic nose and electronic tongue integration for improved classification of clinical and food samples. Sens. Actuators B Chem. 64 (1e3), 15e21.

[25] Di Natale, C., Paolesse, R., MacAgnano, A., Mantini, A., D'Amico, A., Ubigli, M., Legin, A., Lvova, L., Rudnitskaya, A., Vlasov, Y., 2000b. Application of a combined artificial olfaction and taste system to the quantification of relevant compounds

[26] Buratti, S., Benedetti, S., Scampicchio, M., Pangerod, E.C., 2004. Characterization and classification of Italian Barbera wines by using an electronic nose and an amperometric electronic tongue. Anal. Chim. Acta 525 (1), 133e139.

[27] Buratti, S., Ballabio, D., Benedetti, S., Cosio, M.S., 2007. Prediction of Italian red wine sensorial descriptors from electronic nose, electronic tongue and spectrophotometric measurements by means of genetic algorithm regression models. Food Chem. 100 (1), 211e218. in red wine. Sens. Actuators B Chem. 69 (3), 342e347.

[28] Cosio, M.S., Ballabio, D., Benedetti, S., Gigliotti, C., 2006. Geographical origin and authentication of extra virgin olive oils by an electronic nose in combination with artificial neural networks. Anal. Chim. Acta 567 (2), 202e210.

[29] Cosio, M.S., Ballabio, D., Benedetti, S., Gigliotti, C., 2007. Evaluation of different storage conditions of extra virgin olive oils with an innovative recognition tool built by means of electronic nose and electronic tongue. Food Chem. 101 (2), 485e491.

[30] Bleibaum, R.N., Stone, H., Tan, T., Labreche, S., Saint-Martin, E., Isz, S., 2002. Comparison of sensory and consumer results with electronic nose and tongue sensors for apple juices. Food Qual. Prefer. 13 (6), 409e422.

[31] Rodríguez-M_endez, M.L., Apetrei, C., Apetrei, I., Villanueva, S., De Saja, I.J.A., Nevares, I., Del Alamo, M., 2007. Combination of an electronic nose, an electronic tongue and an electronic eye for the Analysis of Red Wines aged with alternative methods. In: IEEE International Symposium on Industrial Electronics, Art. No. 4375050, pp. 2782e2787.

[32] Apetrei, C., Apetrei, I.M., Villanueva, S., de Saja, J.A., Gutierrez-Rosales, F., 2010. Combination of an e-nose, an e-tongue and an e-eye for the characterisation of olive oils with different degree of bitterness. Anal. Chim. Acta 663 (1), 91e97.

[33] Cole, M., Covington, J.A., Gardner, J.W., 2011. Combined electronic nose and tongue for a flavour sensing system. Sens. Actuators B Chem. 156 (2), 832e839.

[34] Gil-S_anchez, L., Soto, J., Martínez-M_a~nez, R., Garcia-Breijo, E., Ib_a~nez, J.,

Llobet, E., 2011. A novel humid electronic nose combined with an electronic tongue for assessing deterioration of wine. Sens. Actuators, A Phys. 171 (2), 152e158.

[35] Buratti, S., Ballabio, D., Giovanelli, G., Dominguez, C.M.Z., Moles, A., Benedetti, S., Sinelli, N., 2011. Monitoring of alcoholic fermentation using near infrared and mid infrared spectroscopies combined with electronic nose and electronic tongue. Anal. Chim. Acta 697 (1e2), 67e74.

[36] Zakaria, A., Md Shakaff, A.Y., Adom, A.H., Ahmad, M.N., Masnan, M.J., Aziz, A.H.A., Fikri, N.A., Abdullah, A.H., Kamarudin, L.M., 2010. Improved classification of Orthosiphon stamineus by data fusion of electronic nose and tongue sensors. Sensors 10 (10), 8782e8796.

[37] Zakaria, A., Shakaff, A.Y.M., Masnan, M.J., Ahmad, M.N., Adom, A.H., Jaafar, M.N., Ghani, S.A., Abdullah, A.H., Aziz, A.H.A., Kamarudin, L.M., Subari, N., Fikri, N.A., 2011. A biomimetic sensor for the classification of honeys of different floral origin and the detection of adulteration. Sensors 11 (8), 7799e7822.

[38] Haddi, Z., Mabrouk, S., Bougrini, M., Tahri, K., Sghaier, K., Barhoumi, H., El Bari, N., Maaref, A., Jaffrezic-Renault, N., Bouchikhi, B., 2014. E-Nose and e-Tongue combination for improved recognition of fruit juice samples. Food Chem. 150, 246e253.

[39] Hong, X., Wang, J., 2014. Use of electronic nose and tongue to track freshness of cherry tomatoes squeezed for juice consumption: comparison of different sensor fusion approaches. Food Bioprocess Technol. 8 (1), 158e170.

[40] Men, H., Chen, D., Zhang, X., Liu, J., Ning, K., 2014. Data fusion of electronic nose and electronic tongue for detection of mixed edible-oil. J. Sens. 2014, 840685.

[41] Ouyang, Q., Zhao, J., Chen, Q., 2014. Instrumental intelligent test of food sensory quality as mimic of human panel test combining multiple cross-perception sensors and data fusion. Anal. Chim. Acta 841, 68e76.

[42] A. D'Amico, C. Di Natale, C. Falconi, E. Martinelli, R. Paolesse, G. Pennazza, M. Santonico, P.J. Sterk Detection and identification of cancers by the electronic nose, expert opinion on medical diagnostics, 6(2012) 175-185, ISSN: 1753-0059.

[43] C. Di Natale, R. Paolesse, G. D'Arcangelo, P. Comandini, G. Pennazza, E. Martinelli, S. Rullo, M.C. Roscioni, C. Roscioni, A. Finazzi-Agrò, A. D'Amico, Identification of schizophrenic patients by examination of body odor using gas chromatography-mass spectrometry and a cross-selective gas sensor array,Medical Science Monitor 11 (8) (2005)CR366-CR375.

[44] G. Peng, U. Tisch, O. Adams, M. Hakim, N. Shehada, Y. Y. Broza,S.Billan, R. Abdah-Bortnyak, A. Kuten and H. Haick, Diagnosing lung cancer in exhaled breath usinggold nanoparticles,nature nanotechnology, 4 (2009)669-673.

[45] E. A. Baldwin, J. Bai, A. Plotto, S. Dea, Electronic noses and tongues: Applications for the food and pharmaceutical industries,Sensors 11 (5) (2011) 4744-4766.

[46] M. Ghasemi-Varnamkhasti, S.S. Mohtasebi, M. Siadat, Biomimetic-based odor and taste sensing systems to food quality and safety characterization: An overview on basic principles and recent achievements, Journal of Food Engineering 100 (2010) 377–387.

[47] G. Pennazza, C. Fanali, M. Santonico, L. Dugo, L. Cucchiarini, M. Dachà, A. D'Amico, R. Costa, P. Dugo, L. Mondello, Electronic nose and GC-MS analysis of volatile compounds in Tuber magnatum Pico: Evaluation of different storage conditions, Food Chemistry 136 (2)(2013)668-674.

[48] C. Di Natale, G. Pennazza, A. Macagnano, E. Martinelli, R. Paolesse, A. D'Amico, Thickness shear mode resonator sensors for the detection of androstenone in pork fat, Sensors and Actuators B:Chemical, 91(2003)169-174, ISSN: 0925-4005, doi: 10.1016/S0925-4005(03)00084-4.

[49] G. Pennazza, M. Santonico, A. Finazzi Agrò, Narrowing the gap between breathprinting and disease diagnosis, a sensor perspective, Sensors and Actuators B: Chemical, (2012)ISSN: 0925-4005, doi: 10.1016/j.snb.2012.09.103.

[50] M. Cole, A. J. Covington, J. W. Gardner, Combined electronic nose and tongue for a flavour sensing system, Sensors and Actuators B 156 (2011) 832–839

[51] J. Simner, Defining synaesthesia, British Journal of Psychology, 103 (1)(2012)1-15.

[52] Compton, R. G., & Banks, C. E. (2007). Understanding voltammetry (p. 107). Singapore: World Scientific.

[53] Compton, R. G. S., & Giles, H. W. (1998). Electrode potentials (No. 544.62 COM).

[54] Kounaves, S. P. (1997). Voltammetric techniques. Handbook of instrumental techniques for analytical chemistry, 709-726.

[55] Bott, A. (1995). Practical problems in voltammetry 3: Reference electrodes for voltammetry. Current Separations, 14, 64-69.

[56] Kissinger, P. T., & Heineman, W. R. (1983). Cyclic voltammetry. J. Chem. Educ, 60(9), 702

[57] Sathe, B. R., Balan, B. K., & Pillai, V. K. (2011). Enhanced electrocatalytic performance of interconnected Rh nano-chains towards formic acid oxidation. Energy & Environmental Science, 4(3), 1029-1036

[58] Ruthven, D. M. (1984). Principles of adsorption and adsorption processes. John Wiley & Sons.

[59] Yang, R. T. (2003). Adsorbents: fundamentals and applications. John Wiley & Sons.

[60] Chattopadhyay, D. (2006). Electronics (fundamentals and applications). New Age International, 224-225

[61] Ramon Cerda, Director of Engineering, Crystek Corporation , Pierce-Gate Crystal Oscillator (http://www.mpdigest.com/)

[62] HC49/4HSMX Datasheet http://www.farnell.com/datasheets/2048129.pdf?_ga=1.136785719.688427019.1479805488

[63] Mazza, G., & Miniati, E. (1993). Anthocyanins in fruits, vegetables, and grains. CRC press.

[64] Pauling, L. (1939). Recent work on the configuration and electronic structure of molecules; with some applications to natural products. Fortschr. Chem. org. Naturstoffe, 3, 203-235.

[65] Brouillard, R., Mazza, G., Saad, Z., Albrecht-Gary, A. M., & Cheminat, A. (1989). The co-pigmentation reaction of anthocyanins: a microprobe for the structural study of aqueous solutions. Journal of the American Chemical Society, 111(7), 2604-2610.

[66] Santonico, M., Parente, F. R., Grasso, S., Zompanti, A., Ferri, G., D'Amico, A., & Pennazza, G. (2016). Investigating a single sensor ability in the characterisation of drinkable water: a pilot study. Water and Environment Journal, 30(3-4), 253-260.

[67] Santonico, M., Frezzotti, E., Incalzi, R. A., Pedone, C., Lelli, D., Zompanti, A., ... & Pennazza, G. (2016). Non-invasive monitoring of lower-limb ulcers via exudate fingerprinting using BIONOTE. Sensors and Actuators B: Chemical, 232, 68-74.

[68] Nelson, E. A., Cullum, N., & Jones, J. (2004). Venous leg ulcers. Clinical evidence, (12), 2774.

[69] Graham, I. D., Harrison, M. B., Nelson, E. A., Lorimer, K., & Fisher, A. (2003). Prevalence of lower-limb ulceration: a systematic review of prevalence studies. Advances in skin & wound care, 16(6), 305-316.

[70] Kantor, J., & Margolis, D. J. (2000). A multicentre study of percentage change in venous leg ulcer area as a prognostic index of healing at 24 weeks. British Journal of Dermatology, 142(5), 960-964.

[71] Moore, K., Huddleston, E., Stacey, M. C., & Harding, K. G. (2007). Venous leg ulcers–the search for a prognostic indicator. International wound journal, 4(2), 163-172.

[72] Turner, C. (2011). Potential of breath and skin analysis for monitoring blood glucose concentration in diabetes. Expert review of molecular diagnostics, 11(5), 497-503.

[73] De Vincentis, A., Pennazza, G., Santonico, M., Vespasiani Gentilucci, U., Galati, G., Gallo, P., ... & Picardi, A. (2016). Breath-print analysis by e-nose may refine risk stratification for adverse outcomes in cirrhotic patients. Liver International.

[74] Mokdad, A. A., Lopez, A. D., Shahraz, S., Lozano, R., Mokdad, A. H., Stanaway, J., ... & Naghavi, M. (2014). Liver cirrhosis mortality in 187 countries between 1980 and 2010: a systematic analysis. BMC medicine, 12(1), 1.

[75] Child, C. G., & Turcotte, J. G. (1964). Surgery and portal hypertension. Major problems in clinical surgery, 1, 1

[76] Pugh, R. N. H., Murray-Lyon, I. M., Dawson, J. L., Pietroni, M. C., & Williams, R. (1973). Transection of the oesophagus for bleeding oesophageal varices. British Journal of Surgery, 60(8), 646-649.

[77] Malinchoc, M., Kamath, P. S., Gordon, F. D., Peine, C. J., Rank, J., & Ter Borg, P. C. (2000). A model to predict poor survival in patients undergoing transjugular intrahepatic portosystemic shunts. Hepatology, 31(4), 864-871.

[78] Christensen, E. (2004). Prognostic models including the Child–Pugh, MELD and Mayo risk scores—where are we and where should we go?. Journal of hepatology, 41(2), 344-350.

[79] Kim, H. J., & Lee, H. W. (2013). Important predictor of mortality in patients with end-stage liver disease. Clinical and molecular hepatology, 19(2), 105-115.

[80] Scarlata, S., Pennazza, G., Santonico, M., Pedone, C., & Antonelli Incalzi, R. (2015). Exhaled breath analysis by electronic nose in respiratory diseases. Expert review of molecular diagnostics, 15(7), 933-956.

[81] De Vincentis, A., Pennazza, G., Santonico, M., Vespasiani-Gentilucci, U., Galati, G., Gallo, P., ... & Picardi, A. (2016). Breath-print analysis by e-nose for

classifying and monitoring chronic liver disease: a proof-of-concept study. Scientific reports, 6.

[82] Pijls, K. E., Smolinska, A., Jonkers, D. M., Dallinga, J. W., Masclee, A. A., Koek, G. H., & van Schooten, F. J. (2016). A profile of volatile organic compounds in exhaled air as a potential non-invasive biomarker for liver cirrhosis. Scientific reports, 6.

[83] Tenax(R) GR adsorbent resin for trapping volatiles. Scientific Instrument Services, Inc.[Internet]. http://www.sisweb.com/index/referenc/tenaxgrm.htm. Accessed April 22, 2016.

[84] Morisco, F., Aprea, E., Lembo, V., Fogliano, V., Vitaglione, P., Mazzone, G., ... & Marmo, R. (2013). Rapid "Breath-Print" of Liver Cirrhosis by Proton Transfer Reaction Time-of-Flight Mass Spectrometry. A Pilot Study. PLoS One, 8(4), e59658.

[85] Van den Velde, S., Nevens, F., van Steenberghe, D., & Quirynen, M. (2008). GC–MS analysis of breath odor compounds in liver patients. Journal of Chromatography B, 875(2), 344-348.

[86] Santonico, M., Grasso, S., Genova, F., Zompanti, A., Parente, F. R., & Pennazza, G. (2015). Unmasking of Olive Oil Adulteration Via a Multi-Sensor Platform. Sensors, 15(9), 21660-21672.

[87] International Olive Council (IOC). Trade Standards Applying to Olive Oils and Olive-Pomace Oils; COI/T.15/NC No 3/Rev. 7; International Olive Council (IOC): Madrid, Spain, 2013.

[88] Yaqoobb, P. (2002). Nutritional and health aspects of olive oil. Eur. J. Lipid Sci. Technol, 104, 685-697.

[89] Moreau, R., & Kamal-Eldin, A. (Eds.). (2015). Gourmet and health-promoting specialty oils. Elsevier.

[90] Zhang, J., Zhang, X., Dediu, L., & Victor, C. (2011). Review of the current application of fingerprinting allowing detection of food adulteration and fraud in China. Food Control, 22(8), 1126-1135.

[91] Aparicio, R., Morales, M. T., Aparicio-Ruiz, R., Tena, N., & García-González, D. L. (2013). Authenticity of olive oil: Mapping and comparing official methods and promising alternatives. Food research international, 54(2), 2025-2038.

[92] International Olive Council (IOC). Determination of the Composition and Content of Sterols and Triterpene Dialcohols by Capillary Column Gas Chromatography; COI/T.20/Doc. No 30; International Olive Council (IOC): Madrid, Spain, 2013.

[93] Agiomyrgianaki, A., Petrakis, P. V., & Dais, P. (2010). Detection of refined olive oil adulteration with refined hazelnut oil by employing NMR spectroscopy and multivariate statistical analysis. Talanta, 80(5), 2165-2171.

[94] Calvano, C. D., De Ceglie, C., D'Accolti, L., & Zambonin, C. G. (2012). MALDI-TOF mass spectrometry detection of extra-virgin olive oil adulteration with hazelnut oil by analysis of phospholipids using an ionic liquid as matrix and extraction solvent. Food chemistry, 134(2), 1192-1198.

[95] Chiavaro, E., Vittadini, E., Rodriguez-Estrada, M. T., Cerretani, L., & Bendini, A. (2008). Differential scanning calorimeter application to the detectionof refined hazelnut oil in extra virgin olive oil. Food Chemistry, 110(1), 248-256.

[96] Maggio, R. M., Cerretani, L., Chiavaro, E., Kaufman, T. S., & Bendini, A. (2010).

A novel chemometric strategy for the estimation of extra virgin olive oil adulteration with edible oils. Food Control, 21(6), 890-895.

[97] Poulli, K. I., Mousdis, G. A., & Georgiou, C. A. (2007). Rapid synchronous fluorescence method for virgin olive oil adulteration assessment. Food chemistry, 105(1), 369-375.

[98] Singleton, V. L., & Rossi, J. A. (1965). Colorimetry of total phenolics with phosphomolybdic-phosphotungstic acid reagents. American journal of Enology and Viticulture, 16(3), 144-158.

[99] Calderon, R. L. (2000). The epidemiology of chemical contaminants of drinking water. Food and chemical toxicology, 38, S13-S20.

[100] Winquist, F., Wide, P., & Lundström, I. (1997). An electronic tongue based on voltammetry. Analytica chimica acta, 357(1), 21-31.

[101] Bard, A. J., Faulkner, L. R., Leddy, J., & Zoski, C. G. (1980). Electrochemical methods: fundamentals and applications (Vol. 2). New York: Wiley.